



DEPARTMENT OF PHYSICS AND ASTRONOMY
AARHUS UNIVERSITY

MASTER'S THESIS



A BLUESONG

TRACING MAGNETIC ACTIVITY IN THE Ca II H & K LINES OF
SOLAR-TYPE STARS USING *eShel*, A COMMERCIAL SPECTROGRAPH
MOUNTED ON THE HERTZSPRUNG SONG TELESCOPE



Author:
NICHOLAS JANNSEN

Supervisor:
CHRISTOFFER KAROFF

JUNE 10, 2019

Contents

Preface	i
Acknowledgments	iii
Abstract	v
1 Introduction	1
2 Stellar Activity	5
2.1 Basic concepts	5
2.2 Chromospheric activity	7
2.2.1 Stellar chromospheres	9
2.2.2 Self-sustaining dynamo	10
2.2.3 Chromospheric HR-diagram	10
2.3 Stellar chromospheric activity research	12
3 Instrumentation	15
3.1 Breaking down a spectrograph	15
3.1.1 Échelle spectrographs	17
3.1.2 Spectroscopic parameters	18
3.1.3 A homogeneous setup	18
3.2 BlueSONG	19
3.2.1 Installation & Integration	20
3.2.2 Coupling eShel to SONG	22
3.2.3 The eShel spectrograph	22
3.2.4 Detectors	23
3.2.5 Acquisition software	24
3.2.6 Technical instrumental work	24
4 Observations	25
4.1 Observational constraints	25
4.1.1 Spectral response	26
4.1.2 Limiting magnitude	26

4.1.3 Seeing	27
4.1.4 Atmospheric dispersion	27
4.2 Target selection	29
4.3 Raw data products	30
5 Pipeline: Blues	33
5.1 Overview	33
5.2 Image reduction	34
5.3 Order tracing	36
5.4 Background subtraction	37
5.5 Spectral extraction	38
5.6 Wavelength calibration	41
5.7 De-Blazing	42
5.8 Scrunching & Merging orders	44
5.9 Radial velocity correction	44
5.10 Continuum normalization	46
6 Results & Discussion	47
6.1 The eShel S index	47
6.1.1 Calibrating to the Mt Wilson scale	50
6.1.2 Uncertainties	51
6.1.3 Results of S indices	53
6.2 Software improvements	56
6.3 System performance	58
6.3.1 Guiding, Focus, & Fiber transmission	58
6.3.2 CCD Detectors	59
6.3.3 Focal-reducer, Collimator, and Objective	61
6.3.4 Effective exposure time	62
6.3.5 Optimizing the calibrating	63
7 Conclusion & Future prospects	65
List of Figures	71
List of Tables	73
Appendix A: BlueSONG Cookbook	75
Appendix B: Technical Work	83

*“Astronomers, like burglars and blues
musicians, operates best at night”*
– Miles Kington,

Preface

This is my Master’s thesis, the final outcome of my work with the commercial échelle spectrograph, *eShel*, mounted on the Hertzsprung SONG telescope, located on the Canarian island Tenerife. My project involvement started back in September 2017, by planning and conducting a service operation to optimize the instrumental setup of the eShel-SONG spectroscopic system, coined *BlueSONG* (or originally coined as *Blue Spec*). To fully understand this project, a basic knowledge of astronomy corresponding to the knowledge gained by astronomical coursework for the bachelor degree of physics at Aarhus University is assumed. A basic knowledge of object-oriented programming is likewise assumed, as the project’s spectroscopic pipeline have been developed in Python.

This thesis has been typeset in L^AT_EX, using a template originally created by Mathias Legrand, but has been extensively modified and inspired by the book *Introduktion til L^AT_EX* by Mads Larsens (a.k.a Daleif). Moreover, every chapter image showing the Sun (Chapter 1, 2, 6, and 7) are observations from the Solar Dynamics Observatory (SDO) mission. The source of the remaining chapter images are presented in the relevant chapters. All images presented in this work are checked against copyright, and all links are checked against continual existence from June 10, 2020. Also, all images not credited are a product of this work, either produced using Python or the vector-graphics software Inkscape. Lastly, as this work is interlinked into the Stellar Astrophysics Center (SAC) in Aarhus, the dark blue logos on the front page is the SAC logo extended by my artistic impression of stellar winds streaming through interplanetary space.

*Nicholas Emborg Jannsen
nej@not.iac.es
La Palma, June 10, 2019*

*“There is no blue without
yellow and orange”*
– Vincent Van Gogh

Acknowledgments

I will like to use this opportunity to direct my greatest cheer and gratitude to a handful of people that have been a guiding light before and during this work.

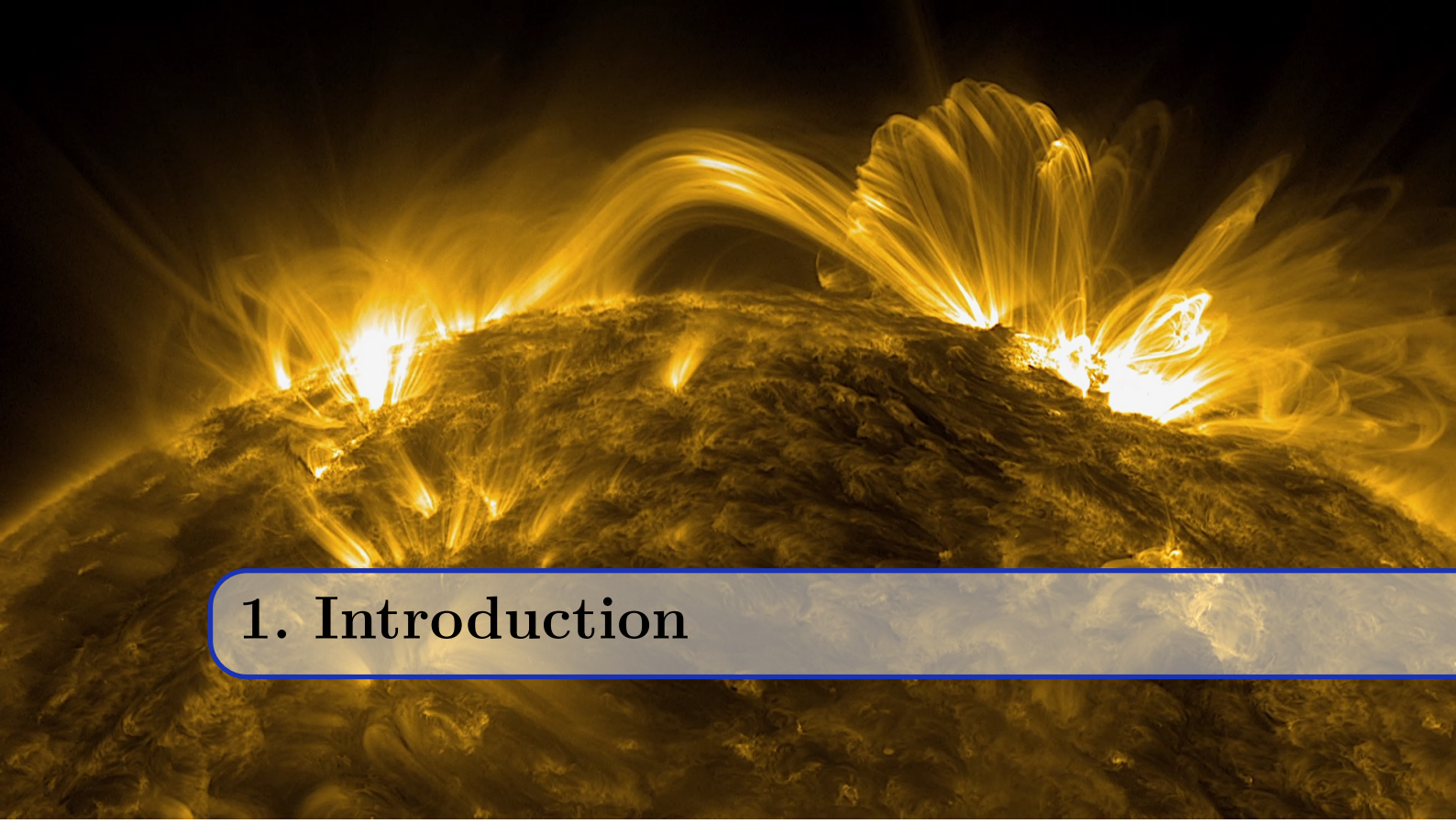
First, like so many others, formally we use results from a massive observational program, where credits needs to be given to *HK_Project_v1995_NSO*: data derived from the Mount Wilson Observatory HK Project, which was supported by both public and private funds through the Carnegie Observatories, the Mount Wilson Institute, and the Harvard-Smithsonian Center for Astrophysics starting in 1966 and continuing for over 36 years. These data are the result of the dedicated work of O. Wilson, A. Vaughan, G. Preston, D. Duncan, S. Baliunas, and many others. Secondly, a thank goes to Pedro Ré for borrowing me his beautiful pictures of the Sun in optical and Ca II K emission, taking on March 23, 2014.

Having a huge impact on my current well-fare and an indirect impact on this project, a sincere cheer goes to René Rasmussen and Ditte Slumstrup for encouraging me to apply for a NOT studentship, which was initiated not long after the beginning of this writing. A great thank likewise goes to Jens Jessen Hansen for his generosity of handing me a draft of the automated spectral reduction pipeline **SONGWriter**, designed for the Hertzsprung SONG telescope. With very limited experience in spectroscopy, Jens provided solid understanding for the foundation of spectroscopic software development. In connection hereto, I would also like to express my gratitude towards my fellow NOT students, for ever great discussions on observation and instrumentation. Among the students, a special thank goes to Joonas Uijas for many (and always) good discussions, for being the ‘know-how’ guy in instrumentation, and for reading through my thesis. For also reading through this work, I would likewise express my biggest gratitude to my old friend Amalie Vonge.

For subjects of technical matter, I would like to use this opportunity to give a great thank to the operational SONG team, especially to Mads Fredslund and Frank Grundahl for their collaboration on time allocation for observations, always kind attitude towards this second-hand SONG project, and useful observational and technical advises. In continuation a huge cheer goes to the technician and hardware-developer of BlueSONG, namely Simon Holmbo. Without his contribution this project would not have been possible. Last, but not least, I direct my greatest acknowledgement to my supervisor Christoffer Karoff for a wonderful collaboration, always useful advices, and helpful input on knowledge in the field of this project. It has been a honor and I am looking forward to collaborate in the future.

Abstract

This project involves the commercial échelle spectrograph, *eShel*, mounted on the fully robotic Hertzsprung SONG telescope on Tenerife, to prove the concept of using an affordable spectrograph, to trace stellar magnetic activity in the Ca II H & K lines of solar-type stars. The eShel is a fiber-fed échelle spectrograph with a spectral resolving power of $\mathcal{R} \approx 10,000$, and it has proven to be a useful tool for the detection of radial velocities down to 80 m s^{-1} , but with the difficulty of receiving a sufficient emission excess in the near-UV, this project is to our knowledge the first of its kind. Since the strongest spectral features observable from ground are the Ca II H & K lines, and the fact that long-term observations of stellar chromospheric activity primarily comes from the Mt Wilson 30-year HK-Project, this research likewise use the Ca II H & K lines as a proxy of stellar magnetic activity. The project objectives are thus; first to investigate that an off-the-shelf spectrograph like eShel can provide sufficient Ca II H & K line emission by observations. Secondly, to calculate the chromospheric activity proxy S and, thirdly, evaluate the success off monitoring activity cycles of stars similar to the Sun using eShel. To meet these requirements, observations obtained with eShel, were supplemented by simultaneous observations made with the FIES spectrograph at the Nordic Optical Telescope, and both dataset was directly compared to the Mt Wilson survey. In a near-future with an increasing number of larger ground and space based telescopes, such as the TMT, ELT, PLATO, JWST, etc., an increase of small and fully robotic telescopes will be needed to complement monitoring, survey, and follow-up observations, of which we begin to see their infancy. Hence, the fact that this master's thesis demonstrates, that the eShel spectrograph can be used to successfully monitor stellar magnetic activity of solar-type stars, confirms that commercial spectrographs may be of significant importance, for future networks of large surveys within the scope of observing and understanding stellar activity in solar-type stars. If proving worthy in terms of efficiency, eShel will provide a possibility and great potential for observing stellar cycles using the Hertzsprung SONG telescope.



1. Introduction

Variability changes and dark spots on the solar surface have been monitored since the invention of the telescope in the early 17th century. With Johannes Fabricius being the first person to publish a scientific treatise on this subject (Fabricius, 17th), a door to more than 400 years of solar exploration became open wide. Diligent observations of these phenomena throughout the following centuries lead to the discovery of the Sun's 11-year¹ periodic rise and fall in the number of sunspots: the so-called *solar cycle* (Schwabe, 1844). Identified by Hale (1908) we now know that sunspots are regions with an enhanced local magnetic fields and that the solar cycles thus likewise is of magnetic nature. In the early 1900s it was discovered that these areas of concentrated magnetic fields of the Sun can been seen in *chromospheric activity* due to the production of strong emission e.g. in the Ca II or Mg II spectral line cores. Although direct observations of spots is only limited to the Sun, Eberhard and Schwarzschild (1913) noticed similar Ca II H & K line “reversal” features in spectra of bright stars (Arcturus, Aldebaran, and σ Gem), and therefore questioned first if the emission arose from processes similar to the solar activity and, secondly, if an emission periodicity similar to the sunspot cycle exists.

These questions, whether a similar phenomenon also occurs in other stars, were in the 1960s pursued by the dedicated astronomer Olin Wilson, who started what would become the famous *HK Project* at the Mt. Wilson Observatory (MWO) (Wilson, 1968).² Exploiting that the strongest spectral features observable from ground are the Ca II H & K lines, together with their physical ground of being a useful proxy for the strength of, and fractional area covered by, magnetic fields, chromospheric emission of more than 2300 solar-type stars in the solar neighborhood was monitored for more than 30 years. Normalizing the measured Ca II core flux by the flux in two quasi-continuum bandpasses on the blue and red sides of the Ca II lines, the HK Project’s “heart of darkness”, the so-called *S* index,

¹Or 22-year sunspot period if defined as full magnetic bipolar cycle just like that of the Earth, where the magnetic poles inverts for later to return.

²One may emphasize the tremendous work of Wilson's successor, Sallie Baliunas, who kept the program going until 2003.

was born. Long-term results of the S index from this program (e.g. Wilson, 1978; Duncan et al., 1991; Baliunas et al., 1995), demonstrates that activity cycles similar to the solar one are indeed common in other stars. In fact, analyzing 111 stars with highest cadence from a 25 year MWO dataset, Baliunas et al. (1995) showed that long-term magnetic variability (between 2–25 years) manifests in cyclic, flat, and irregular variability.

Given the greater perspective, it is evident that activity analyses of the Sun is a cyclic process in understanding stellar activity in general, and vice versa. Hence accurately placing the Sun on the S scale is important for understanding the so-called *solar-stellar connection*. Such solar measurements means observing “the Sun as a star”, hence unresolved solar spectroscopy. Luckily, such observations at Wilson’s time were easy to come by, simply using scattered light from the Moon or the Rayleigh scattering from the blue sky. Later direct long-term Ca II H & K observations of the Sun began at the National Solar Observatory (NSO) in 1974 using the McMath solar telescope at Kitt Peak (White and Livingston, 1981), and in 1976 at Sacramento Peak (Keil and Worden, 1984). Present studies placing the Sun on the S scale accurately (Egeland et al., 2017), have confirmed that despite much effort finding solar analogs, only very few stars resembles the Sun.

By the tremendous effort in understanding the solar-stellar connection, together with the fact that we still at this writing are unable to answer the question “is the Sun special?”, reminds us that the journey into solar and stellar explorations has just begun. The solar-stellar connection began as a relatively small field of research, but have in the last few decades, become of high astrophysical importance for disciplines in stellar structure and evolution, as magnetic fields comprise a limiting factor in the determination of gross stellar parameters and modeling (Hall, 2008). A shared motivation in exoplanet detection studies have emerged, as state-of-the-art spectrographs now are able to detect $\sim 1\text{ m s}^{-1}$ Radial Velocity (RV) signals from Earth-sized planet, where long-term activity of solar-type stars may prohibit such detections by inducing RV “noise” at a significantly higher level (e.g. Lovis et al., 2011). Pushing the frontier towards detections of rocky exoplanet naturally lead to questions about their habitability and (exo)space weather, which may be determined ultimately by the activity level of the stellar host (e.g. Lingam and Loeb, 2018). From a broader perspective such considerations interlinks deeply into keen debates about how the Sun’s activity level effects the climate on Earth today, and in the past, e.g. by the well known Maunder minimum from 1645–1715, for which a greatly reduced activity level could have been responsible of the Little Ice Age (Eddy, 1976).

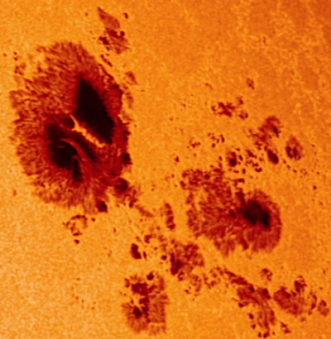
With a common need of knowing high accuracy stellar bulk parameters in stellar activity, exoplanet studies, etc., Asteroseismology, the science of stellar oscillations, has become a pivot for obtaining these. To the characterization of stellar activity of solar-type stars, asteroseismology have provided tremendous insight especially from the first big “cusp” in activity-asteroseismology analyses coming from the nominal mission of the NASA satellite Kepler Borucki et al. (2012); Koch et al. (2010), observing several hundred stars in the short cadence. Shown by results spread across a vast list of literature (e.g. Chaplin et al., 2007; Metcalfe et al., 2007; Kiefer et al., 2017; Karoff et al., 2019), with Kepler it was finally possible to complement activity measurements on stellar cycles, first with the correlation between acoustic oscillations (p-modes) and stellar activity cycles and, secondly, from the asteroseismic insight into stellar convection zone depths and differential rotations, which is most valuable to understand the magnetic *dynamo* driving stellar activity. Thus the next “cusp” in stellar activity may await from asteroseismic results of the NASA’s ongoing Transiting Exoplanet Survey Satellite (TESS), as precise determinations of stellar radii, masses, and ages (plus occasionally differential rotations and convection zone depths)

possibly will be determined for the complete stellar sample of the HK Project.

With the exceptional time coverage of a substantial stellar sample, the MWO survey still to this date yields the present reference database for magnetic activity in solar-type stars, and the basis of our understanding on the relationship between magnetic activity and variability on fundamental stellar properties (Hall, 2008). Nevertheless, during the 21st century, stellar activity studies now generally draw observations from an increasing diverse number of sources such as large-scale RV surveys of exoplanets (e.g. HARPS (Lovis et al., 2011) among others), and additional dedicated stellar activity surveys like the Lowell Observatory (Hall, 2008), SMARTS (Metcalfe et al., 2009), TIGRE (Schmitt et al., 2014), and LCOGT (Siverd et al., 2018). All these “second generation” projects follows the Mount Wilson “recipe” as closely as possible in order to produce comparable Ca II H & K emission estimates. The *S* index has therefore become the standard way of measuring chromospheric activity in stars. Although now more than half a decade after the initiation of the HK Project, only a handful of studies mentioned above, do actually focus on the long-term behavior of stellar cycles.

Since the majority of projects acquire spectroscopic observations from highly stable (and thus expensive) spectrographs, in addition to the high competition for monitoring programs and observing time in general, it is a small wonder, to why so few projects have emerged. Thus, a cheap and efficient, though precise, way to monitor stellar cycles for a long time is needed. Such considerations naturally placed the seed growing into the idea of using a commercial spectrograph mounted on a robotic telescope to trace stellar activity Karoff et al. (2019), which is the base of this project.

We will in Chapter 2 start by introducing the basic theoretical foundation of stellar activity, which will include aspects of stellar structure, astronomical spectroscopy, and research within stellar magnetic activity. Next, in Chapter 3 we will illustrate the fundamental aspects about spectroscopic instrumentation, which leads us to the actual project instrumentation. Connecting to the our instrumentation, in Chapter 4 important observational constraints, which have effected our selection of a stellar sample, will be presented, and the actual observations will be presented. The spectroscopic pipeline to reduce all data is presented in Chapter 5, and the results are presented and discussed in Chapter 6, together with the considerations to the performance of the spectroscopic setup. Lastly, Chapter 7 will be left for a summation of future prospects and a conclusion of this work.



2. Stellar Activity

Thematised by this SDO chapter image, of the Sun's visible continuum of the photosphere imprinted by dark sunspots, we will in this chapter enter the realm of stellar activity in context to the lessons learned from astronomical spectroscopy and stellar structure. This knowledge will be useful in the selection of targets and how to interpret their spectra.

2.1 Basic concepts

Starting from scratch, per definition spectroscopy is the study of the interaction between matter and light. Light is a electromagnetic wave that in vacuum propagates with the speed $c \simeq 3 \times 10^8 \text{ ms}^{-1}$ and although light, as a particle, is massless it transfer energy $E = h\nu$, which dependent on its frequency ν (or wavelength $\lambda = c\nu^{-1}$), where h is Planck's constant. Hence, the higher the frequency (or the shorter the wavelength) the higher the energy. Looking at the wave-particle duality of light, interactions with matter may be more intuitive in the framework of a quantum mechanical particle called a *wave packet* or a *photon*. For each photon we can associate an oscillation of the same frequency of the corresponding electromagnetic wave, but the transfer of momentum of a photon from its particle-like nature directly links to the classical interpretation of conservation of momentum during an interaction, compared to the framework of a wave.

Matter is on the other hand any substance that has mass and therefore physically occupy a volume in space, but ultimately consist of atoms. Atoms in turns are made of interacting subatomic particles (quarks) and each atom has a specific number of electrons occupying certain allowed energy levels in accordance to Quantum Mechanics. Thus, when an atom change, between two different electronic states of a single electron, a photon with the exact same energy difference between the states will be emitted or absorbed depending on, if the atom is initially exited or if it is to become exited. Thus, since each atom of a specific element has its own structure, the possible combinations of energy changes for the electrons are specific to that element and therefore, each element has its own “finger print” in the form of an *emission spectrum* and *absorption spectrum*.

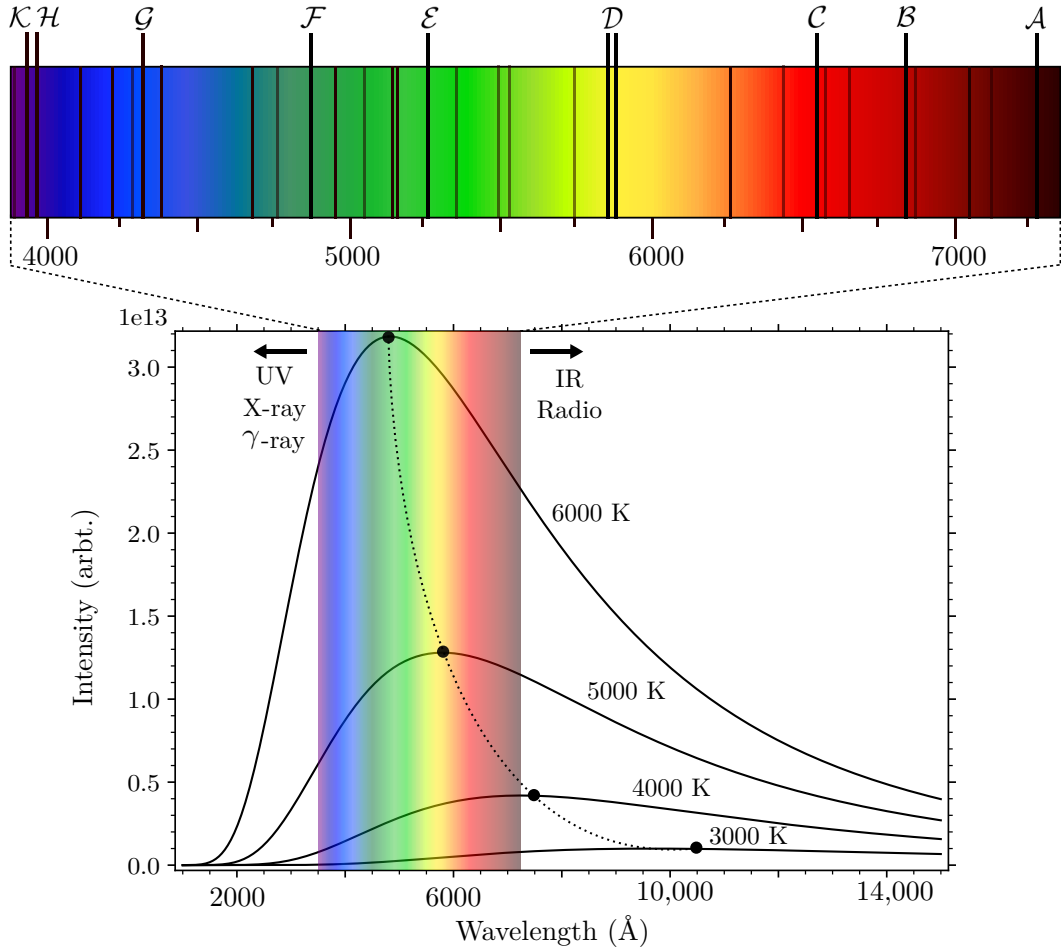


Figure 2.1: Illustration of the Sun’s continuum: Bottom panel shows the Planck radiation for blackbodies of four different temperatures (—) (4000 K, 5000 K, 6000 K, and 6000 K), and the wavelength of Wien’s law of maximum emission is likewise indicated (···). These curves were created using Planck’s law in term, of spectral radiance as intensity (Planck, 1914). The top panel is an enlarged illustrative view of the solar spectrum and the most dominant spectral lines are marked, including the Fraunhofer absorption lines indicated with letter from \mathcal{A} to \mathcal{K} .

A natural consecutive question is then, “how does a stellar spectrum look like?”. By simple reasoning, the answer is ambiguous, since it first of all depends on the star (effective temperature, abundance, gravity, etc.) and, secondly, on external factors such as the spectrograph, telluric lines if observing from ground, reddening/extinction from interstellar dust, etc. On the other hand, illustrated in the lower plot of Fig. 2.1, the overall shape of a stellar spectrum, also called the *continuum*, is primarily described by the *Planck function* which only depends on temperature under the assumption that stars emit as a blackbody¹ in thermal equilibrium. The stellar spectral sequence OBAFGKM(LT) describes this and is effectively a temperature sequence ranging from hot to cold (also referred to early and late spectral types), respectively, for which stars of different T_{eff} is assigned to a certain *spectral class*. For each spectral class a sub-divisions from 0-9 exists where 0 corresponds to the hottest star.

¹A black body is an idealized object that absorbs all incident light, regardless of frequency and angle of incidence. A black body in fully thermal equilibrium has the property of emitting in all ν in accordance to its thermal state (temperature) and do so isotropically. (Planck, 1914)

To complete the crude description of stars, a *luminosity class* is used as an indicator of the total radiance. Assuming yet again that stars are perfect spheres that emit like a blackbody, the *luminosity*, being the amount of energy radiated from the stellar surface per unit time, can then be expressed by

$$L = 4\pi\sigma T_{\text{eff}}^4 R^2 \quad (2.1)$$

with σ is the Stefan-Boltzmann constant and R is the stellar radius. Evident from (2.1) the luminosity relates to the radius by $L \propto R^2$, and thus the luminosity class ranging from I-V outlines stellar sizes of super-giants (I), bright-giants (II), giants (III), sub-giants (IV), and main-sequence or dwarf stars (V). Intuitively following from stellar structure and evolution, the mass and age of a star (and the chemical composition and stellar rotation to a lesser extend) determines L , R , and T_{eff} . Thus, by the invert calculation using a $\log T$ vs. $\log L$ plot, named by the two (independently) discoverers, the famous *Hertzsprung-Russell* (HR) diagram is one of the most powerful tools to determine the evolutionary stage of a star (Kippenhahn et al., 1990).

Stars Spectral Energy Distribution (SED), however, deviates from an ideal blackbody spectrum mainly by the presence of absorption lines (and to a smaller extent of emission lines). Illustrated in the top panel of Fig. 2.1, is a schematic view of the Sun's optical spectrum together with the dominant Fraunhofer absorption lines indicated with the letters from \mathcal{A} to \mathcal{K} . Generally defined as the transition region from the stellar interior to the interstellar medium, a stellar atmosphere can roughly be divided into four different layers: *sub-photosphere*, *photosphere*, *chromosphere*, and *corona*. Absorption lines originates from the stellar photosphere and the depth and strength of the lines are described by the atomic ionization and excitation stages through the Saha and Boltzmann equation, respectively. Both equations depends heavily on stellar effective temperature, surface gravity, and abundance. Not surprisingly, spectroscopy thus serves as one of the most accurate methods in determine these physical parameters.²

2.2 Chromospheric activity

While the stars provide a branch for atmospheric studies across a range of stellar masses and ages, the vicinity of Sun allows high-resolution observation of what we can hope is a typical stellar atmosphere, which we can use as a stepping stone to test hypotheses about stellar atmospheres in general and hence stellar structure and evolution. However, drowned in radiation from the photosphere, the Sun's outer atmosphere was first confirmed to be of solar rather than terrestrial origin in the 18th century during total solar eclipses. This stunning result accelerated spectroscopic studies of the extended corona, first observed by scattered photospheric light, and the chromosphere, first noticed as a pink ring of H α emission at the solar limb together with “red flames” or so-called *prominences*.

These phenomena raised several important questions about solar and stellar activity, which for the majority lead back to their origin, namely, “what is activity?”. It turned out that the complexity of this seemingly simple question at the time of writing still feed unsolved questions in solar and stellar magnetic dynamo theory, and the definition itself of a stellar chromosphere. Presently coined as stellar activity, the profound connection between the Sun's activity and its chromosphere was discovered by a broad range of phenomenas, for which the first observations, initiated by the invention of the telescope in the beginning

²With a typical precision for FGK stars of $T_{\text{eff}} \sim 80\text{K}$, $\log(g) \sim 0.08\text{dex}$, and $[\text{Fe}/\text{H}] \sim 0.07\text{dex}$, respectively. (Gray, 2005)

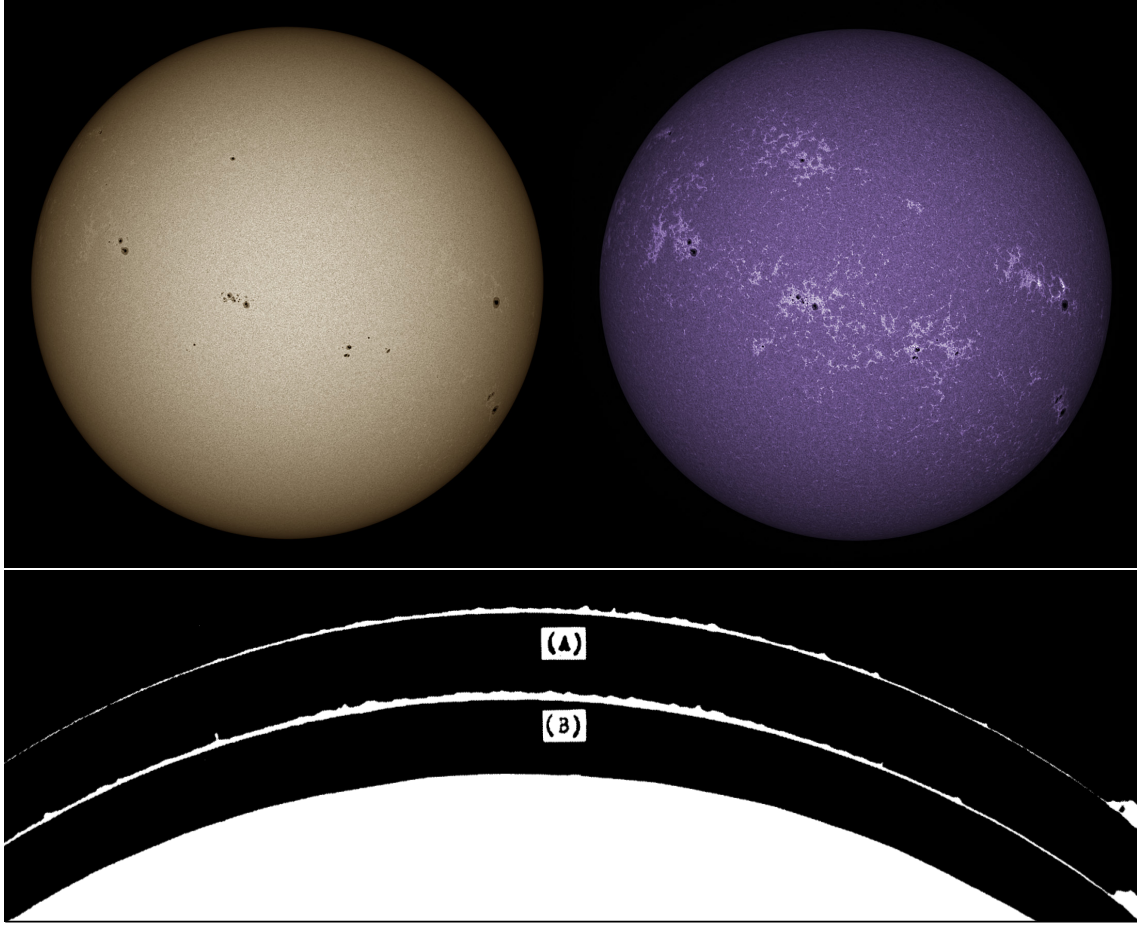


Figure 2.2: Top: Photographs of the Sun in optical (left) and Ca II K (right) emission observed by Pedro Ré on March 23, 2014. These images clearly demonstrate the coupling between sunspots and plages (bright chromospheric emission networks), and that chromospheric activity is magnetic of origin. Bottom: Photographs by [Roberts \(1945\)](#) of chromospheric prominences near the Sun’s north pole during the solar eclipse on February 3, 1944. Only about 8 min apart, image (A) and (B) shows the rapid evolution of chromospheric prominences: those visible in image (A) disappear and new ones emerge in image (B). Compared to the original illustration (PLATE VI) by [Roberts \(1945\)](#), this figure has been vertical compressed for a more clear comparison of the prominences.

of the 17th century, were variability changes and dark spots on the solar surface. By monitoring the dark *sunspots*, beautifully illustrated both in the SDO chapter image and the top left image of Fig. 2.2, the solar cycle was discovered.

A major breakthrough answering the question at hand happened within the infancy of photographic plates, with [Roberts \(1945\)](#) observations of the detailed spike-like structure of the chromospheric prominences, or *spicules* as he called them. Seen in the lower photograph of Fig. 2.2 he noticed that spicules’ and evanescent features of the chromosphere are highly variable on short timescales, with prominences appearing and disappearing within about 8 min between photograph (A) and (B). Realizing that prominences are collimated jets of plasma streaming out through the chromosphere, revealed the shared magnetic nature of prominences and sunspots – also evident from the shared location of the sunspots (left) and accumulation of chromospheric Ca II K emission (right) seen in Fig. 2.2. Thus, it is quite clear that activity itself defines the chromosphere to a significant extent and vis versa.

2.2.1 Stellar chromospheres

Although the word *chromo-sphere* by itself indicates a figuratively description of an intermediate region in the atmosphere of a star, the inhomogeneous magnetic topology of the solar surface, seen in Roberts (1945) photographs, clearly demonstrates why a simple chromospheric model of a well-defined layer will be incomplete, and great care must be taken when speaking about model parameters like height and temperature. Nevertheless, lessons are to be learned e.g. considering Vernazza et al. (1981) “toy-model” of the solar chromosphere seen in Fig. 2.3. By relating atmospheric temperature T and atmospheric scale height h (with h increasing right-to-left away from the solar surface zero-point) this diagram reflect a crucial aspect, for understanding activity: After falling from about 6500 K down to 4500 K through the photosphere, the rise in temperature reaches an extended plateau of about 7000 K, to all of a sudden jumping to more than 1 MK in the corona. Hence, this simple model suggests that a chromosphere (at least for the Sun) by physical terms lie above the photosphere and below the corona. Secondly, contrary to transport of energy happening almost purely by radiation in the photosphere, in so-called Radiative Equilibrium (RE), the physical extent of the temperature rise illustrated in Fig. 2.3, together with the detection of high-temperature ionization species, shows that additionally non-RE processes within the chromosphere are needed, to explain the outgoing energy transport (Hall, 2008).

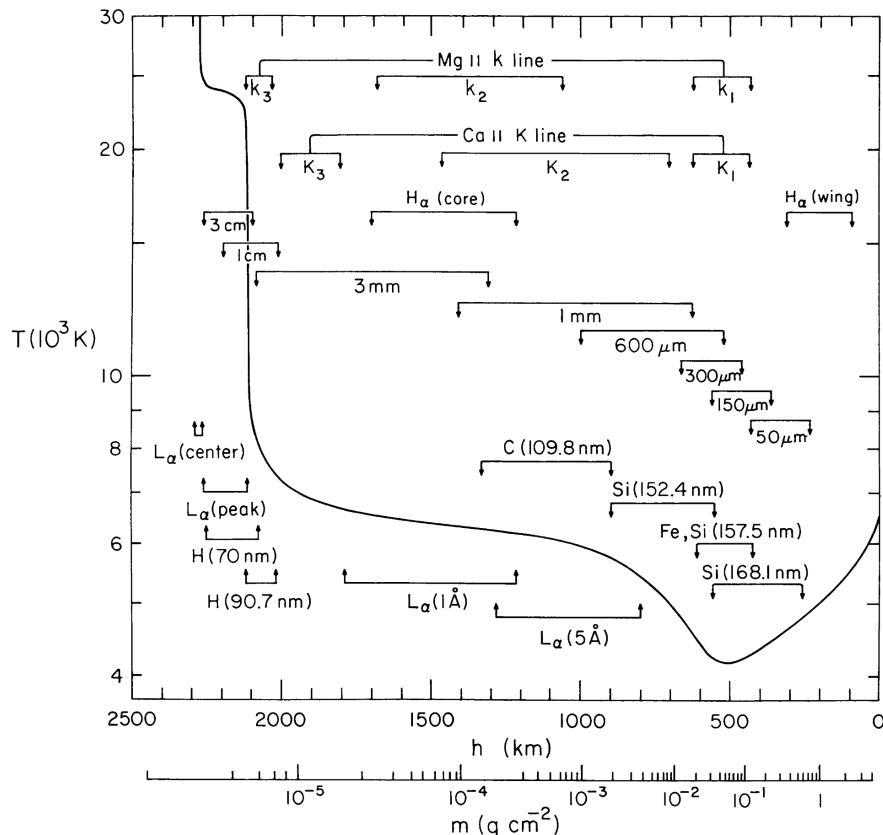


Figure 2.3: Chromospheric toy-model of the Sun from Vernazza et al. (1981). The solid line shows the atmospheric temperature derived from a semi-empirical model of the solar chromosphere, along with the formation heights of important lines and continua. Suggestive from this illustration the solar chromosphere lies somewhere between the temperature minimum at about 500 km and the steep rise towards transition region and coronal temperatures at about 2200 km.

By avoiding model parameterizing with height and temperature, one may define a chromosphere (on the cost of complexity) less crudely saying: A chromosphere is a region in the atmosphere where (I) lights excess from non-RE processes is observed and, (II) where cooling occurs mainly by radiation in strong resonance lines (rather than in the continuum as is the case of the photosphere) of abundant species such Mg II and Ca II. Hence, from this definition it immediately stems that a real chromosphere at a certain time may look radically different from an “average” chromosphere presented in Fig. 2.3.

2.2.2 Self-sustaining dynamo

Although activity is visible elsewhere in the outer atmosphere of the Sun, the “location” of the chromosphere right above the photosphere closely relates it to the physical processes at the surface and sub-surface. In fact, the main ideas behind the driving of activity, directly correlate the energy generation from these phenomenon to the non-RE temperatures reached in the chromosphere. To date the theory of greatest observational support was proposed by Babcock (1961), and explains an dynamo of a overall self-sustaining magnetic field driven by sub-surface convection. Clearly, such a self-sustaining dynamo directly explains the nature of sunspots being local areas on the solar surface where energy transport is suppressed by strong magnetic fields, and thereby the existence of the sunspot cycle itself. Stellar magnetic fields have also been found to account for most of what we observe as activity in the chromosphere and corona, via heating by *magnetohydrodynamic waves* (also known as Alfvén waves) or transport of mechanical energy into the outer atmosphere along magnetic “conduits” equivalent to the prominences seen in Fig. 2.2 photographed by Roberts (1945). Alternative theories for the feeding of solar activity (e.g. considering the dissipation of energy from granulation), however, cannot explain the combined set processes and phenomena coined as activity (Hall, 2008).

Considering again Fig. 2.3, it is now clear that the release of acoustic and mechanical energy into the atmosphere overlaying the mainly neutral photosphere, induces an increasing non-RE heating of the plasma as the opacity increases throughout the atmosphere. A cooling balance to the non-RE heated plasma happens as a result of an increasing hydrogen ionization of the plasma, thus releasing a huge amount of free electrons for the radiation to collide with. Creating a temperature plateau, seen in Fig. 2.3 the cooling “shield” provided by the free electrons only last so long, and at $T \sim 8000\text{K}$ the plasma is eventually fully ionized and loses its ability to cool, hence, explaining the rapid temperature increase from the chromosphere to the corona. Thus, ionization of hydrogen is likewise an essential component to the definition of a chromosphere.

2.2.3 Chromospheric HR-diagram

We have seen so far that chromospheric activity is tightly linked to changes in the stellar magnetic field, and the definition itself, therefore strongly suggesting which stars that might show chromospheric activity. Namely, first stars with an extended atmospheric region where the chromospheric definition (I) and (II) is fulfilled. Not surprisingly, this is the case of cool stars, as they have a great reservoir of neutral hydrogen available, being clearly absent for hot stars. Secondly, any theory advanced so far imply the presence of surface convection, e.g. for the theory presented above, a sub-surface bulk mass transport is needed to sustain a self-generating magnetic dynamo. Hence, we might shortly dive into the basics of convectional energy transport.

Convective transport deals with buoyancy of blobs of material moving outwards, dissipate their energy at some transition layer, and then move back inwards again. For convection to occur we need *instability* such that the blobs of gas can move. In short, assuming that each blob moves adiabatically outward, meaning the motion is slow enough to ensure pressure stabilization and fast enough to avoid heat loss to the surroundings, an instability in the plasma will then happen when the temperature gradient ∇ is

$$\nabla = \frac{d \ln T}{d \ln P} > \nabla_{ad} \equiv \left(\frac{\partial \ln T}{\partial \ln P} \right)_{ad} \quad (2.2)$$

Circumstances under which one may expect convection, is easiest considering a stellar model where energy transport takes place through radiation – hence, the case of RE where all energy is transported outwards by photons. Looking at the photon mean free path $\lambda = 1/(\kappa \rho)$ (with κ being the opacity and ρ the density), the radiative flux, and energy density, one may derive the radiative temperature gradient

$$\nabla_{rad} = \frac{3}{16\pi acG} \frac{\kappa(r) L(r) P(r)}{m(r) T(r)^3} \quad (2.3)$$

Since radiative transport is always present, convection can only exist when energetically preferable, which is when the condition for *convective instability* is fulfilled

$$\nabla_{rad} > \nabla_{ad} \quad (2.4)$$

Considering both (2.3) and (2.4) we thus directly expect to find a convective envelope for stars where either κ is large, ρ/T^3 is large, or ∇_{ad} is small. For all three cases this is satisfied in the outer parts of relatively light and cool stars, i.e. light stars on the main-sequence and evolved red-giant stars. The two former cases originates directly as a consequence of a low T_{eff} , since $\kappa \sim \kappa_0 \rho T^{-3.5}$ increases with temperature and ρ/T^3 explicitly. Having a small ∇_{ad} is usually satisfied in the ionization zone of hydrogen, i.e., again in the outer parts of cool stars Christensen-Dalsgaard (2008).

For illustration Fig. 2.4 shows the “evolution” of approximate locations for which energy transport by convection (wave-shaded areas) and radiation (plain colors) takes place inside main-sequence stars as function of stellar mass. Evidently with increasing stellar mass, there is a gradual transition between surface convection and core convection, since the average rate of energy generation per unit mass within r , expressed by $L(r)/m(r)$, increases with mass and thereby fulfills (2.4) towards convective instability. Thus, the main point from Fig. 2.4 is that surface convection, and thus the expectation of chromospheric emission, for

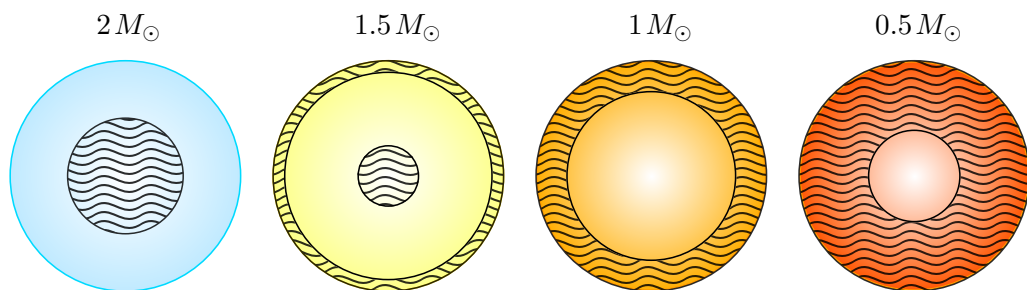


Figure 2.4: Illustration energy transport zones in main-sequence stars of different masses. Convective zones are indicated by wavy-shaded areas, and elsewhere is radiation dominated zones. The color of each star is approximative to its effective temperature.

main-sequence stars, will be present roughly up to late A type stars (with $M \sim 1.6\text{--}2.4M_{\odot}$ and $T_{\text{eff}} \sim 7000\text{--}10.000\text{K}$) – in perfect agreement with [Simon et al. \(2002\)](#)’s study of A type stars, showing that chromospheric emission is visible for stellar temperatures as high as 8250 K. Towards the fully convection zone limit for low mass stars is a review in itself, however, from observations it is clear that the solar-like stars (FGK types) in our interest, clearly exhibit the chromospheric emission expected from the theoretical discussion above. Hence, only stars on the cool half of the HR-diagram, lives in a “chromospheric HR-diagram”.

2.3 Stellar chromospheric activity research

Before moving on, we now have the foundation to understand and fully appreciate the work of dedicated researchers, that have brought us to our present scientific position. It may be provocative to say that “*despite the volume over which it is distributed, the mass of the solar chromosphere is only about the mass of Earth’s atmosphere; moreover, the mass of the photosphere down to an optical depth of one in the continuum is only about that of the Indian Ocean!*” ([Hall, 2008](#)). However, whether trying to understand or mitigate the effect of stellar chromospheric activity, its massive influence is evident in almost all stellar and planetary studies of modern day astronomy.

Mentioned in the introduction, the HK Project at the Mt Wilson Observatory (MWO) is the single largest archive of chromospheric data of today. Thanks to Olin Wilson’s successor Sallie Baliunas, the MWO program was kept alive until 2003, being time enough for other dedicated surveys, like at Lowell Observatory, to take over and continue the solar-stellar legacy. This legacy of (what seems to be a complete) calibrated and self-consistent observations from 1966 to mid-1995, was actually found during 2015 at the National Solar Observatory (NSO). The early theoretical foundation presented above was the leap for the HK Project, and as such, the fostering of the activity proxy S used to trace stellar activity of solar-type stars. However, one might wonder to why the Ca II H & K lines was used for the measure of activity in the first place, since other lines like the Mg II h & k shows a much higher level of chromospheric emission (due to its 15 times higher abundance). At the initiation of the HK Project, observations were only made from ground, and apart from a very limited amount of lines, such as Ca II H & K and $H\alpha$, chromospheric lines lie in the UV or beyond and are not accessible from the ground. Thus, the HK Project exploited the strongest observable spectral features from ground, namely Ca II H & K lines. The reasoning behind the specific composition of the S index then came from the physical ground that using two pseudo-continuum bands $V + R$ as normalization factor, S is essentially the residual intensity of $H + K$, hence the actual chromospheric flux excess measured from the Ca II H & K line cores themselves. By the discussion above, they therefore clearly proved to be a useful proxy for the strength of magnetic fields, but also the fractional area covered by magnetic fields.

From the complex and cyclic definition of chromospheric activity, it may not be that surprising to learn that long-term magnetic variability manifests in cyclic, flat, and irregular variability as first was found by [Baliunas et al. \(1995\)](#). [Wilson \(1978\)](#) noticed early on that activity cycles decreases with stellar age, which was the underlying basis for the discovery that a “bifurcation” in activity cycles exist for solar-like stars; one active and one inactive ([Saar and Brandenburg, 1999](#)), and that the Sun may be in a transition also known as the *Vaughan-Preston gap* ([Vaughan and Preston, 1980](#)). A detailed analysis of the MWO survey suggested that a rapid increase in the relation of the cyclic and rotational period

$P_{\text{cyc}}/P_{\text{rot}}$ occurs at a stellar age of around 2–3 Gyr, switching stars from a young active to an old inactive branch. Böhm-Vitense (2007) suggested based on the fact that the number of rotations during a cycle seems to be different between the two subgroups of stars, the bifurcation may be caused by different dynamos operating in the two branches. From ensemble studies, of a large number of MWO stars with poorly constrained fundamental properties, it seems likely that the Sun is in fact special, owing to its location inside the Vaughan-Preston gap, together with its unusually low photometric variability compared to other solar-type stars. The correct path to unraveling this question may takes us down many different roads, however, it is clear that well constrained fundamental gross stellar properties in combination to chromospheric data offers a shortcut, compared to the activity proxies alone.



3. Instrumentation

Spectroscopy have for a long time been very expensive technique, mainly due to the high costs of stable high-resolution spectrographs. Accordingly a new market within commercial échelle spectrographs is growing, and the foundation of this thesis is build upon one such spectrograph, namely the *eShel*. Although a detailed mathematical exposition of spectrographs is beyond the scope of this project, some basic principles is needed in the forthcoming. In this chapter we will also introduce the installation and integration of the eShel-SONG spectroscopic system, *BlueSONG*.

3.1 Breaking down a spectrograph

A spectrograph is a scientific instrument that disperse light into a spectrum. With a spectrograph integrated inside a spectroscopic system, conceptually, such a system is composed of five main types of components

1. Slit or a fiber serving as the light interface/feeding with the telescope
2. Collimator
3. Dispersive element(s) like a prism, échelle grating, or grism
4. Objective like a camera lens
5. Detector

The light interface serves two purposes: first to select the target of interest within the telescope's Field Of View (FOV), so that only the light from this target is feed to the spectrograph¹ and, secondly, to spatially define the resolution element of the spectrograph as this is the initial image feed to the spectrograph. Illustrated in Fig. 3.1 (a) a slit is a mechanical aperture with a elongated rectangular gap, whereas (b) a fiber is a (silica) glass tube working as a wave-guide by the principle of total internal reflection (Barden, 1988).

¹Obviously, compared to using a fiber, a slit as the light interface allows simultaneously spectral observation of multiple targets if fitted within the length of the slit.

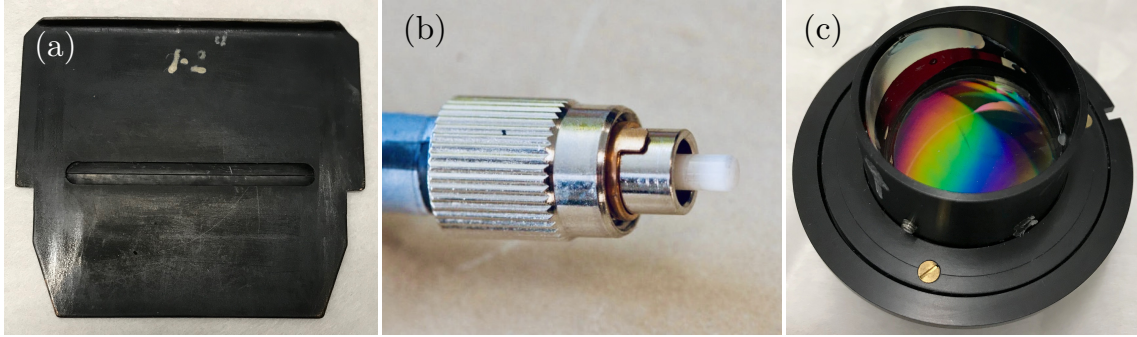


Figure 3.1: Schematic view of (a) a slit, (b) a fiber, and (c) a grism. The slit and grism are optical elements used at the NOT, and the fiber-head image from shelyak.com shows the 50 μm core diameter entrance of the object fiber used for eShel.

The simplest spectrographs only have a single dispersive elements being a prism, grating, or a grism. These dispersive elements comes in a variety of shapes and classifications, and being the most common, a prism is a block of glass with a triangular shape with at least two polished surfaces. Seen in Fig. 3.2 (A) when a parallel beam of monochromatic light enters one of the polished faces, the light is refracted according to Snell's law which depends on the refractive index n of the glass (Schroeder, 1999). Unfortunately, the angle of dispersion that can be achieved with a prism is very low, and as a consequence the ability to disperse light into different wavelengths is rather limited. Illustrated in Fig. 3.2 (B) a diffraction grating is on the other hand a block of glass with a multitude of closely packed grooves, thus allowing much higher dispersion angles. The density of grooves is specified by the *grating* which typically spans from 10–1200 grooves per millimeter for different spectrosopes (Schroeder, 1999). As equidistant grooves can reach down to a few hundred of a nanometer, each basically works as a slit and the domain of diffraction is reached. Lastly, as seen in Fig. 3.1 (c), a grism is a combination of a prism and a grating meaning the light transmitted through such an optical element disperse in accordance to the theory of refraction and diffraction, allowing an even higher angle of dispersion.

From the theory of diffraction light incident on a reflection grating obey the diffraction equation (Palmer and Loewen, 2005)

$$\begin{aligned} m\lambda &= d(\sin \beta + \sin \alpha) \\ \Rightarrow \quad \beta(\lambda) &= \sin^{-1} \left(\frac{m\lambda}{d} - \sin \alpha \right) \end{aligned} \tag{3.1}$$

where α and β is the incident and diffraction angle of the light rays measured relative to the grating normal, respectively, d is the separation between the grooves (also called the grating constant), λ is the wavelength of the light, and m is the order of interference. The angular dispersion is then simply given by the derivative of β

$$\dot{\beta}(\lambda) = \frac{m}{d \cos \beta} = \frac{\sin \beta + \sin \alpha}{\lambda \cos \beta} \tag{3.2}$$

where the Pythagorean trigonometric identity was used to provide the first equal sign and (3.1) to provide the second. From (3.2) it follows that for a given λ the angular dispersion depends only on α and β .² The importance of these two equations is the existence of

²Note that also transmission gratings exists (the example of grisms) for which the sign in (3.1) and (3.2) is opposite.

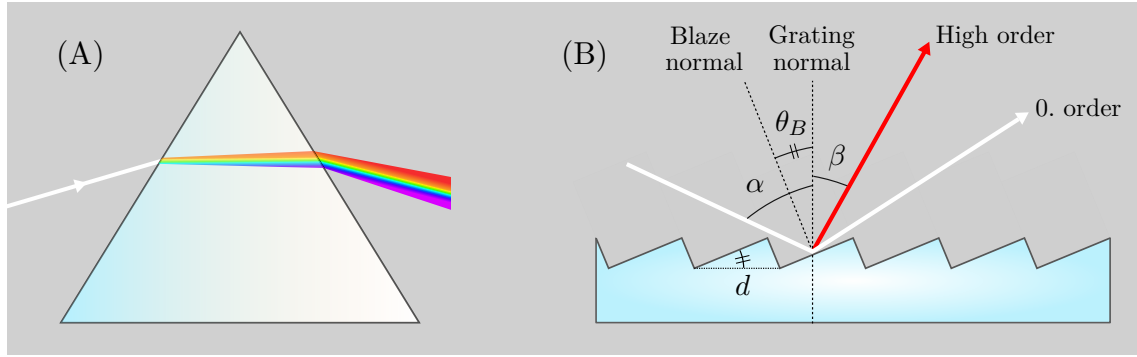


Figure 3.2: Schematic drawing of light diffracted by a (A) prism and (B) an reflective échelle grating. Important parameters of an échelle grating is the incident (α) and diffracted (β) angle of the rays measured relative to the grating normal, the separation between the grooves (d), and the blaze angle (θ_B) defined from the grating normal. Notice that a setup corresponding to panel (B) is good for illustration but far from optimal in terms of efficiency.

multiple solutions with different m values, which ultimately leads to a superposition of different orders along a given β . It can be shown that the maximum efficiency of an ideal grating occurs at reflection when $m = 0$ (hence $\alpha = -\beta$) and decreases rapidly with increasing solutions of $|m|$. However, this zeroth order maximum is of no use because it does not provide any discrimination in wavelength.

Also in real life keeping the instrument size small for stabilization and practical reasons means that the best optical design is close to the *Littrow* solution of (3.1) when $\alpha = \beta$. Although this forces us to work at high m , hence in a low efficiency regime, by changing the so-called *blaze angle* θ_B , which is the angle between the normal of the grooves and the grating normal (see Fig. 3.2 (B)), a high efficiency can be restored. Thus, the efficiency is maximized when $\alpha = \beta = \theta_B$ which is called the *Littrow-Blaze* condition which most échelle spectrographs take advantage of.

3.1.1 Échelle spectrographs

From the discussion above of gratings, the different solutions of m , leading to a superposition of different orders along a given β , give rise to a fundamental problem: Only a small part of the spectrum can be studied with a high efficiency at a fixed grating. This lead naturally to the usage of échelle spectrographs where both a high efficient spectral detail over a large spectral range can be accomplished by first using an échelle diffraction grating (close to the Littrow-Blaze condition) and then a secondary dispersive element, which is orientated perpendicular to the grating and thus separates (cross disperse) the spectrum into different orders. The cross dispersion can either be done by yet another diffraction grating, a prism, or a grism, and the result at the detector focus is a latter-like stack of spectra from successive orders. Due to the geometry of an échelle spectrograph and its optics a raw échelle spectrum have curved orders.

From the the discussion above, for a given pair of α and β , the grating equation (3.1) is satisfied for all wavelengths where m is an integer. This means that there is an spectral overlap between successive orders, as two wavelengths λ and λ' are diffracted in the same direction as they fulfill $m\lambda' = (m+1)\lambda$. The wavelength difference, also known as the *free spectral range*, is thus given by $\Delta\lambda = \lambda/m$ (Schroeder, 1999). Échelle spectrographs avoid this spectral overlap confusion by cross dispersing each spectral free range onto successive

échelle orders. As we will see in Chap. 5 this is very handy, when working in near-UV wavelength and low Signal-to-Noise (S/N) ratio environments, where the free spectral range allows optimized spectral extraction. Altogether, échelle gratings are thus both specially designed to operate at very high orders (typically between $m = 30\text{--}150$), and intuitively designed for storing a large quantity of information given a sufficiently large surface area of the detector.

3.1.2 Spectroscopic parameters

The key parameter for a spectroscope is the *resolution*, $\delta\lambda$, and true for any imaging system the resolution is the smallest detail visible. With λ being the wavelength considered the spectroscopic *resolving power* is thus a unit-less measure of spectral detail

$$\mathcal{R} \equiv \frac{\lambda}{\delta\lambda} \quad (3.3)$$

Depending on the field of research, spectral resolving power may vary from $\mathcal{R} = 100$ (very low resolution) to $\mathcal{R} = 100,000$ (very high resolution).³ Hence, the choice of a spectroscope's \mathcal{R} are designed accordingly to meet observational constraints. Thus, for spectrographs two major trade offs persists: First between the resolution and the spectral domain observed, simply because of the size of the detector – the more we “zoom in” on the spectrum, the smaller the coverage of the spectral range. As mentioned, with échelle spectrographs this problem is solved to some extent. Secondly, a trade off between resolution and efficiency in terms the S/N ratio exists, as the same amount of light per unit time is distributed over more or less pixels in both dispersion and cross dispersion.

The latter trade off relates to the fact that resolution (in Å) and dispersion (in Å pixel⁻¹) are proportional with the *sampling* (in pixel) as the factor of proportionality. Thus only at a proper sampling are the resolution and dispersion equivalent. In fact from signal processing the Nyquist-Shannon theorem says that for an optimal detection, the smallest detail visible in the spectrum should cover at least two pixels (Gray, 2005). In practice a Full Width Half Maximum (FWHM) of 3 pixel would be a better choice to avoid sub-sampling, where the detector limits the visible details in the spectrum.

3.1.3 A homogeneous setup

Together with the dispersive element(s), a spectrograph needs optics, such as mirrors, a collimator, and a objective for guidance of the light rays. A collimator and objective may consist of a curved mirror or lens (or various combinations of the two) with a collimator serving the purpose of aligning light into a parallel beam and an objective of gathering and converge light rays coming from “infinity”⁴ to a point called *focus*. Lenses/focal reducers are in far most cases the combination of a collimator and objective and their practically functionality is to reduce (or adjust) the distance between the objective and its focus, the so-called focal length f . We define the optical axis of a lens from its axis of symmetry, and the focal plane is the plane perpendicular to the optical axis on which the focus lies. The

³E.g. from our discussion in Sec. 2.1 the aforementioned would fit stellar temperature measurements, as the Planck profile can be extracted from the wide-view-spectrum covering the entire visible spectrum, whereas the latter would be ideal for precise RV measurements or abundance analysis, for which two very close lines needs to be distinguished.

⁴In spectroscopic a source is generally defined to be infinitively far away if its distance to the spectrograph is greater than $100\times$ focal length (Cochard, 2018).

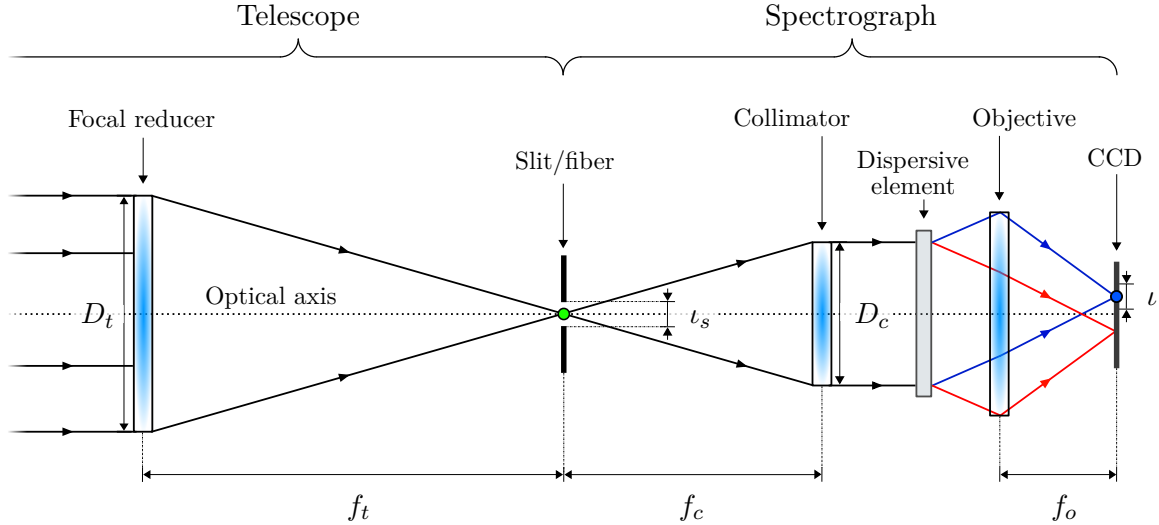


Figure 3.3: Schematic drawing of an optimal configuration between a telescope and a spectrograph with the focal ratios of the telescope and spectrograph being equal ($f_t/D_t = f_c/D_c$). This figure illustrates both the light path through a spectroscopic system and the basic components of a spectroscopic setup listed in Sec. 3.1, namely, slit/fiber, dispersive element, detector, and optics, and a focal reducer belonging to the telescope system as indicated above the setup. Notice that ι represents the slit/fiber image size.

focal ratio which is defined by (Bradt, 2004)

$$f_R \equiv \frac{f}{D} \quad (3.4)$$

with D being the diameter of the focusing optical element. By tradition the notation “ f/f_R ” will be used to indicate the focal ratio – i.e. if $f_R = 5$ this would be written as $f/5$ which is in fact the equating of D . Nevertheless, the important point here is, to obtain a homogeneous setup, the focal ratio (or F-ratio) of the telescope system and spectrograph system must be the same, meaning $f_t/D_t = f_c/D_c$. One such homogeneous configuration is illustrated in Fig. 3.3, where stellar light enters the focal reducer on the left, then passes through a slit or fiber,⁵ and is within the spectrograph collimated, dispersed, and focused by an objective onto the CCD tip. With an overview of a general spectroscopic system, it is time to introduce the eShel-SONG spectroscopic system.

3.2 BlueSONG

In addition to the considerations mentioned in the introduction, of the high cost and competing for observing time on modern spectrographs, the idea of using an commercial échelle spectrograph mounted on the fully robotic Hertzsprung SONG telescope on Tenerife (Karoff et al., 2019), was inspired by noticing that the main spectrograph at SONG is optimized to measures accurate RVs using a iodine cell, which covers the wavelength range 4900–6200 Å. In fact the Ca II H & K lines do not even fall on the detector.

⁵While using a fiber as the light interface it is less obvious why the telescopic and spectroscopic F-ratios have to equal, however, recalling that fibers works by the principle of total internal reflection, the incident and outgoing angle are the same and the setup remains homogeneous.

3.2.1 Installation & Integration

The eShel spectrograph was acquired in 2016 and installed on the 1 m Hertzsprung SONG telescope⁶, an Cassegrain-Coudé focus design on a on-axis Alt-Az mount, placed on the Teide Observatory, Tenerife.⁷ With the future prospect and potential of combining minimum 3-4 telescopes on each hemisphere to monitor the sky for all times, the node

⁶The chapter image shows Mads Fredslund's APOD image from 5th of May 2016: *SONG and the Hunter*.

⁷The installation was performed solely by Simon Holmbo, a PhD student from Aarhus University.

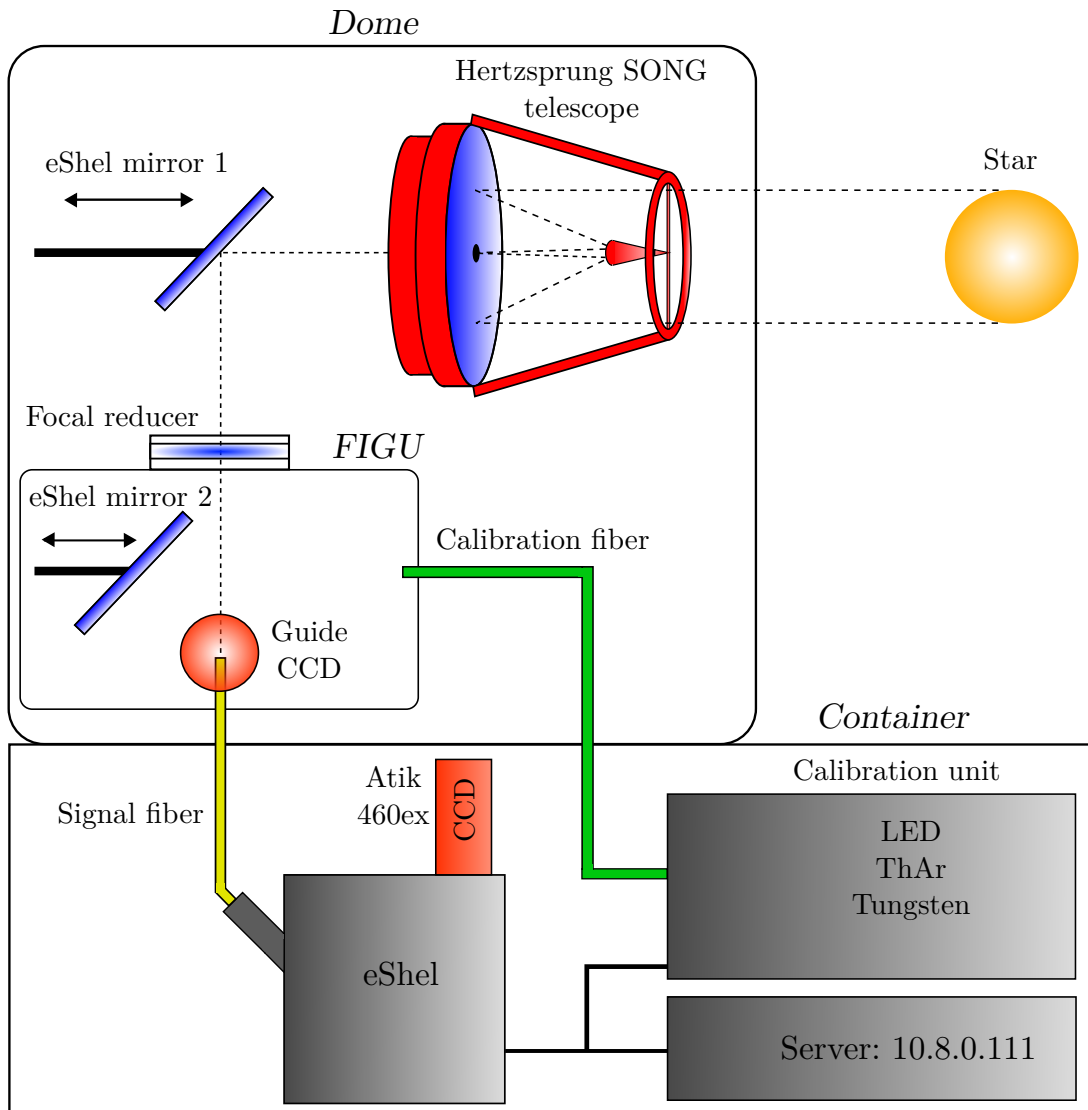


Figure 3.4: Drawing of BlueSONG; the instrumental setup of eShel on the Hertzsprung SONG telescope. From the top and downward the three main enclosed boxes represents the dome, the Fiber Injection and Guider Unit (FIGU), and Container, respectively. In science mode light from a distant sun is observed with the 1 m mirror telescope, which pass the light to the eShel mirror 1 (which is pushed into the ray path) reflecting the light into a focal reducer, which collimates the light, and pass it into the FIGU. A guide camera monitors how collimated light is received at the signal fiber, and through the fiber the starlight goes into the spectrograph. In calibration mode any of the calibrations lamps (LED, ThAr, or Tungsten) pass the light through the calibration fiber into FIGU where the eShel mirror 2 now is activated and reflects the light into the signal fiber and into the spectrograph.

on Tenerife (in the forthcoming only SONG) is for now the only telescope in operation.⁸ The site of the Teide Observatory (28.4746° N, 16.3081° W) provides approximately 220 photometric nights per year, and the total duty cycle of SONG since the scientific start of operations in early 2014 is 63.3% (Andersen et al., 2019). With only a technical downtime of 7.9% and the robotic flexibility of SONG makes it an ideal telescope for long term projects of measuring both stellar oscillations and tracing stellar cycles of close-by solar type stars, with the former being its main purpose.

Fig. 3.4 shows an illustrative drawing of BlueSONG with the three enclosed boxes being the dome, the Fiber Injection and Guider Unit (FIGU), and the container. During an observation stellar light collected by the telescope is from the nasmyth design (not shown in this illustration) send to the eShel mirror 1, a movable mirror placed on an optical bench. The light is then reflected into a lens (working as a focal reducer) which focus the light and pass it into the FIGU. Suggestive from the name the FIGU has attached a signal and calibration fiber together with a guide camera, and within the movable eShel mirror 2. In science mode a guide camera monitors how collimated light is received at the $50\text{ }\mu\text{m}$ signal fiber, and through the fiber the starlight goes into the spectrograph. In calibration mode, any of the calibrations lamps pass the light through the $200\text{ }\mu\text{m}$ calibration fiber into FIGU, where the eShel mirror 2 now is activated, and reflects the light into the signal fiber and spectrograph.

⁸Another node at the Delingha Observatory in China was operational in 2017 but is now being moved to a new location, and a new node (using two 0.7 m diameter mirror telescopes) has been initiated in early 2019 on Mount Kent in Southern Queensland, Australia. To see more visit <http://song.au.dk/>.

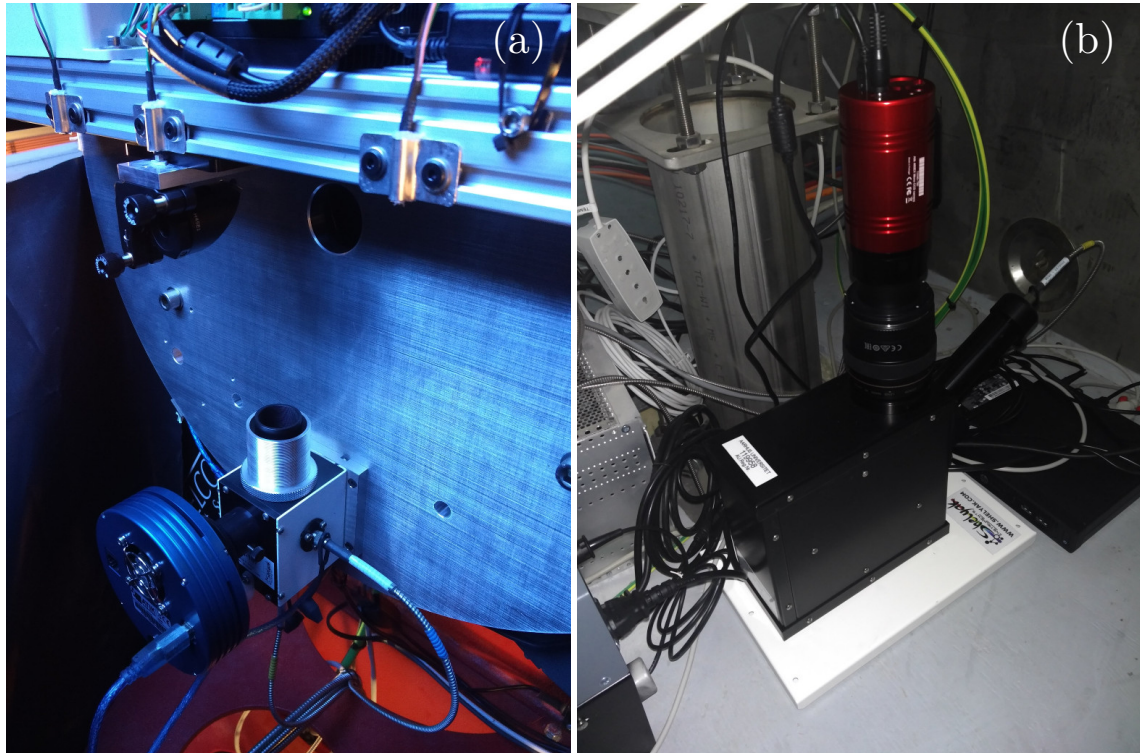


Figure 3.5: Setup of FIGU (a) and eShel (b). In (a) the eShel mirror 1 is placed on an optical bench seen in the top with the FIGU below having a Atik Titan guide camera and ThorLab lens-focal reducer installed. Not seen in (b) the eShel spectrograph and calibration unit are now placed inside a wooden box for protection.

Fig. 3.5 (a) shows the FIGU setup within the dome with the eShel mirror 1 on the optical slider-bench in the upper-left corner, a Atik Titan guide camera mounted on the of the FIGU in the lower left image corner, and a ThorLab lens-focal reducer mounted on top of the FIGU central in the image. Fig. 3.5 (b) shows the eShel spectrograph within the container before it was placed inside a wooden box for protection, and with the acquisition CCD from Atik attached on top, and the object fiber and server seen to the right.

3.2.2 Coupling eShel to SONG

In fiber-fed spectrographs, the photons collected by the telescope aperture are focused onto the fiber tip which, just like a slit, acts as a limiting aperture of the spectrograph. Thus, as we saw in Fig. 3.3 the size of the stellar disk image at the focal plane of the focal reducer should be comparable to the size of the limiting aperture: the fiber-head diameter. Thus, the *coupling efficiency* between the telescope and the spectrograph is defined as the fraction of the photons reaching the focal plane that enter the fiber. Performing with optimal coupling efficiency a homogeneous setup should already be provided by the manufacturer (Shelyak). To achieve optimal coupling efficiency with the telescope a $0.16 \times$ focal reducer was introduced between the telescope and the FIGU to match the $f/36.7$ focal ratio of the telescope to the $f/6$ entrance of FIGU. Using the small angle approximation to the plate scale equation $P_s = f^{-1}$ (hence the angle in radians that is imaged onto a unit length of the CCD), with this focal reducer the $50 \mu\text{m}$ entrance aperture of the signal fiber is equivalent to $1.7''$ on the sky plane.

3.2.3 The eShel spectrograph

The eShel is an “of-the-self”, fiber-fed échelle spectrograph manufactured by the French company Shelyak Instruments⁹. A transparent drawing of eShel seen in Fig. 3.6 illustrates how the light goes through the spectroscopic system. Light feed into eShel is first collimated by a collimator and then dispersed by a $50 \times 25 \text{ mm}$ R2 grating (blaze angle of 63.4°) with 79 lines per mm – from the discussion of Sec. 3.1 this corresponds to a *quasi-Littrow* configuration. Next a prism is used for cross dispersion and lastly a Conon lens focus the light onto the CCD tip. Already mentioned, in spectroscopy acquiring a homogeneous setup means keeping things as simple as possible. In fact the very basic homogeneous setup shown Fig. 3.3 is the exact setup of BlueSONG (if including the prism for cross dispersion), using a $f_t/D_t = 6/15.0 \text{ mm}$ focal reducer together with a $f_c/D_c = 5/12.5 \text{ mm}$ achromatic doublet collimator, nicely almost equaling to unity.

In comparison with the cost of other commercial spectrographs the eShel spectrograph was chosen for its good spectral qualifications. The standard setting of the high order échelle grating of eShel disperse the spectrum into a total of 21 orders, with default order usability from $m = 30\text{--}50$ spanning a wavelength range of about $4500\text{--}7600 \text{ \AA}$. However, at the cost of a focusing the Canon objective lens, it is possible to cover the near-UV down to 3900 \AA with the eShel spectrograph, which is needed to access the order containing the Ca II H & K lines at around 3968 \AA and 3934 \AA , respectively. Another configuration for probing into the near-UV will be discussed in Sec. 6.3, but accessing the near-UV domain by tuning the objective lens means only the Ca II H & K order (order #57) and parts of successive orders above and below can be properly focused onto the CCD simultaneously (as will be shown later in Fig. 5.2).

⁹<https://www.shelyak.com/>

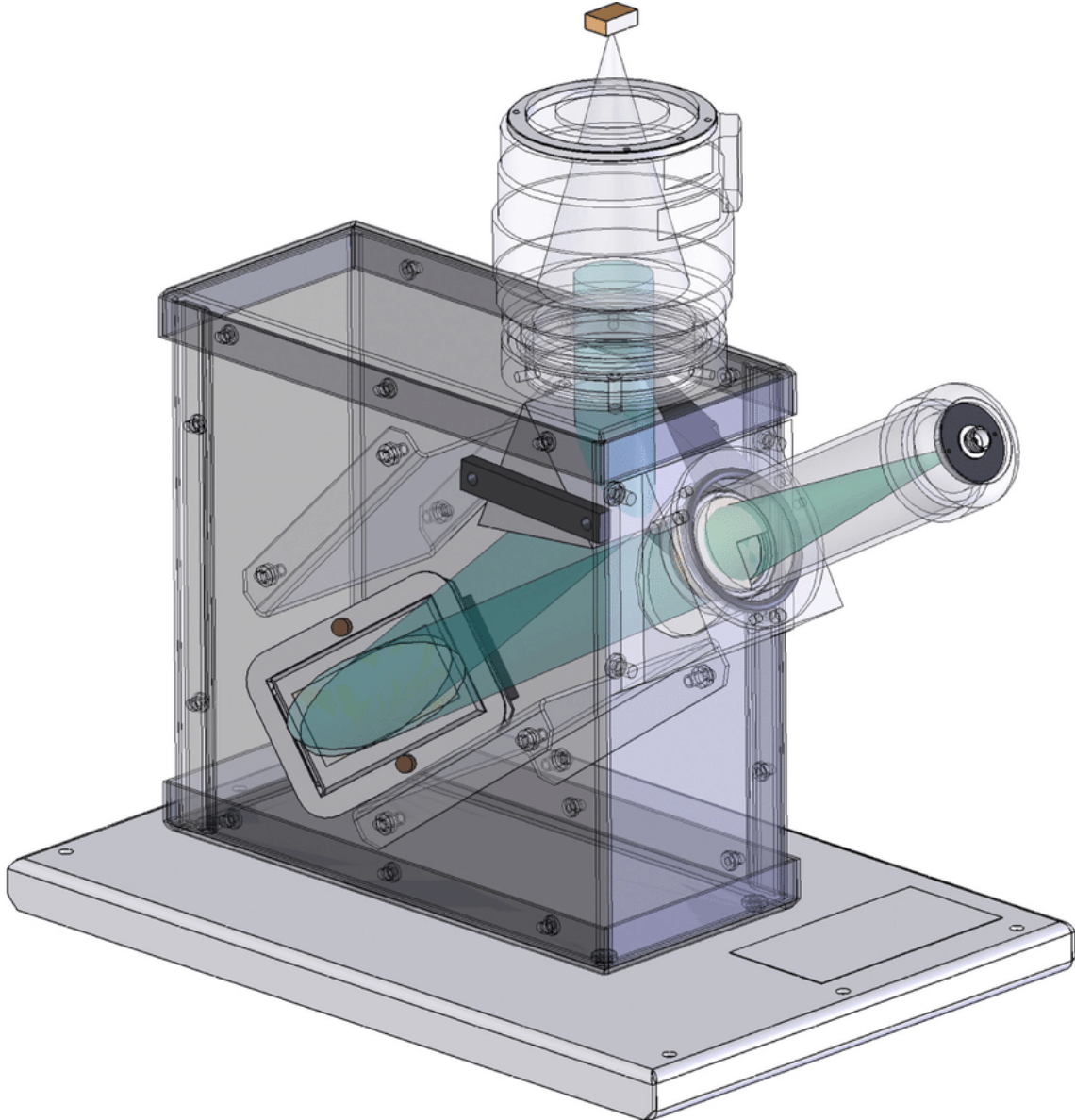


Figure 3.6: Transparent view of the eShel spectrograph. Light feed to the eShel is first collimated, secondly, dispersed by a échelle grating, thirdly, cross dispersed by a prism and, lastly, focused by a objective Canon lens onto the CCD tip. *Credit: Eversberg (2016).*

3.2.4 Detectors

Presented in Fig. 3.5, in this project we use an Atik 460EX mono CCD camera with a Sony ICX694 image sensor for science acquisition, and an Atik Titan mono (monochromatic) CCD camera with a Sony ICX424 image sensor for guide imaging. Like any other image sensors a CCD are a pixel matrix of a given size, and the specifications for both detectors can be seen in Tab. 3.1. Perfectly suited for astronomy the Atik 460EX has typically values of gain of $\sim 0.27 \text{ e}^- \text{ ADU}^{-1}$, Read-Out Noise (RON) of 5 e^- , a full-well of $\sim 18.000 \text{ e}^-$, and a dark current of $\sim 4 \times 10^{-4} \text{ e}^- \text{ s}^{-1}$ at a temperature of -10°C . The CCD can reach down to -25°C below the ambient temperature, which when placed inside the temperature stabilized container is around -10°C . Hence, the above mentioned appreciable dark current value is what we should expect. Depending on the type of CCD that is being used, the

Table 3.1: Specification of the Atik cameras.

Detector	Resolution (pixels)	Pixel Size ($\mu\text{m pixel}^{-1}$)	ADC (bit)	Cooling ($^{\circ}\text{C}_{\text{amb}}$)	RON (e^-)	Gain ($e^- \text{ADU}^{-1}$)	Full Well (e^-)
Sony ICX694	2750×2200	4.54×4.54	16	-25	5	0.27	18,000
Sony ICX424	658×492	7.4×7.4	16	-20	7	0.34	22,500

dynamical range of the detector determines how many counts in ADU each pixel can store before it saturates. Just like both detectors used in this project, the majority of CCDs used in astronomy are 16 (or 24) bit Analog to Digital Converter (ADC) CCDs, meaning saturation occurs at $2^{16} = 65.565 \text{ ADU pixel}^{-1}$.

3.2.5 Acquisition software

The eShel spectrograph and calibration unit can either be operated manually by the open-source astronomy software KSTARS¹⁰, or automatically with scripts written by Simon Holmbo. Two main scripts exists for which one acquire calibrations images (bias, dark, flat, and ThAr) each day at 12.00 UTC, and the second is used for observations and takes care of focusing the telescope, telescope guiding, and fiber acquisition using automated scripts for the Titan guide camera. For more details the reader is directed to Appendix A for the *BlueSONG Cookbook*, which is likewise a product of this work.

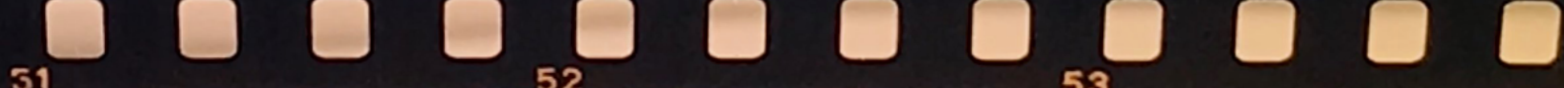
3.2.6 Technical instrumental work

Apart from observation and computation, technical work regarding ways to optimize the instrumentation BlueSONG is (and will be) the key ingredient for a successful outcome. Since the installation of eShel, several bugs have been discovered along the way. Due to a fatal drop in the flux-throughput in 2017, I visited the SONG telescope for service and identified the problem to (possibly) being a wrong mounting of the object-fiber. In continuation to the trip, a few setup optimizations were made. Since the commencement of my thesis, I have likewise logged the functionality of BlueSONG and any changes in regards to e.g. changing of calibration lamps, dismounting and mounting of fibers, etc. A complete list of services together with a future workplan, can be found in Appendix B. The future workplan will likewise be a pivot of discussion in Chapter 6.

¹⁰<https://edu.kde.org/kstars/>



5. Pipeline: Blues



5.1 Overview

With the instrumentation in place it is time look at the spectroscopic software related to the BlueSONG project. Instead of using existing software (such as the eShel module Audela), we choose to develop an project-specific pipeline compatible with the high defocussing of light onto most spectral orders. A Python class called `Blues` works as the main script and library containing all subroutines and utilities used in the spectroscopic analysis. Fig. 5.1 show a schematic drawing of `Blues` and its dependencies. Within this pipeline all subroutines and their utilities are enclosed by dashed lines, the filled blue boxes correspond to the subroutines, and the light boxes are the corresponding utilities. The light boxes on the left side are input arguments, and the light/green boxes on the right side are output arguments. Upon a software call, the black arrows illustrate the interlink between subroutines and utilities and the (downward) computational progress towards a final reduced spectrum and a S index estimate.

To make the code more plain and readable, every subroutine has a built-in graphical illustration (contained in the dependence program `Plot_Tools`) which can be activated by adding the flag `plot=1`. Here every plot utility is build from `matplotlib` packages. Also a utility called `convolve` was developed and used throughout this software to convolve data series (optionally using a mean, median, sum, or std filter). `Blues` likewise takes advantage of highly optimized packages from the `numpy`, `astropy`, and `scipy` library.

The “skeleton” of `Blues` was initially build from SONG’s main échelle pipeline called `SONGwriter` (with identical structural “backbones” for `trace_orders`, `inter_order_mask`, `background`, and `spectral_extraction`), but have extensionally been modified and inspired by other softwares such as `FIESstool` for the FIES spectrograph. Hence, following the line of subroutines seen in Fig. 5.1, the structure is based on standard recipes for stellar spectral extraction. We will in following walk through the functionality of each routine step by step, starting with the subroutine `image_reduction`.

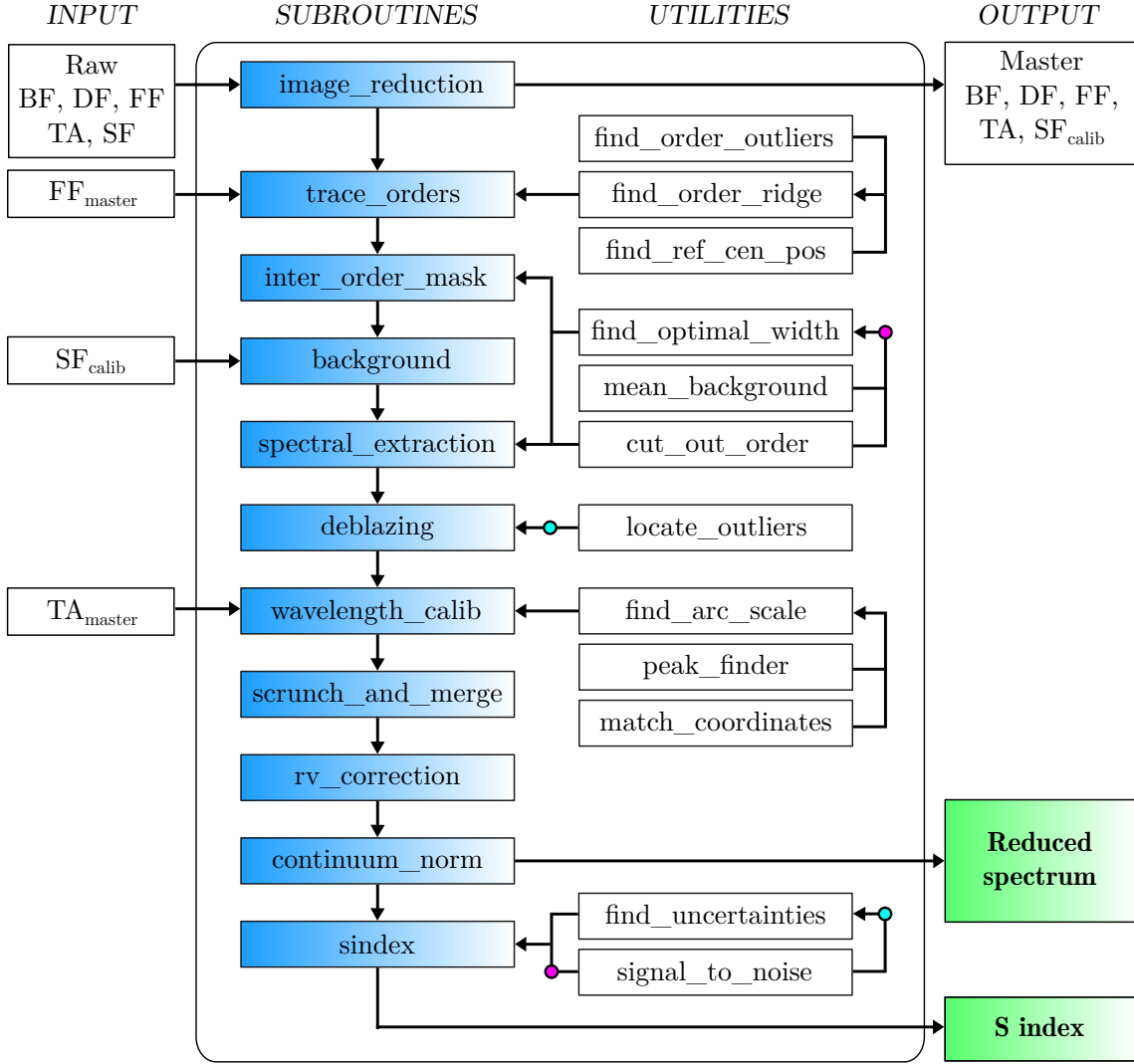


Figure 5.1: Schematic drawing of the data reduction pipeline `Blues`: The combined pipeline of `Blues` is enclosed by the solid line box. The filled blue boxes within are subroutines and utilities are enclosed in normal boxes. The boxes on the left side are input arguments, and the boxes on the right side are output arguments. The two colored dots [(●) and (●)] are internal dependencies between utilities.

5.2 Image reduction

The initial step in all observational astronomy is to reduce the raw data. We choose to develop an image reduction routine for échelle spectroscopy from scratch, which seen from Fig. 5.1 `Blues` automatically takes the raw image files (bias (BF), dark (DF), flat (FF), ThAr (TA), and science (SF) frames) as input. As we will discuss in the following, the image operations is handled using the fits header extension, and returns and saves the corresponding master and calibrated science frames within the parent directory. By following standard image processing the subroutine `image_reduction` reduce the science images by equating

$$SF_{\text{calib}} = SF_{\text{raw}} - BF_{\text{master}} - DF_{\text{master}}. \quad (5.1)$$

First a master bias is created from 50 bias images using a median-filter¹, and this is subtracted from every calibration and science frame. Next 10 dark-current frames, with

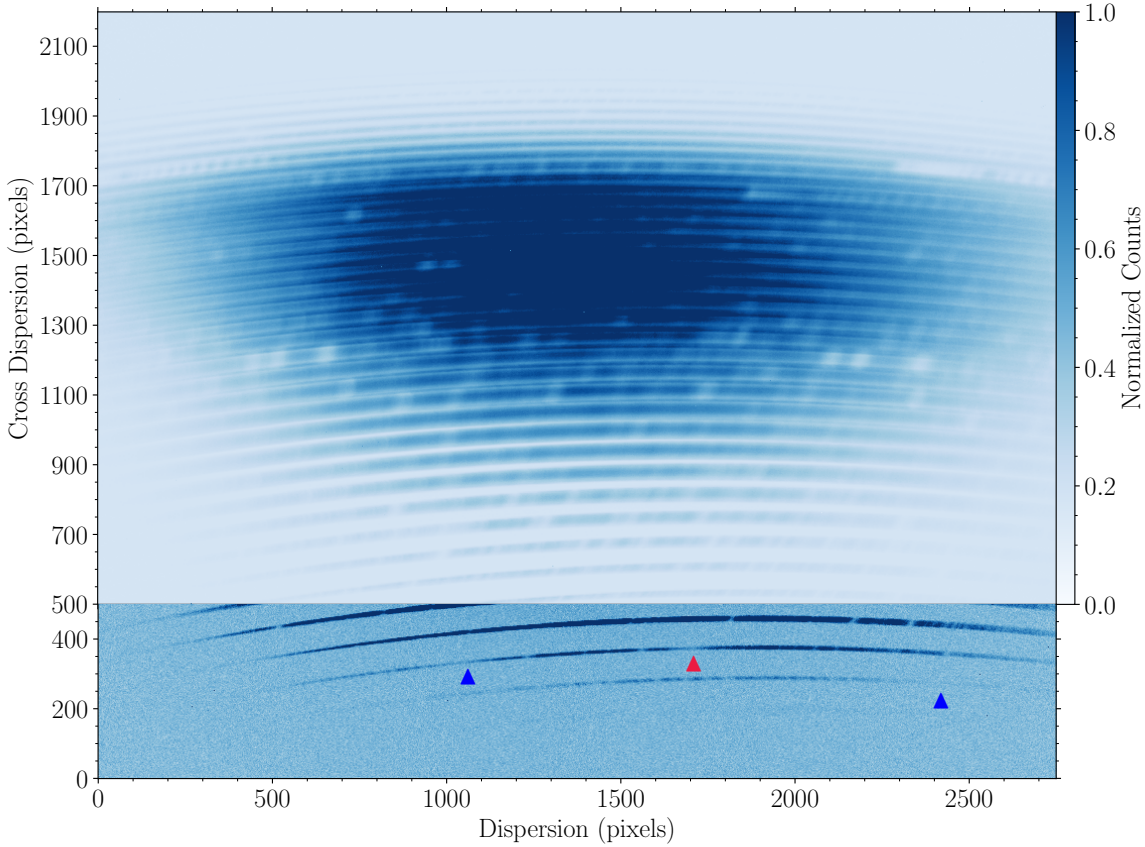


Figure 5.2: Full échelle spectrum of the K1 V star HD 26965. The upper part of the CCD covering optical wavelengths are clearly defocused, while the lower part of the CCD is scaled such the focused order containing the Ca II H & K lines (\blacktriangle) and (\blacktriangleup) are visible, respectively.

exposure times of 1200 s, are median-combined to form a master dark-current image, and then scaled to match the exposure time of the science, flat, and ThAr images, respectively. A master ThAr frame is likewise created using a median-filter on whatever number of frames that is available (either from the daily calibration or extra night arc exposures). For all our targets 3 arcs was used. As a last step the complementary scaled master dark current images are subtracted.

Having calibrated the stellar spectra we will now point our attention to the subroutines of `Blues` which reduce the 2D spectrum to a 1D spectrum. As an illustrative example we use a 1200 s calibrated science frame of the K1 V star HD 26965 seen in Fig. 5.2. Shown is the full-frame échellogram with the lower part of detector being rescaled to accentuate the Ca II H & K lines (\blacktriangle) and (\blacktriangleup), respectively. As the Ca II K line are represented in two orders, due to the free spectral range, a slice of full dispersion width and 450 pixels in the cross dispersion is cut out around these spectral orders.

¹Compared to the mean-method, median-combining is generally more robust against cosmic ray contamination, which in principle only should be a severe problem in space. Since the bias images should be Gaussian distributed in pixel counts, the mean and median should be exactly the same (Howell, 2006). From a selection 50 bias frames the mean and median filter gave (mean: 321, σ : 5.3) and (median: 321, σ : 6.2), respectively. Thus, as the standard deviation of from each image is almost alike and total mean and median of each image agrees perfectly our data is indeed Gaussian distributed.

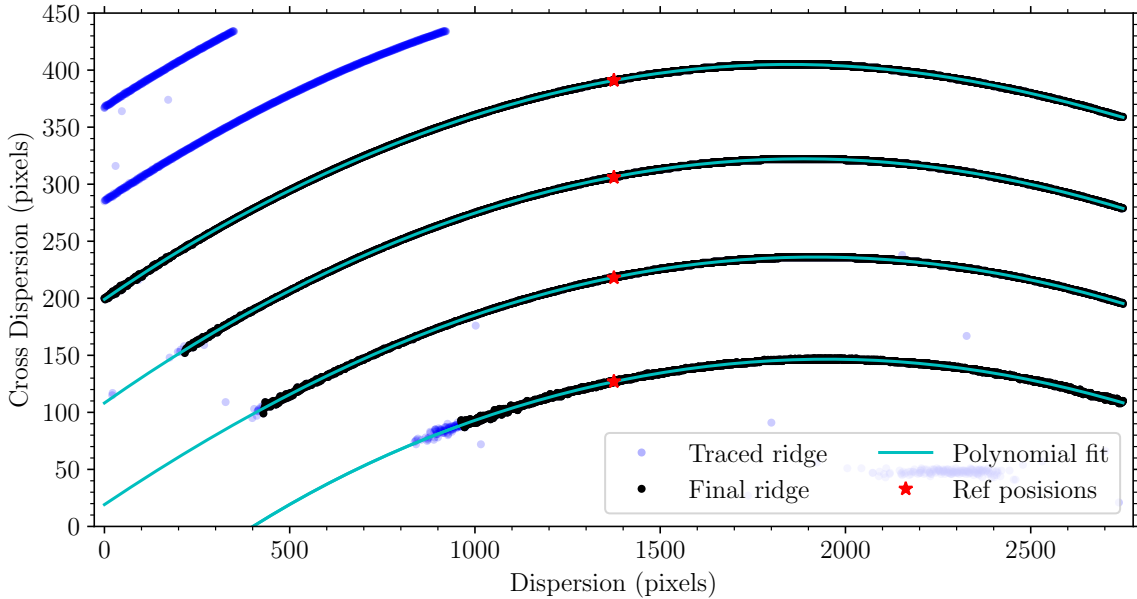


Figure 5.3: Functionality illustration of the subroutine `trace`: The final 5. order polynomial description of the order (—) is a fit to the sigma clipped order ridges (●) which is fully outlined within the image. Also shown is “raw” traced order ridges (●) together with the central reference positions (★).

5.3 Order tracing

The second subroutine within Blues is `trace_orders`. This function maps out the spectral orders in the échellogram by tracing the light distribution along each order in the flat image. To trace each order, first the central order position needs to be known for future references. This is done with a utility `find_ref_cen_pos`, which first use a median-filter to “collapse” the spectrum in the dispersive direction (or simply dispersion), which is done to avoid any problems with contamination of comic rays. Next the data is convolved using a sum-filter which prepares for the detection of the residual peaks. The peak-detection algorithm from `scipy.skimage` finds the local maximum for each order by a simple iterative process of finding the local maximum with an increasing position accuracy. These positions is then returned to the next utility in play, `find_order_ridges`, which traces the light centroid along each order. To describe the light “ridge” of each spectral order, the structure of this utility resembles that of `find_ref_cen_pos`. For each slice in dispersion the spectrum is convolved and within each slice the local maximum values for each order are found. Continuing this procedure looping through slices in dispersion the utility returns up to 10 cross dispersion coordinate peaks per step in dispersion (see (●) in Fig. 5.3).

Lastly the utility `find_order_outliers` constructs a final functional description of each order. Seen in Fig. 5.3 the center position of each order found by `find_ref_cen_pos` is here used as reference points (★) for the order tracing. As a consequence of the initial image cut, some orders are barely defined, and thus removed by through their lack of a order reference position. Since no grating is ideal, so-called *grating ghost*, being weak spurious lines symmetrically placed on each of the parent order line (Gray, 2005), may contaminate the spectrum and therefore result in a degradation of the order definitions. As a guard against this, all 2σ outliers are traced on each side and then removed. Fig. 5.3 shows the original traced ridge (●) and the final ridge without outliers (●). Lastly, a 5. order polynomial serves as the final description of each order (—).

5.4 Background subtraction

Next step in the data reduction is to determine and subtract the background flux level. Within every spectrograph there is a small but non-neglectable amount of scattered light and other sources of uneven CCD illumination that needs to be subtracted to preserve spectralphotometric accuracy and precision. This is likewise an important step in this project because (1) most parts of the detector is out of focus which introduce an increased scattering of light, and (2) it is not well known how this light scattering affect the spectralphotometric quality. Generally the determination of a global background map it likewise important as its description affects the blaze function and hence the final spectrum.

The subroutine at play is the `inter_order_mask` which uses the order polynomials, found from the previous subroutine `trace_orders`, and a program-defined width defining the “inter-orders” (between the orders), to create a background mask. The inter-order mask normalized to the actual pixel counts is shown on top of a transparent flat image in Fig. 5.4. We may notice that scattered light does not affect precision to first order since its level is directly proportional to the total (stellar) flux entering the spectrograph, but a second order effect in our setup may come from a non-systematic light scattering of defocused consecutive échelle orders into the inter-orders. In principle the inter-order width should be a fixed parameter of a spectrograph (as it only depends on the cross dispersion and collimation of the light onto the CCD), but with this second order effect the width of the inter-orders needs to be selected with extra care. We will return to the procedure of finding this “Goldilock” inter-order width, but for now we claim that this value is (and needs to be) determined as part of the routine and the mask in Fig. 5.4 is optimal for this flat exposure. By determine the inter-order width for every observation also makes this software more robust against external changes such as lamp fluctuations and fading. As an extra feature of the `inter_order_mask` it is possible to give a low and high nudge parameter to the mask width, also making the software adaptable to other detectors, where a greater pixel size may result in skewed order tracing.

With the background pixel mask defined a background map of the scattered light within eShel can now be made. While the exposure time of flats can be tuned for the best subtraction, stellar spectra may vary significantly due to stellar magnitude, spectral type, and observing condition. As such this may also complicate the background subtraction from the stellar signal. For fiber-feed spectrograph the best approach is usually to use a surface fitted to the inter-order background over the whole image (Clayton, 1996). Following this approach the subroutine `background` takes the inter-order mask as input and use this to perform a polynomial fit to interpolate local count values both in dispersion and cross dispersion. We start considering the fits in cross dispersion.

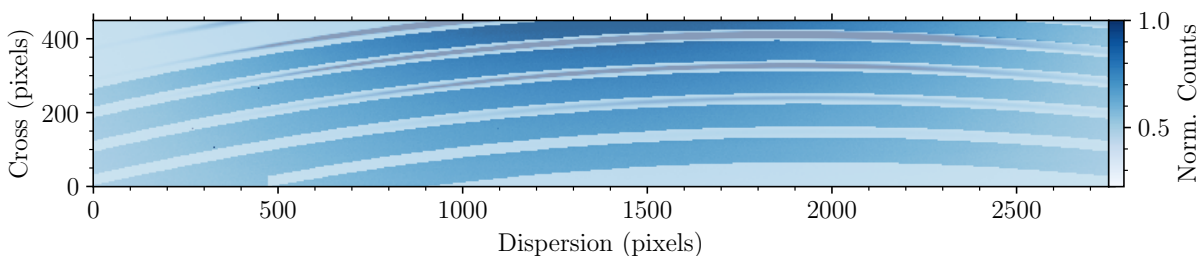


Figure 5.4: Functionality illustration of the subroutine `inter_order_mask`: The inter-order mask is plotted on top (in darkblue) the transparent flat spectrum, making it possible to both see the background mask and the spectral orders beneath.

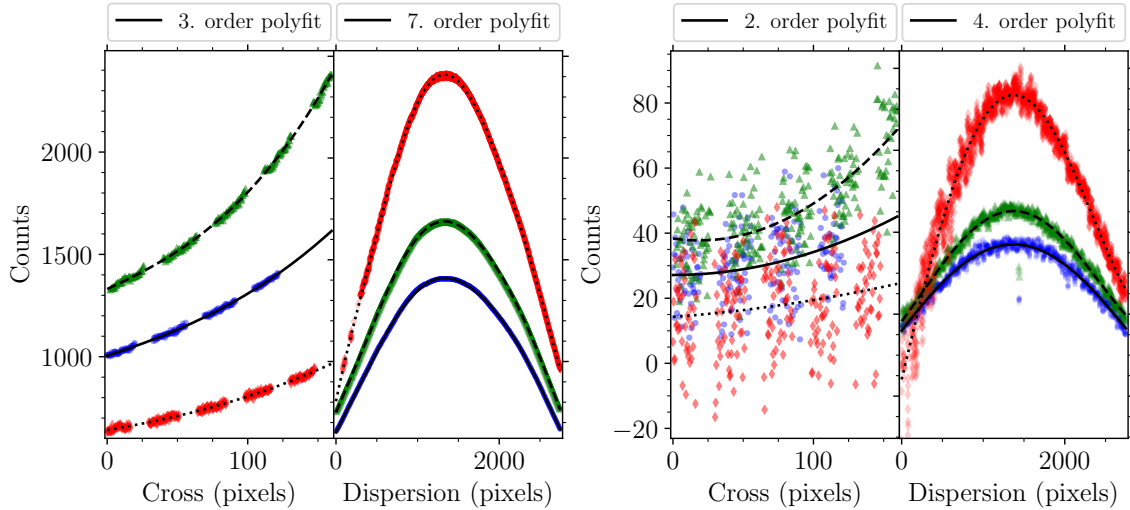


Figure 5.5: Functionality illustration of the subroutine `background` describing the flat-field and stellar background. Left and right panel shows background fitting to the master flat image and the stellar spectrum, respectively. For illustration three slices at different locations of dispersion and cross dispersion ([500, 1000, 2750] and [50, 200, 400] pixel, respectively) are shown [(\bullet), (\blacktriangle), (\lozenge)] together with their complimentary polynomial fits [(—), (---), (\cdots)].

Initially the software cuts out a slice with a length of the total cross order and a width determined by the user defined parameter. The data is then collapsed in dispersion by taking the mean value of each column of dispersion. Then only data within the inter-order mask is kept and used to fit a 2. and 3. order polynomial function for the star and flat, respectively. Additionally, to prevent influence of cosmic rays hits and other blemishes, each fit is performed with a iterable σ -clipping, thus only data less than 3σ is kept for each iteration until the combined data sequence fulfill the σ limit. Fig. 5.5 shows three slices in cross dispersion [(\bullet), (\blacktriangle), (\lozenge)] at different locations of dispersion together with their complimentary polynomial fits [(—), (---), (\cdots)].

Now that we are left with an image array consisting of cross dispersion fit values, this array is then used to fit a 4. and 7. order polynomial fit in dispersion for the star and flat, respectively. Just as was done in cross dispersion a 3σ limit σ -clipping iteration was performed while fitting in dispersion. From the fits to the flat background in cross dispersion small “ripples” are visible which directly originates from small amounts of “spilled” light from consecutive orders into the inter-orders. Hence, instead of trying to fit a high polynomial function in dispersion, to take into account of these fluctuations, a low order polynomial should be a better description of the true background. The ripples are most pronounced for inter-orders at high cross dispersion values, which simply reflects the increasing order defocussing with lower order number m .

5.5 Spectral extraction

Having performed a background subtraction of our flat and science frames it is time to the extraction of the spectral information in the image. There are several approaches to the extraction of the spectral data. The most commonly used are the *optimal* or *linear* extraction also referred to the “normal” or “simple” method, respectively. In the following linear extraction is performed, however, a small overview to optimal extraction developed by Horne (1986) allow insight in the shortcomings of linear extraction.

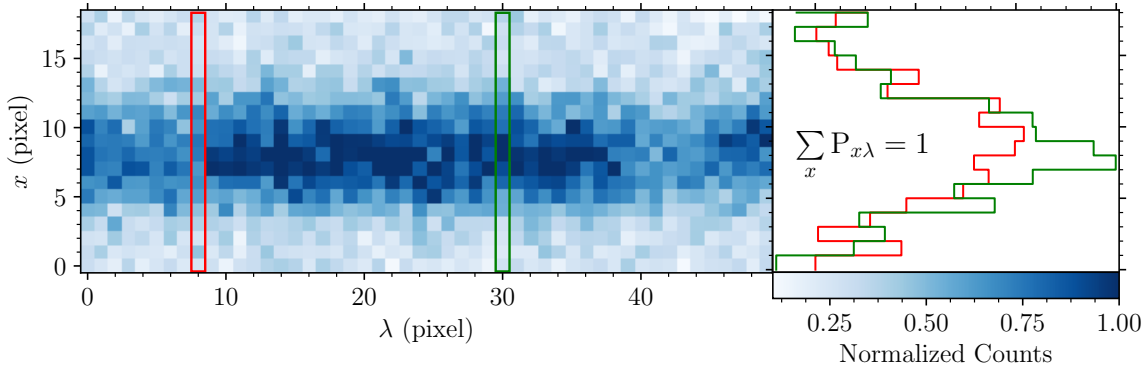


Figure 5.6: Functionality illustration of the subroutine `spectral_extraction` using linear extraction. The left plot is the extracted pixel bandpass around the order of interest with the order clearly seen in dark blue normalized counts. The two boxes represent the spatial profiles in the right plot in accordance with their colors (—) and (—). Compared to linear extraction, where integration sum of the spatial profiles are used for spectral extraction, the optimal profile weight each pixel such lower signal pixels are assigned smaller weights. For completeness of this method, the weights of each spatial profile $P_{x\lambda}$ most sum to unity.

First consider a bandpass of pixel width Δx in the spatial direction and pixel length $\Delta \lambda$ in spectral direction enclosing the object spectrum, with x and λ referring to discrete pixel indices in spatial (cross dispersion) and spectral (dispersion) direction of the CCD, respectively. Connected to the extraction subroutine `spectral_extraction`, this bandpass extraction is done by the utility `cut_out_order` using the traced order as midpoint determination for the “cut”, and a subset of one such bandpass in λ is illustrated in Fig. 5.6. The same figure shows two colored pixel boxes at different spectral positions and their spatial profiles in the right plot by (—) and (—), respectively. In the framework of the above mentioned extraction techniques, linear extraction is simply the integration of all pixels in Δx along λ with equal weighting. Optimal extraction does on the other hand take into account that pixels at the edges of the order profile contain a smaller part of the signal than those in the middle, and consequently nonuniform pixel weights are assigned in order to simultaneously minimize the statistical noise in the extracted spectrum and thus optimize overall spectrum S/N ratio.

It is clear that linear extraction heavily depends on Δx , and thus we now return to the issue of finding the “Goldilock” inter-order width, as this is determined from the “Goldilock” order width ($\Delta x = x_2 - x_1$) used to cut out the order spectrum. Intuitively selecting the object limits x_1 and x_2 to achieve the highest possible S/N ratio, is analog to the problem of selecting the optimal aperture achieving the highest S/N ratio in aperture photometry, hence, we apply this approach. Let $\langle n_s \rangle$ be the variance (or mean square noise) in the signal and $\sqrt{\langle n_s \rangle}$ be the random noise in the signal (or just the standard deviation). The simple devision of the two would recover the S/N ratio for an ideal detector, however, a real detector also gives counts from background sources $\langle n_b \rangle$ (such as the sky background) and from the detector $\langle n_d \rangle$ (Schroeder, 1999)²

$$\text{S/N} = \frac{\langle n_s \rangle}{\sqrt{\langle n_s \rangle + \langle n_b \rangle + \langle n_d \rangle}} \quad (5.2)$$

Inferring (5.2) to a software issue means, first approximating the mean count values with the measured values. Secondly, in accordance to the noise properties of a CCD, by multiplying

²Several approaches to equate the S/N ratio with Poisson statistic exists, e.g. see Bradt (2004).

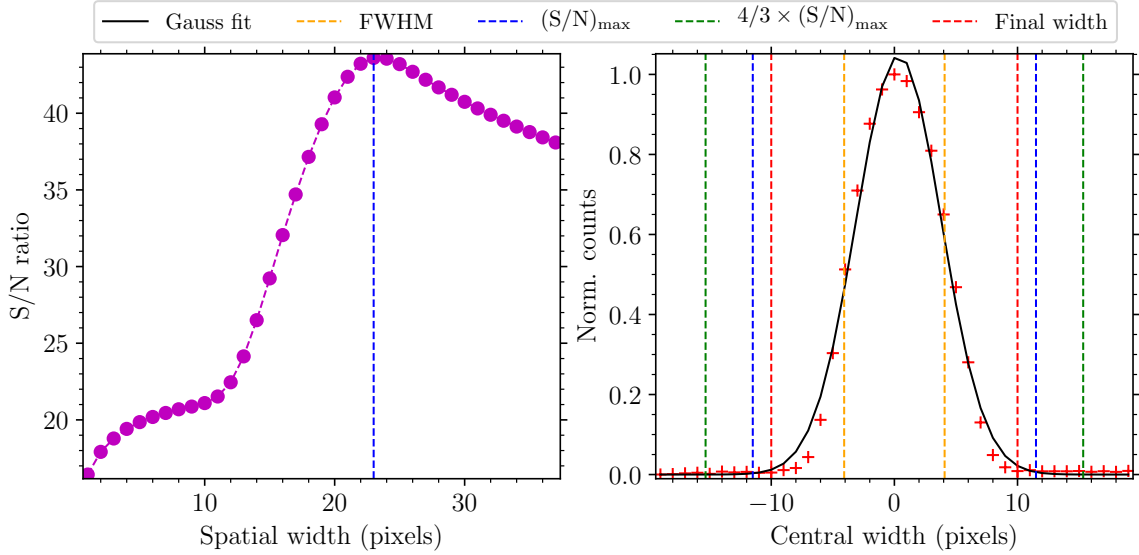


Figure 5.7: Functionality illustration of the utility `find_optimal_width`. Left plot shows the S/N ratio as function of spatial order width (●), with curve maximum (---). The right plot shows a Gauss function (—) fitted to the spatial profile (+), which is used for sanity checking the order width and selecting the inter-order width (---). As well-focused spatial order profiles for eShel is a bit shallower than a real Gaussian profile, the order width (---) is then the width at maximum S/N subtracted by 2 pixels from its limits.

the signal and background counts with the gain, g , and the background and RON, r , with the total number of pixels used for the signal mask, n_{pix} , hence

$$\text{S/N} = \frac{g n_s}{\sqrt{g n_s + g n_b n_{\text{pix}} + r n_{\text{pix}}}} \quad (5.3)$$

Notice, as an image reduction already have been performed, r here represents the mean noise fluctuation of the RON.

Seen in Fig. 5.6 the spectrum is initially cut out using a wide bandpass covering about two spectral cross order profiles. Next the pixel-location of the flat blaze’s peak maximum in the Ca II H & K order is determined. Now looping over increasing spatial widths while calculating the S/N ratio results in a relation (●) seen in the left-hand plot of Fig. 5.7, from which the order width of highest S/N ratio can be found to $(\text{S/N})_{\text{max}} = 23$ pixel (---). Since the flat cross order profile do not have any local S/N maximum, only here the stellar flux is used as the background estimate to create an “artificial” curve maximum – reasoning that this is the high background limit $B \gg S$, the curve maximum represents to first order the tangent point of the curve derivative where the S/N ratio turnover to reach a almost constant level.

For a Gaussian profile, a spatial bandpass of $\Delta x = 3\text{FWHM}$ enclose more than 99% of the flux,³ hence to estimate how this agrees with $(\text{S/N})_{\text{max}}$, from a fitted Gaussian profile (—) to the cross order profile (+), seen from the right-hand plot of Fig. 5.7, we find a $\text{FWHM} \approx 8.2$ pixel (---), thus recovering a ratio of $\Delta x \approx 2.8\text{FWHM}$. From the spatial profile (+) (and from extensive checks of the final spectralphotometric quality) it can be seen that the $(\text{S/N})_{\text{max}}$ width encompass background pixels, hence, a 2 pixel subtraction from this S/N optimized width was implemented as the final order extraction width – e.g.

³More specifically for a Gaussian the $\text{FWHM} = 2\sqrt{2\ln(2)}\sigma$, where σ is the standard deviation (Ivezić et al., 2014).

for this observation 21 pixel is the order extraction width (---). By the Goldilock principle (selecting the inter-order border limits as close to the orders as possible, however, not too close) an order width of $\Delta x = \frac{4}{3} (\text{S/N})_{\text{max}} = 31 \text{ pixel}$ (---) was used to enclose the inter-orders. As extraction is limited by the pixel space, only odd integers can computationally be used as widths, hence, in cases of an even number, the integer is always rounded down. Finally, these widths are then used for the extraction of the flat and stellar spectrum for consistency.

5.6 Wavelength calibration

With a calibrated arc spectrum, as shown in Fig. 4.3 (D), it is time to perform the wavelength calibration. The basic steps here are

1. Identify the lines in the arc spectrum and fit line centers
2. Derive function to map pixel scale to wavelength scale
3. Apply the arc dispersion-wavelength solution to the object spectrum

Two different techniques exist for wavelength-sample relation can be fitted separately for each order or a model for the whole échellogram can be built. The success of the latter technique will depend to some extent on how many lines the software can identify and where they lie in the spectrum – e.g. precision increases steadily if lines near the order edges can be used in addition to central order lines. Since some arc lines are heavily distorted due to high defocussing at their location in the focal plane, each order is treated separately and extracted using `cut_out_order`.

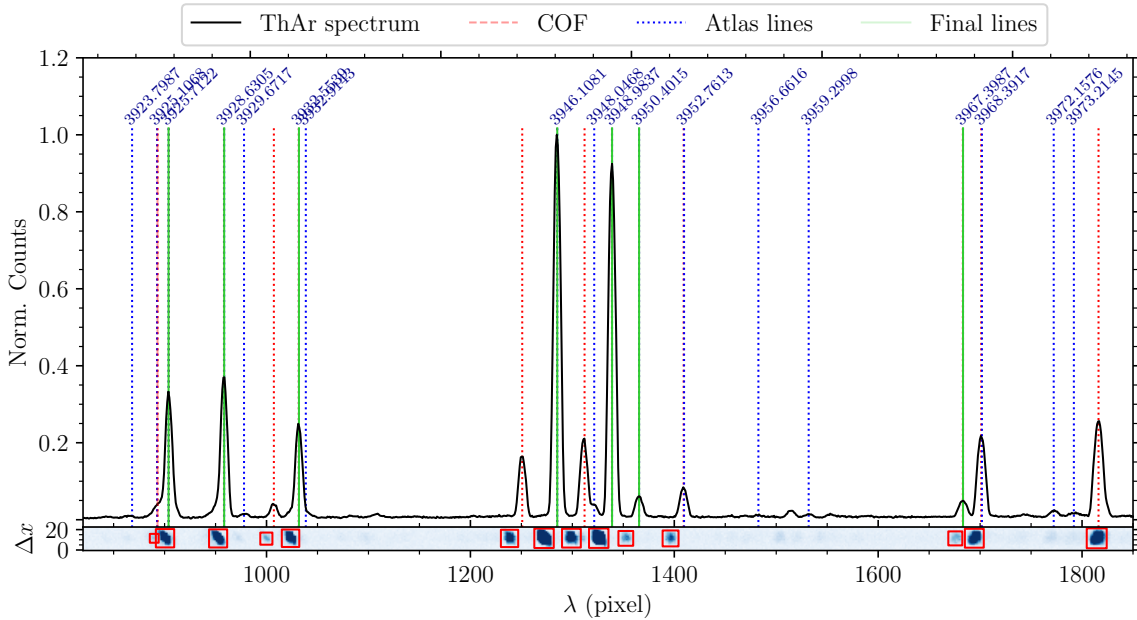


Figure 5.8: Functionality illustration of the subroutine `wavelength_calib`. The bottom panel show a 2D order segment image of ThAr lines from the Ca II H & K order, with red rectangular boxes being all identified arc lines by `peak_finder`. The plot above show the wavelength calibrated arc spectrum (—), together with the observed COF lines (---), Photron atlas lines (···), and the final matched lines (—) used for the wavelength calibration. Note that the mismatch of observed lines between panels is due to the calibration of the upper spectrum.

To identify the ThAr lines within each order the subroutine `peak_finder` is used. This subroutine uses the `scipy.nimage` to find structures in 2D image slice, and tuning the input parameters being the minimum structure pixel number and σ -threshold to eShel, all arc lines are efficiently located. The real strength for using this `scipy` algorithm for the wavelength calibration lies in the fact that it distinguish between comets and patches such as arc lines (or stars). For illustration a order segment of the most well-focused ThAr lines are shown in the lower panel of Fig. 5.8, where each rectangular box is a arc line identified by `peak_finder`. By trial-and-error it was noticed that the tilt-and-oblate distortions of the arc lines effect the determination of Center-Of-Flux (COF) line centers, which in turn heavily degrade the pixel-wavelength solution, if spatial order limits that includes whole line structures were used, contrary to simply apply the order width used for the flat and stellar extraction. Thus, the stellar order width was likewise applied here.

Next, deriving a function to map the pixel-wavelength scale was done over three iterations. In the first iteration a ThAr atlas for the FIES spectrograph,⁴ which use an identical Photron arc lamp, was used to manually identify the common strong well-defined lines, and a 2. order polynomial establish the initial solution. In the second and third iteration all available lines from the FIES atlas and Photron atlas⁵ is used, respectively, and for each a 3. order polynomial is fitted to the dispersion-wavelength scale. To computationally select and reject identical lines between eShel and FIES/Photron, a utility called `match_coordinates` was developed, which uses Pythagorean trigonometric to match coordinates. Hence, the detection threshold for `peak_finder` and `match_coordinates` is complementary increased from first to third iteration, which for both orders of interest leaves an error in the wavelength solution less than 1%. An illustration of the last iteration, the upper panel of Fig. 5.8 shows the final match (—) between all available Photron lines (…), together with all observed lines (….) from the 2. iteration wavelength calibrated arc spectrum (—).

5.7 De-Blazing

As we learned from Sec. 3.1 échellograms provides broad overall wavelength coverage while retaining high spectral resolution. In doing so, it produces a characteristic efficiency trend along each order known as the échelle *blaze function*. Less relevant with eShel, de-blazing is one of the greatest challenges in the reduction procedure for state-of-the-art spectrographs (see e.g. Bowers and Lindler (2003)). The blaze function changes the intensity of the spectrum inside each order and thus modulates strongly the shape of the stellar continuum (Barker, 1984). In each order, the intensity of signal steeply rises from one edge to the center of frame and falls down to the other edge.

There are several methods of the blaze removal. Argued by Barker (1984), one of the most promising is to model its theoretical shape. From the diffraction theory the blaze function should behave like a sinc^2 function of the spectrograph construction parameters (recalling these from Sec. 3.1 being the angle of incidence (α), the blaze angle (θ_B), and grating constant (d)), and by precisely knowing these parameters, a model of blaze may be constructed. However, the real blaze is not produced by an ideal grating, and thus this approximation will inevitable depend on the grating quality and on other construction features to second order, making it a very unfit de-blazing method for an affordable spectrograph like eShel. Another interesting technique is to fit a smooth surface through only the extracted stellar data in pixel-order space, using only the orders where the

⁴Atlas is available at <http://www.not.iac.es/instruments/fies/>.

⁵Atlas is available at http://iraf.noao.edu/specatlas/thar_photron/thar_photron.html.

continuum is present. In this case, the flat field is used only for adjusting the CCD pixels sensitivity. This method, however, is inadequate here as the order of interest is densely packed with the dominant Ca II H & K lines in addition to several sharp absorption features.

For reasons just mentioned we thus turn to one of the simplest and most widely used techniques, namely the division of the extracted stellar spectrum by the blaze of the extracted flat spectrum. Another justification of doing so was noticed by Škoda et al. (2008) as this technique gives best results for fiber-fed spectrographs, where the cross-order profile of the star and flat in theory is the same (as the fiber scrambles the signal), therefore providing identical blaze functions. Again theory is fabricating the truth, as the blaze function in practice shows small variations (known as the Residual Blaze Function) of still unknown origin (Clayton, 1996). However, at the sensitivity level of eShel such variations have not been seen and hence we adapt this method.

Fig. 5.9 shows the flat blaze of the Ca II H & K order (order #57) (—) and the order below (order #58) (—), together with the un-blazed stellar spectra (—). Clearly visible from the stellar spectrum is the contamination of several cosmic ray hits together with CCD non-linearity effects here originating from extra sensitive pixel columns (e.g. at around pixel value 1000 and 2150 since they are both seen in the flat and object spectrum). Since our philosophy is to “reject rather than correct”, at this stage no attempts are made to remove these spurious signals from the object spectrum. On the other hand, all mocked signals needs to removed from the flat blaze before using it for correction. Since the blaze is free of spectral lines, to locate bad spectral data s , a similar description to locate and reject outliers in timeseries analysis is used

$$\text{scatter}(i, N) = \frac{\hat{\mu}_i}{s_i} - 1. \quad (5.4)$$

where $\hat{\mu}_i = \text{median}[s(i-N), \dots, s(i+N)]$ being the i 'th median convolution of $2N$ data points. Intuitively either choosing a low or high N value will simply show different levels of intrinsic scatter, hence, if any data point calculated by (5.4) is extreme (higher than a

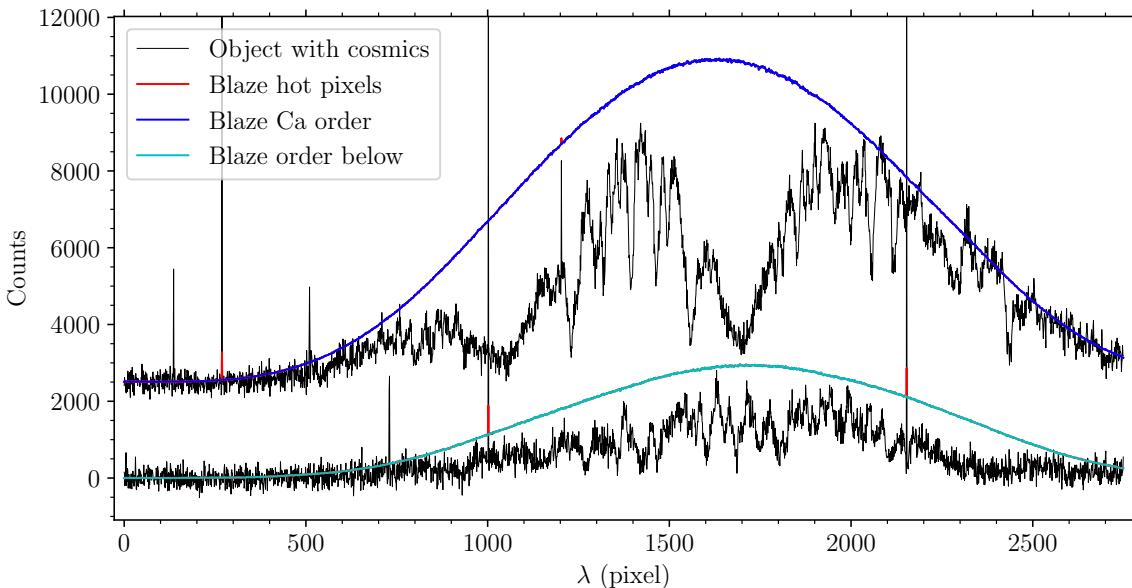


Figure 5.9: Functionality illustration of the subroutine `blaze_function_removal`. The blaze function (—) is used to correct the uncorrected spectrum (—). The blaze corrected data can be seen in top plot of figure 5.9.

chosen threshold), this will be located and replace them by $\hat{\mu}_i$ (in contrast to delete it). Fig. 5.9 shows the order blazes before (—) and after (—) the data correction. Having wavelength calibrated and de-blazed each order, the time has come to scrunch and merge orders.

5.8 Scrunching & Merging orders

Mentioned in Sec. 3.1, it is evident from Fig. 5.9 that the free spectral range for each order especially allows optimized spectral extraction when working in near-UV wavelength, first because the strong wavelength dependence of the blaze shape (which extent is much shallower in blue than in red) and, secondly, because of the low S/N regime for ground-based near-UV observations. In fact, since the the quasi-continuum V bandpass, used to calculate the S index, in the Ca II H & K order lies almost at the blaze edge minimum, and because the same band is represented in blaze maximum of the free spectral range below, it is possible to retain a high spectrophotometric quality by *scrunching* and *merging* the spectral orders.

In spectroscopy, scrunching is the process of re-binning spectra to a fixed wavelength (or even velocity) scale, in order to combine (or merge) successive orders, or co-add spectra from separate exposures (Clayton, 1996). Thus, scrunching the data is equivalent to apply a filter to the data by simple interpolation. In this project interpolation is done using `scipy.interpolate.griddata` which allows to perform interpolation using an optimal weighting scheme for the input data. Notice since the dispersion in individual orders is different, scrunching to a new wavelength grid may decrease the actual spectral resolution, which ultimately means the flux counts per wavelength bin is not conserved Telting et al. (2014). As only two successive orders are combined, these effect may altogether be ignored. Combining orders into a single spectrum is generally done with a weighting strategy in the regions where the wavelength coverage of orders overlaps, i.e. determine the wavelength cross section where one order is much fainter than the other. Since here only the extent and location of the V bandpass in the lower spectral order is of interest, the final spectrum is thus simply merged using 3915 Å as the reference, and a lower cut is applied at 3880 Å. Hence, the merge spectrum covers wavelengths from 3880–3920 Å.

5.9 Radial velocity correction

Since astronomical objects are moving in respect to each other, any movement v in respect to an “stationary” observer will introduce an wavelength shift $\Delta\lambda$ of the emitted wavelength λ measured in the observers rest frame. This phenomena is also known as the (non-relativistic) Doppler effect

$$\frac{\Delta\lambda}{\lambda} = \frac{v}{c} \quad (5.5)$$

where c is the speed of light. In astronomy the Radial Velocity (RV) amplitude thus consist of various velocity contributions, such the movements from Earth’s rotation and orbital motion, the Barycenter (the Solar system’s Center Of Mass (COM)), the motion of the target object itself, the cosmological redshift (included if the object is sufficiently far away), etc. For stars in the solar vicinity the three former contributions are usually sufficient in most astrophysical analyses, with the occasionally exception of e.g. exoplanet detections.

In spectroscopy usually the RV shift is determined by cross-correlating a high resolution spectrum of a standard star, or in solar activity analysis, with a solar spectrum. As only

Table 5.1: RV corrections of the stellar sample.

HD	Date	Stellar RV km s ⁻¹	Barycentric km s ⁻¹
26965	2019-02-17	-42.18(13)	-26.652(3)
136202	2019-04-15	+54.3(1)	+10.986(3)
142373	2019-04-15	-56.88(9)	+3.660(3)
152391	2019-04-15	+45.09(7)	+20.627(3)
185395	2017-10-03	-27.26(15)	-8.359(3)

a very limited spectral range is at our disposal, another strategy, using the stellar RV amplitude and Barycentric motion, was used to shift the stellar spectra. The wavelength plate scale for the final spectra is $0.0528\text{\AA}\text{ pixel}^{-1}$ which, by using (5.5) with $\lambda = 4000\text{\AA}$, translate to of a scaling of $\Delta\lambda(1\text{km s}^{-1}) \approx 0.0133\text{\AA}$ (or $v(1\text{\AA}) \approx 80\text{km s}^{-1}$). Assuming a stellar RV amplitude of 100m s^{-1} gives a difference between the relativistic and non-relativistic doppler velocity of about 10^{-5}\AA , which is two orders of magnitude from what can be resolve in this project. Hence, the non-relativistic doppler shift was used only.

In practice the stellar RV amplitude is collected from the CDS database⁶ (which for most stars uses the latest proper motion release from the Gaia missions). Next the `radial_velocity_correction` from `astropy.coordinates` library is used to calculate the Barycentric correction, which also includes effects such as the rotational and orbital motion of Earth, as well as the gravitational redshift due to the potential at the Earth's surface. From the date and time of observation, and the observatory's location, the software uses the so-called *ephemeris*⁷ for computing the location of the Sun and Earth, and hence the residual radial velocity component in respect to the target object.⁸ Less important to this project, any observed radial velocity provides a Barycentric correction that is accurate to a level of approximately 3m s^{-1} , hence, the CDS value of the stellar RV is the actual limitation. Tab. 5.1 shows the applicable velocities used to make the final correction for each target star. As a quick sanity check, notice that Earth's orbital speed around the Sun on average is about 30km s^{-1} , for which the Barycentric velocities are in the same bold park. Also all targets was checked for binarity, which for our stellar sample is firmly known since these are nearby and bright stars.

Lastly, as part of the wavelength calibration the pipeline also trace any instrumental drift in dispersion (and cross dispersion), which happens mainly due to temperature variations in the immediate enviroment of the spectrograph. Since daily ThAr calibration frames are available almost from the time of eShel's installation, day-to-day position changes of the ThAr lines was monitored, which for approximately the past year are plotted in Fig. 5.10. Here the drift are both shown in pixel space and in velocity space, and the errorbars represent the scatter of the drift of the used arc lines. Only very high S/N and low defocused arc lines was used for drift monitoring (and 15 lines for this plot). Comparing to another study by Engel et al. (2017), which placed their eShel spectrograph inside a thermally insulated box, a day-to-day variation of about $\pm 1\text{km s}^{-1}$ was found, which is more or less in correspondence to our setups seasonal change. The temperature stable

⁶<http://cds.u-strasbg.fr/>

⁷In astronomy and celestial navigation, an ephemeris gives the trajectory of naturally occurring astronomical objects as well as artificial satellites in the sky, i.e., the position (and possibly velocity) over time.

⁸See Wright and Eastman (2014) for the computational implementation, and for more information see <http://docs.astropy.org/en/stable/coordinates/velocities.html>.

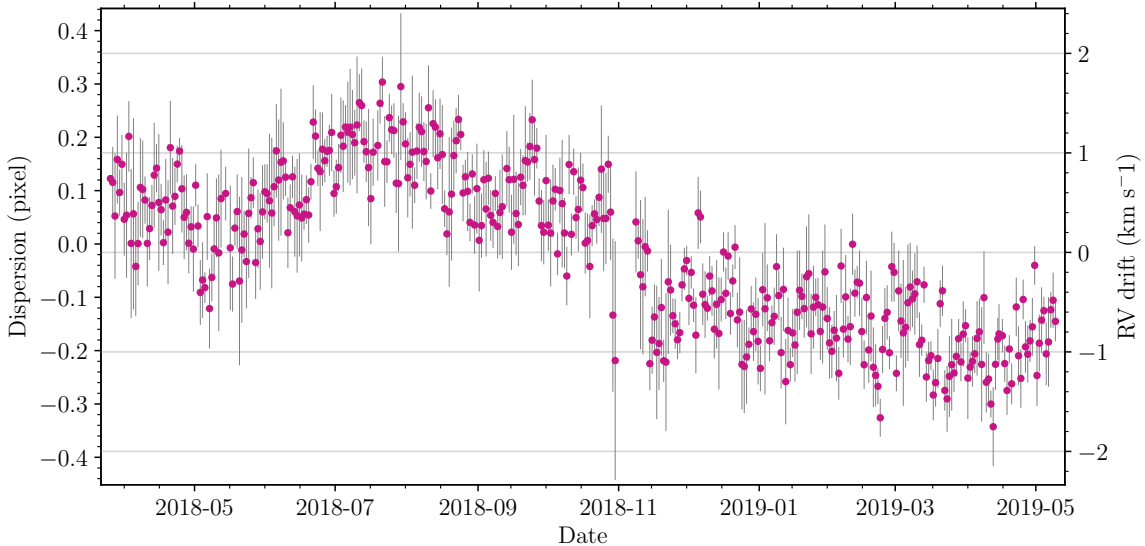


Figure 5.10: Annual drifts of the ThAr line positions on the CCD shown in pixel-space (left) and RV drifts (right).

container for which this project’s eShel spectrograph is placed in, give rise to systematic day-to-day RV variations of about $\pm 0.5 \text{ km s}^{-1}$, compared to Engel et al. (2017)’s result, likely reflects that a larger volume of the temperature insulator results in higher stability. Most importantly is that, the sub-pixel drifts in dispersion are too small to effect our S index calculations.

5.10 Continuum normalization

So far the most pronounced variations in the extracted continuum has been removed by the division of the normalized blaze function, though the blaze correction do not recover the physical continuum. Generally continuum normalization are performed either by locating the position of the physical continuum, using a synthetic spectrum, or simply normalizing by trial-and-error (Gray, 2005). The choice upon these techniques depends heavily on the spectrum at hand: the continuum may not be present or locatable e.g. due to spectral quality, limited spectral range, and/or severe blend of lines or molecular bands. The two latter instances is in fact the encountered limitations for this project, since the Ca II H & K order is first dominated by the Ca II H & K lines itself and, secondly, the whole order is generally basked in strong metal lines (mainly by Fe) and molecular bands (especially TiO increasingly contributing for cooler stars in our sample). As a workaround we recognized that the trial-and-error continuum normalization procedure at Lowell Observatory (Hall et al., 2007) yield surprisingly accurate results consistently. For the Ca II H & K order they use two pseudo-continuum points at 3912 Å and 4000 Å, fit a straight line to the two points, and simply divide the order by the linear fit. As this procedure for the Solar-Stellar Spectrograph (SSS) pipeline is done before the RV correction, to avoid the exact position of the pseudo-continuum points to be coincidental, a search interval of $\pm 100 \text{ km s}^{-1}$ from each predetermined fit point is scanned to find the maximum spectrum value near each point. Since a RV correction already have been applied here, we adapt Hall et al. (2007) methods and additionally test two extra methods to determine the linear fit: (1) using the exact pseudo-continuum points, and (2) using the mean value of a $\pm 1 \text{ Å}$ spectral interval around each point. As the choice of continuum clearly effect the estimate of S indices, we will wait for the next chapter to discuss this issue.



6. Results & Discussion

With an introduction to stellar magnetic activity, instrumentation, observation, and software development in spectroscopy, in this chapter we present the main result of this work with eShel. This includes a discussion of our activity results, on the shortcomings of the software development, and the performance of the eShel spectrograph.

6.1 The eShel S index

Like so many other studies in the field of stellar activity, the eShel S index is calculated following the original procedure used at the MWO (Duncan et al., 1991). From the HK Project we may recall that the dimensionless S index is defined by

$$S = \alpha \frac{H+K}{R+V} \quad (6.1)$$

with α being a calibration constant, H and K are the recorded counts in a 1.09 Å FWHM triangular bandpasses, centered on the Ca II H and K lines at 3968.470 Å and 3934.664 Å, respectively, and V and R are two 20 Å wide pseudo-continuum reference bandpasses centered on 3901.0 Å and 4001.0 Å, respectively. For illustration the position, physical extent, and enclosed flux of each bandpass, using the reduced stellar spectrum of HD 26965, is shown in Fig. 6.1.

Observations at the MWO were originally made with the 2.5 m telescope, using a so-called coudé scanner with a two-channel photometer, but in 1977 it moved to the 1.5 m telescope to continue the monitoring observations more frequently. Retaining equivalence internally in the survey, the HKP-2 spectrophotometer was used. This was a grating spectrometer which was designed with a rotating mask with four slots spinning at a sufficient rate to sequentially observe all four channels independently within the timescale of unchanged atmospheric conditions. In 1983 a copper wheel was installed to sample the H and K fluxes simultaneously for increased throughput, and thus the H and K channels are exposed 8 times longer than the continuum bandpasses (Vaughan et al., 1978). For any other

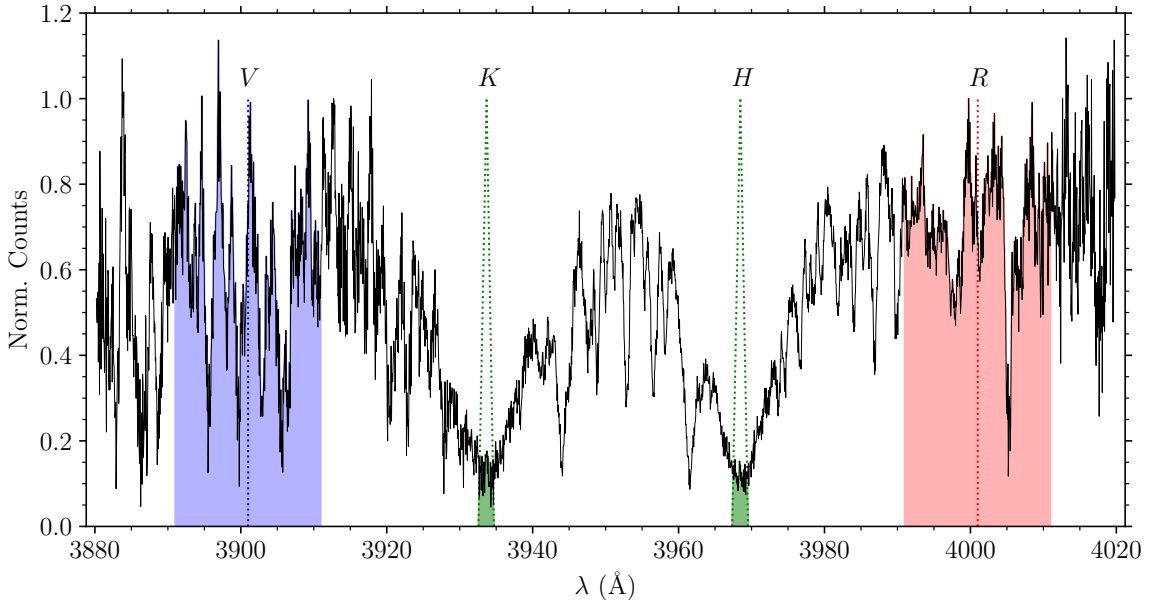


Figure 6.1: Illustrative example of the position and physical extent of each bandpass that is used to calculate the S index. The name of each bandpass (V , K , H , and R from left to right) is indicated above the continuum level normalized to one, and the stellar spectrum shown is of the K1 V dwarf star HD 26965.

spectrograph operating by default (like eShel), to be on the MWO scale (6.1) needs to be multiplied by a factor of 8.

Before heedlessly jumping to the calculation of S , it is worth acknowledging the statement by Hall et al. (2007) that a direct comparison to HK Project can be accomplished following two paths

- (1) Replicating the triangular MWO H and K bandpasses as close as possible.
- (2) Choose a bandpass in accordance with the spectral resolution at hand, and simply letting α be the best linear-fit coefficient to the MWO data.

From the literature we identified two different bandpass selection techniques for procedure (1) and various bandpass selection and flux estimation techniques (countable if chosen upon physical reasoning) for procedure (2). Although not explored fully in detail in this project, for selecting bandpass/estimating bandpass fluxes, three different techniques using method (1) and two different technique using method (2) were explored and implemented computationally as part of the `sindex` subroutine.

Each method may be understood by considering Fig. 6.2, which shows an enhanced view on the K (top) and H (bottom) bandpass from Fig. 6.1, likewise with the triangular MWO bandpass highlighted (\cdots). True for both methods above, the real issue is resolution, since this set the finite number of wavelength grid-points for each bandpass, and therefore how precise the flux may be determined. Deciding upon method (1) this directly translate into a geometric problem as a consequence of triangular shaped bandpasses. Illustrated for eShel's resolution, Fig. 6.1 shows that due to the finite resolution, the triangular MWO bandpass (—) cannot be defined exactly at the points where it coincide (\bullet) with the stellar spectrum (—). Consequently this means that the lower the spectroscopic resolution, the higher the flux uncertainty using method (1). As mentioned above, since this is a geometric problem, we can translate the issue of finding integrated fluxes to determine the area inside

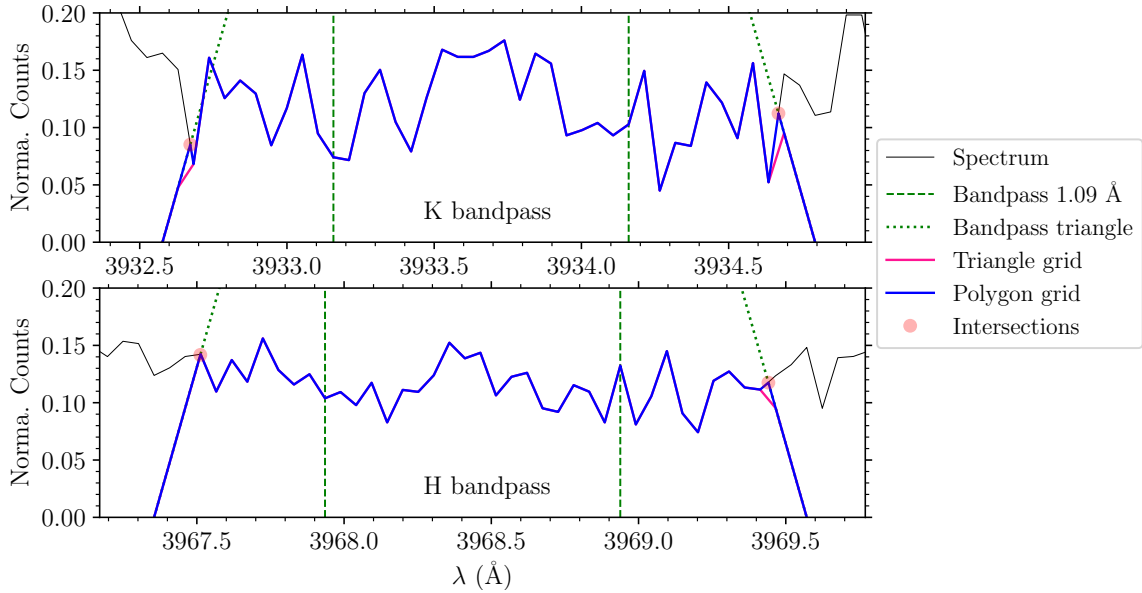


Figure 6.2: Illustration of different H and K bandpasses, over-plotted on the stellar spectrum of the K1 V dwarf star HD 26965 (—), which clearly shows chromospheric line emission. The different bandpasses considered are the MWO triangular bandpass (···) and a 1.09 Å square bandpass (---). Working in a finite grid, means the flux in the triangular bandpass either can be determined by simple flux integration (—) or using the area enclosed by a polygon (—).

each closed curve defining the bandpass (i.e. the colored boxes of Fig. 6.1). According to Green's theorem the area an object D bounded by a closed curve C can be expressed as a contour-path integral around this curve

$$A = \iint_D dA = \frac{1}{2} \oint_C (-y \, dx + x \, dy) \quad (6.2)$$

Since we computationally work in a finite grid in wavelength-intensity space, this curve integral can be approximated by a closed plane bounded by straight sides, also called a *polygon*. For polygons the total enclosed area is calculated by

$$A = \sum_{i=1}^{N-1} L_{i+1,i} + L_{1,N} \quad \text{with e.g.} \quad (6.3)$$

$$L_{2,1} = \int_{x_1}^{x_2} y \, dx = \frac{1}{2}(y_2 + y_1)(x_2 - x_1) \quad (6.4)$$

and acknowledging that $x = \lambda$ and $y = s$, with s denoting the normalized spectral counts. Setting aside the exact value of the S index, from all five targets, we here report a difference in S between the Polygon (—) and MWO bandpass (—) of $\Delta S \approx 0.12\text{--}0.65\%$.

Mentioned above, using method (2) actually implies any other technique for which a direct comparison to the MWO data are not possible, and thus calibrating to the MW scale are needed. E.g. two techniques used occasionally in the literature are either working with simple integrated fluxes in any reasonable choice of bandpass, or with integrated fluxes, normalized by the triangular bandpass definition. Intuitively the latter technique corresponds to a simple weighting procedure given highest weight to the Ca II H & K line

cores – which might be handy in low S/N cases, but on the expense of a higher dependency to the error of the wavelength calibration.

As a last technique, which may efficiently be used by either method (1) or (2), is working with mean fluxes per wavelength interval, which was introduced by Lovis et al. (2011) analysis using data from the HARPS spectrograph at the ESO La Silla 3.6 m telescope. Working with mean fluxes per wavelength interval infer that $\tilde{X} = X/\Delta\lambda$, where X represent any bandpass and $\Delta\lambda_X$ the effective bandpass width, which translates S into

$$S = \alpha \cdot 8 \cdot \frac{\Delta\lambda_{HK}}{\Delta\lambda_{RV}} \cdot \frac{\tilde{H} + \tilde{K}}{\tilde{R} + \tilde{V}} \quad (6.5)$$

It may be noticed that with $\alpha = 2.4$, being the factor used to calibrate the HKP-2 data to the HKP-1 data, the front-factor in (6.5) equals nearly unity: $2.4 \cdot 8 \cdot 1.09 \text{ \AA}/20.0 \text{ \AA} \simeq 1.046$ (or even 1.0028 if $\alpha = 2.3$ like Lovis et al. (2011) uses). The advantage of mean fluxes, compared to any other bandpass flux measurement, comes from its minimization of potential edge effects at the bandpass boundaries (as discussed above), plus uncertainties related to the wavelength calibration. Actually Lovis et al. (2011) used mean fluxes in accordance with method (1) to make a direct comparison to the MWO data, for which an excellent agreement between the HARPS and MWO S indices was obtained (and needed only a small scale calibration). Investigating the real influence between all these different methods, techniques, and various combinations of the two, are beyond this project. However, it is worth noticing that with eShel, comparing our seeming direct estimates of S indices (from method 1) with the $\langle S \rangle$ of the non-active MWO standard stars in our sample (hence HD 136202 and HD 142373), we only get a $\sim 5\%$ lower estimate using mean fluxes per wavelength interval, compared to $\sim 20\%$ lower estimate using either integrated fluxes or polygon fluxes.

For the reduced spectra of eShel and FIES, by choice we continue with method (2) using the simple 1.09 Å square bandpass seen in Fig. 6.2 since, first, visually for both datasets this bandpass seems to be sufficiently wide to contain the total excess of chromospheric emission. Secondly, we did not find an agreement between the different techniques within methods (1), and there is no need to introduce any extra uncertainties that this may involve. Thirdly, argued by Lovis et al. (2011), even with the best of effort trying to arrive on the MWO scale, all spectrographs shows different levels of scattered light, thus introducing systematics, and hence a final fit-correction is needed anyway.

6.1.1 Calibrating to the Mt Wilson scale

For reasons explained above, the integrated fluxes of the 1.09 Å square H and K bandpass were used for calculating S , meaning α needs to be determined through a simple linear calibration between our eShel/FIES data and the MWO data.¹ The normalization constant α are usually obtained by measuring a number of stars that were part of the HK Project (Duncan et al., 1991), however, since only two standards were observed with eShel and FIES, we need to included all observations because, first two data points do not provide a fit uncertainty and, secondly, spanning a larger range in S indices gives more reliable results. To include the cyclic activity stars of our sample, HD 26965 and HD 152391, a uncertainty-weighted sinusoidal fit to the available MWO data was performed to find a comparable value of S_{MW} . We have likewise included our initial observation of HD 185395

¹Although, it have been argued that the calibration does necessary follow a linear function Isaacson and Fischer (2010).

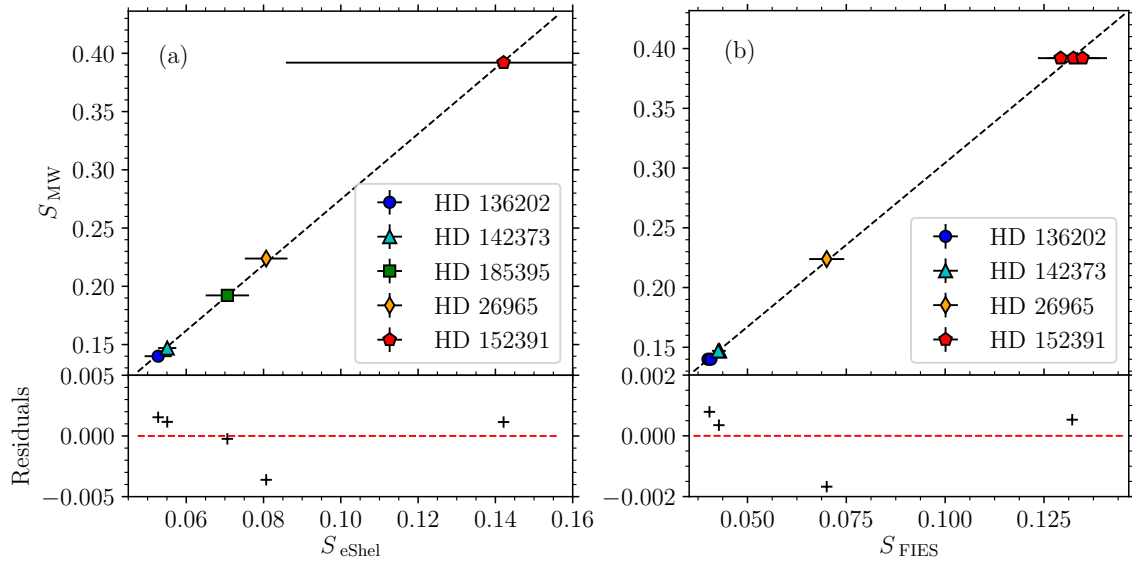


Figure 6.3: Determination of the α coefficients from a best linear-fit between S indices for (a) eShel and MWO, and (b) FIES and MWO. The fits are performed with only a single eShel observation for each target, while for FIES, none for HD 185395, one for HD 26965, two for HD 136202 and HD 142373, and three for HD 152391 were available for the calibration. Notice that both HD 26965 and HD 152391 are magnetic active stars, showing a clear cyclic activity period, and therefore S_{MW} have been determined from a sinusoidal fit to the available MWO data.

(θ Cyg). For this star only a limited amount of MWO data exists, and we thus assumed a flat activity – also from the fact that this star is a F3 V type, and belongs to the spectral range of similar standard stars, for which we do not see a activity cycle.

The best linear-fit between S_{MW} and S_{eShel} (the eShel S indices), and between S_{MW} and S_{FIES} (the FIES S indices), are shown in Fig. 6.3 (a) and (b), each with their residuals plotted in the panel below, respectively. Mentioned in Sec. 4.2 with eShel only a single observations were acquired for each target, while observations made with FIES, none for HD 185395, one for HD 26965, two for HD 136202 and HD 142373, and three for HD 152391 were acquired. Consequently, for higher precision a mean S value was used for FIES whenever possible. Both polynomial fits are made with the mathematical χ^2 minimization technique, and the linear fits yield

$$S_{\text{MW}} = 2.815 S_{\text{eShel}} - 0.007 \quad (6.6)$$

$$S_{\text{MW}} = 2.744 S_{\text{FIES}} + 0.030 \quad (6.7)$$

with the fit uncertainties from the residuals being $\sigma = 0.002$ and $\sigma = 0.001$ for eShel and FIES, respectively. These uncertainties were included in the final uncertainty estimate of our results.

6.1.2 Uncertainties

So far we have only briefly mentioned the uncertainties in relation to the χ^2 minimization of the fitting procedure and in connection to the S/N ratio used to estimate the spatial order width for spectral extraction. As a shared problem with continuum normalization in this project, the absence of the physical continuum in the area around the Ca II H & K lines, makes it impossible to follow any standard procedure involving a continuum domain

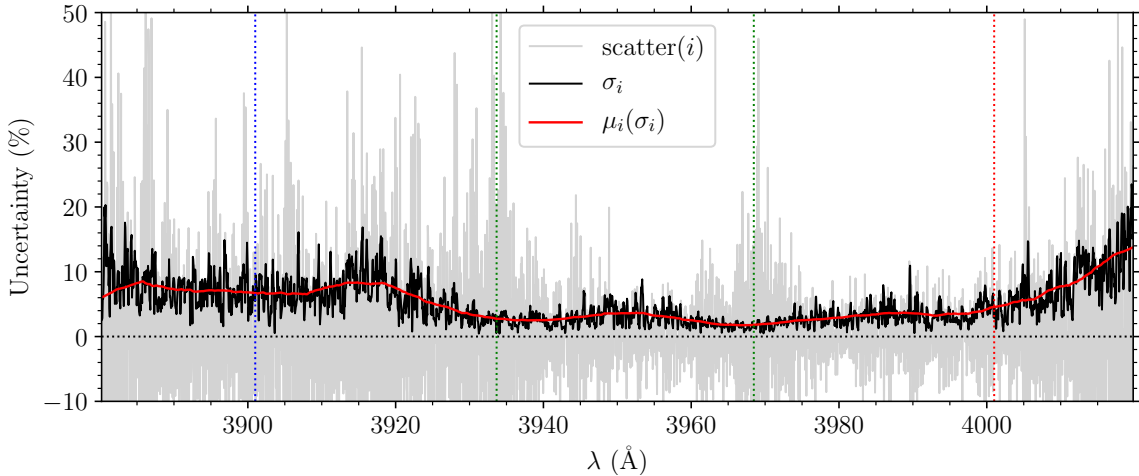


Figure 6.4: Illustration of the S index uncertainty estimation. Just for illustration the scatter function (—) is plotted, together with spectrum convolved first by a σ_i filter (—), for then to be smoothed by a μ_i filter (—). Central positions for each bandpass are indicated by the colored dotted lines. Notice that the small bump around $\lambda = 3920\text{ \AA}$ is the merging-point between the orders, and hence represent the fact that merging was not done in a S/N optimization scheme.

free of lines to either measure the order S/N ratio or estimate the flux uncertainties in each bandpass. Nevertheless, mean flux uncertainties in each S index bandpass is in the following estimated using the *fractional uncertainty* given by $(\text{S}/\text{N})^{-1}$.

A statistical estimate of the S/N ratio can be derived from the final reduced spectrum at a given position. This is done by comparing the flux level (signal) within a particular wavelength range with respect to the intrinsic noise of the spectrum in the same wavelength region, i.e. the ratio between the average signal value to the standard deviation of the signal $\text{S}/\text{N} = \mu/\sigma$. Such a S/N estimate will not only consider the random variations in the detection, but all the additional sources of error introduced by the pipeline reduction process (Clayton, 1996), hence, this method was used. From a computational point of view, μ and σ are calculated using

$$\mu_i = \frac{1}{N+1} \sum_{j=i-N/2}^{i+N/2} s(j) \quad (6.8)$$

$$\sigma_i^2 = \frac{1}{N+1} \sum_{j=i-N/2}^{i+N/2} [s(j) - \mu_i]^2 \quad (6.9)$$

with N effectively being the (even) number of points used in the so-called *box car* filter. Thus, as seen before this is a simple data convolution. Generally (6.8) and (6.9) are in fact applicable to any data sequence as they only depends on N , which in turns depends on the data sampling and how fast the quality is changing throughout the data sequence. Seen in Fig. 6.4 for the example of HD 26965, for illustrative reasons and to get an initial idea of how internal noise depends on the intensity, first we compute the scatter function (—) following the description of (5.4) presented in Sec. 5.7, however, replacing the median filter with a mean filter. As a check of our expectation, seen by the increased scatter in the Ca II H & K lines the mean-scatter do not provide a good description for the uncertainty. For our sampling and data quality (6.9) is first calculated using a convolution filter of $N = 2$ (—), and to equate the fractional uncertainty function along the spectrum $\sigma_s = \sigma_i/\mu_i$ the

Table 6.1: Fractional uncertainties for the stellar sample. Notice the uncertainties from the blaze normalization and wavelength solution are a direct result of exposure time of the flat and arc image used, respectively. For FIES only uncertainties estimated from the spectrum have been considered.

HD	Blaze σ_b (%)	Wavelength σ_λ (%)	Spectrum $\sum_i \sigma_s(X_i)$ (%)	S/N $\sum_i \sigma_s(X_i)$ (%)	Total (%)	FIES (%)
26965	0.84	0.31	16.4	15.3	17.55	6.34
136202	1.30	0.34	16.4	14.8	18.04	3.54
142373	1.30	0.34	13.0	11.0	14.64	3.66
152391	1.30	0.34	49.0	43.2	50.64	4.69
185395	1.80	0.34	17.5	14.1	19.64	—

data was convolved using a $N = 100$ mean filter (—). Lastly, from σ_s the mean uncertainty for each bandpass X_i was then determined using the exact width of each bandpass.

As a sanity check of the bandpass uncertainties, $(\text{S}/\text{N})^{-1}$ may in fact be estimated in an alternative way, trying to simulate a stellar order continuum. This was done by first scaling the count level of each order blaze (i.e. using the flats) to that of the stellar spectral orders before the blaze normalization – exactly as shown in Fig. 5.9. More specifically, the blazes was scaled as close as possible to the pseudo-continuum peaks discussed in Sec. 5.10. Next the S/N ratio along each blaze-continuum was calculated using (5.3) and for each bandpass the mean result was returned. Tab. 6.1 shows all the considered fractional uncertainties for the stellar sample, together with the total fractional uncertainty from the detector, wavelength calibration, α calibration coefficient, and spectral quality. We notice that the flux uncertainties using the pseudo-continuum method to determine the S/N ratios, approximately agrees with the measured spectral quality, and thereby confirm their usage.² The values of σ_λ and σ_α is determined from the χ^2 goodness of fit, hence, the uncertainty of S is then calculated through simple error propagation using the value presented in Tab. 6.1. For FIES, the uncertainty related to the de-blazing and wavelength calibration is imperceptible, and hence they were not included to the spectral uncertainties (which was calculated in the same procedure as for eShel) seen in the right most column of Tab. 6.1.

6.1.3 Results of S indices

Having estimated the uncertainty of each spectrum observed, and being fortune to have data for both eShel and FIES, Fig. 6.5 shows a main result from this work. Plotted from top to bottom are the S index timeseries of our five targets, of increasing $\langle S \rangle$, comprised of all data from the HK Project available³ (●), our eShel observations (●), and our FIES observations (▼) observations. Errorbars are indicated by black lines for the work of this project, and with lightgrey lines for the MWO data, while the mean S values (···) and sinusoidal fits to the MWO data (—) is likewise indicated. Lastly, each panel to the right is a closeup-view in time of the eShel and FIES observations, and each panel to the left shows stellar HD name, stellar type, B magnitude, and cyclic activity period.

²The S/N technique tends to underestimate the uncertainty, which is expected as it first lack the knowledge of internal scatter (e.g. induced by cosmics or the pipeline itself), and pseudo-continuum selected can easily be overestimated.

³All measured S indices for almost 2300 stars from the Mt. Wilson HK Project was available for download from the National Solar Observatory web page: ftp://solis.nso.edu/MountWilson_HK/.

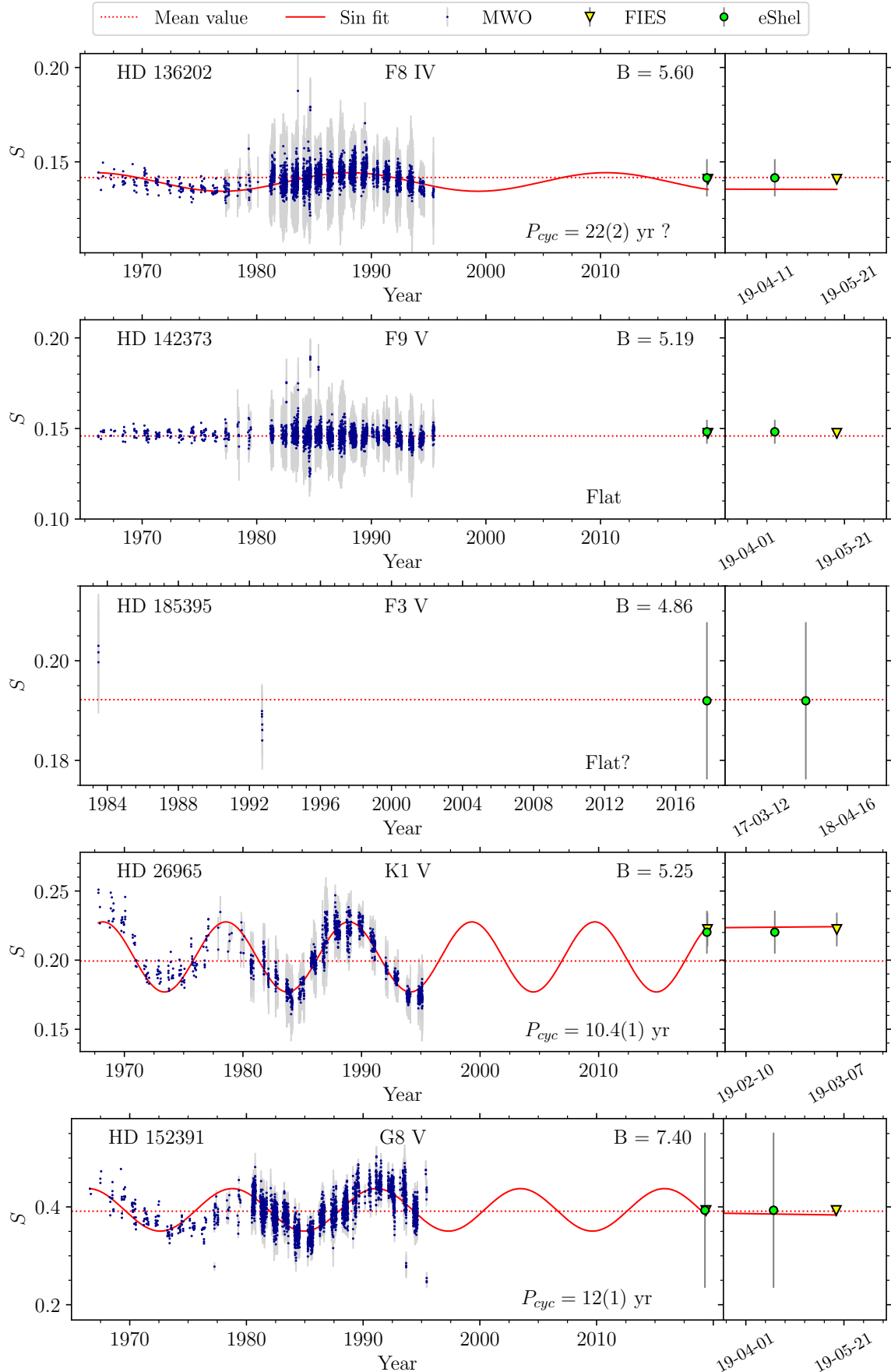


Figure 6.5: Final S index timeseries for the complete stellar sample.

Several things is noteworthy from Fig. 6.5. First there is a great correspondence between the MWO observation and our eShel/FIES observation. In fact, the predicted S indices for all five cases are all within their estimated uncertainty from the expected MWO value, whether cyclic or flat activity. The star HD 136202 is here a special case, as it from the MWO data seemingly has a period around 22 year, whereas one may argue for a completely flat timeseries from the FIES data (just as have been assumed in HK Project). Secondly, the agreement between the eShel and FIES data are very solid in all five cases. This is an extremely important fact, since without the FIES data, we would have no direct means of ensuring that any of our results are correct, which especially is true for the very active star HD 152391 that despite the large ($\sim 50\%$) uncertainty, both agrees with the FIES and MWO data, and hence can be assumed to reflect the real level of activity. In fact, even though HD 185395 only have been observed with eShel, and the observation display a relatively large uncertainty, it is not unexpected to see the eShel data agree with the sparse amount of MWO data. Thirdly, from the uncertainties of the eShel observations it is clear how the errorbar of each target is tightly related to exposure time and B magnitude (and to a lesser extent spectral type, together with weather/seeing condition). This e.g. explains the big error of HD 185395 due its exposure time of only 600 s (compared to 1200 s for the remaining targets), and HD 152391 due to its relatively high magnitude. We will resume this discussion after presenting the performance of eShel.

The fact that HD 136202 shows signs of cyclic activity may in fact highlight one of the fundamental and single most important problems of trying to determine high-precision, long-term variability, by directly comparing to data observed in the HK Project; identical “standard” stars for both instruments needs to be observed, however, many of the MWO standard stars show signs of a long-term cyclic behavior, just like HD 136202. Moreover, intrinsic variability, due to rotational modulations and/or magnetic cycles, will likewise induce noise in the calibration procedure, and ultimately set the borderline between detection and non-detection of low cyclic activity levels (Baliunas et al., 1995). From this me might even question the inclusion of the star HD 152391, since this star from the FIES α calibration, seen in Fig. 6.3 (b), seemingly shows short-term intrinsic magnetic activity. As a last notice, we have in this analysis (like so many others) assumed stellar magnetic cycles with a sinusoidal model. By physical means this is obviously an approximation. In future work given a sufficient amount of time, one may skip some of the tedious work in retrieve stellar chromospheric activity data using the database and query tool for stellar activity, `sunstardb`, developed by Egeland (2018). Data from second-generation surveys (e.g. Lowell Observatory, SMARTS, TIGRE, LCOGT, HARPS, etc) can be a strong support for validating our results.

As a last item, as part of the pipeline’s continuum normalization, we mentioned how the two maximum peaks around two pseudo-continuum points have been used to continuum normalize for the SSS at Lowell Observatory. Finding the peak maximum around each pseudo-point was done using a $\pm 0.5 \text{ \AA}$ interval. To explore how the continuum normalization effect the estimate of the eShel S index, we thus applied this method, together with the normalization of using the exact position of pseudo-points and the mean value of the spectral area around these points. Fig. 6.6 shows the spectrum before continuum normalization (—), the linear continuum fits using maximum peaks (---), exact pseudo points (-·-), and the mean values (···), together with the (downward shifted) continuum normalized spectrum (—) using the peaks as reference. First, using the local peak and mean flux value for normalization give in all cases the same result within the uncertainties of our S index estimates (hence a difference lower than $< 10^{-4}$). On the other hand, the exact

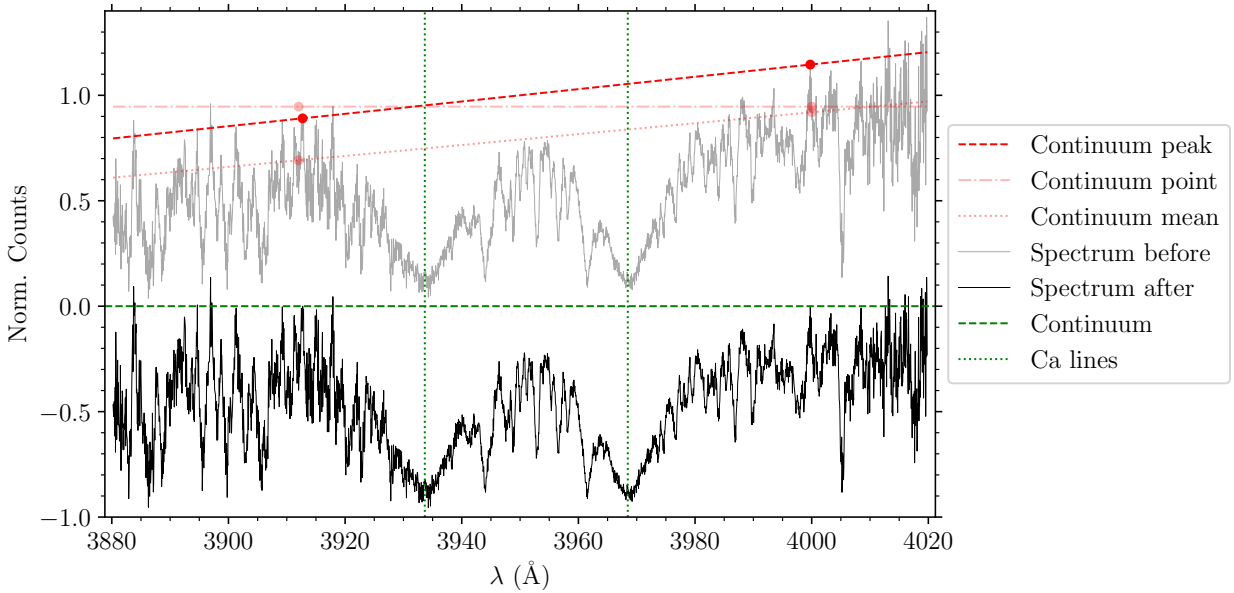


Figure 6.6: Functionality illustration of the subroutine `continuum_norm`. Shown is the spectrum before (—) and after (—) continuum normalizing using the maximum peaks (---) as reference points. Further shown is the linear continuum fits using the exact pseudo points (---) and the mean values (···). Notice that for the continuum normalized spectrum, the actual continuum is indicated by the horizontal line at 0 counts (---) and the total absorption is at -1 counts due to the vertical spectral displacement.

positions of the pseudo-points introduce a clear spurious (and maybe systematic) signal of the order $\sim 10^{-3}$. Seen from Fig. 6.6 this agrees with our expectation – while here for the example of HD 26965 it shows a completely flat continuum. The equivalence between the peak and mean normalization technique, may simply be a geometrical result of only using square bandpasses: Normalizing with a continuum having the same slope but a different flux levels should not effect the S index, since the fractional increase/decrease between bandpasses leaves $(H+K)/(R+V)$ as a conserved quantity. This hypothesis may likewise be a future test, since using a triangular H and K bandpass should, however, be effected by different slopes, but not by different flux levels if the slope is zero.

6.2 Software improvements

Since a substantial large fraction of this project have been spent on software development, it is worth while letting “the devil be in the proverbial details”, and self-critically elaborate of the short-comings of the `Blues` pipeline. In the following we therefore list all relevant updates needed to bring `Blues` to a highly professional level within near-UV observations, starting with the most severe.

Optimal extraction: Notable to this project, ground-based observations in the near-UV regime is a massive challenge for most spectrographs, and thus a true limitation of spectral quality. As discussed earlier, compared to linear extraction, optimal extraction maximizes the S/N ratio while preserving spectrophotometric accuracy, and in fact the algorithmic inventor, Horne (1986), have shown that in the regime of low S/N an optimal extraction offers a 70% gain in S/N ratio, and thus effective exposure time. In this project an important reason to use optimal extraction is due to the fact that reaching the near-UV domain was done by an adjustment of the objective lens, which we have seen introduce

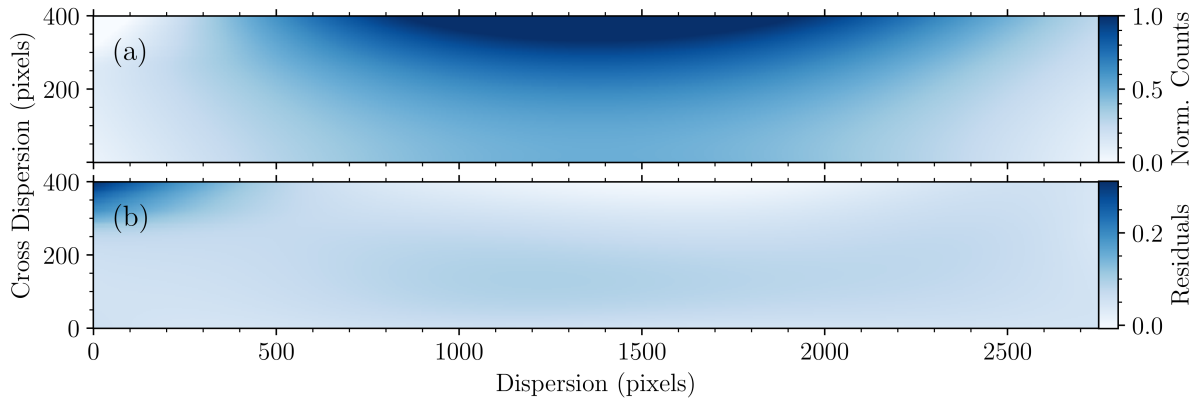


Figure 6.7: The background estimation and scattered light. The order polynomials fitting the data can be seen above each panel. The lower plot shows (a) the final estimated stellar background from the above mentioned fitting procedure, and (b) the residual background of the normalized flat and star background subtraction.

elongated order profiles and a skewed light distribution – especially clear from the arcs. Clearly this originates from the fact that only a very limited area in the focal plane are actually in optimal focus, and as such the effect introduce a clear gradually increase of the order width, for increasing pixel values in dispersion. Thus, despite our effort of finding a “Goldilock” width, in our case there is actually no such thing, and thus an additional gain in S/N ratio is expected simply using optimal extraction.

Cosmic ray contamination: At several occasions in the spectral extraction, the cosmics have contaminated our spectrum, but luckily not in any of the bandpasses used to calculate S . However, to not curse our luck, we need either to correct or reject these ambiguous high pixel counts. Although our “philosophy” is that bad data should be rejected and not repaired, we needed to correct each order-blaze to prevent obvious errors propagate into the de-blazed stellar spectra. Thus for a future update we need either (1) to develop or implement an already existing routine for repairing every single image as part of the image reduction, or (2) use optimal extraction which likewise has the advantage that the specific modeling of each spatial order profile can be used to reject cosmic rays.

Double flat-fielding: So far it may be noticed, that only flat-fielding in the sense of dividing the extracted spectra by the blaze shape of the flat-field spectrum, has been performed. Many spectroscopic pipelines (like e.g. `FIEStools`) likewise uses a flat-fielding analog to imaging, by first dividing the non-extracted frame by a normalized 2D flat to remove pixel-to-pixel sensitivity, for then later to de-balze. We may here reason to why we have not done the first flat-fielding. From the background fits (illustrated in Fig. 5.5), it is quite clear that the low stellar background level makes it more difficult to estimate the “true” sky background, compared to the flat background. The estimation of the stellar background seen in Fig. 6.7 (a) shows not surprisingly a pronounced light gradient from high to low wavelengths. Keeping in mind that the stellar background depends on spectral type, and that the flat exposure produce a Planck profile of 2800 °C, Fig. 6.7 (b) shows the residual background image of the normalized flat and star background subtracted. By normalization the residuals is in percentage, and the plot shows that for most of the CCD workspace the difference in flat-to-star scattered light is less than 5%, though with a deviation of about 20% in the upper left corner, owing to lack of orders traced here. Since a $\sim 5\%$ deviation was observed for all of our targets, the light scattering may be profoundly different between the two, and it was left for future investigations.

Automatic wavelength calibration: Presented in last chapter, the success of our wavelength calibration depends on a manual selection of initial arc lines. This is very unfit method, since for any future change the same set of lines needs identification once again. The routine thus needs fully atomization which e.g. can be done by finding abundant lines in correspondence to the spectral type that is being analyzed (e.g. strong and narrow FeI are seen for most of our targets, and TiO lines for our K dwarf star).

6.3 System performance

Lastly, we now resume to the main project goal, namely determine if the performance of eShel is sufficient for any future prospects. To answer this question we thus need to go through several important elided quality checks of BlueSONG. Hence, in this section we address and discuss the overall throughput and performance of eShel, and will do so in the context of future work and improvements.

6.3.1 Guiding, Focus, & Fiber transmission

To date no telescope is capable of pointing to a star right on the micrometer-precision of a slit/fiber relying only on the pointing capabilities of the telescope mount. As a natural consequence every professional telescope use the principle of *guiding* by continuously measuring the stellar position of the target star (or in photometry a star close by). In the special case of fiber-feed spectroscopic observations, continuously centering the target onto the fiber is more difficult as the stellar position needs to be determined from the excess of light not entering the fiber. Within the FIGU this light excess comes from the light reflected from a fixed mirror with a 50 μm diameter hole. For illustration left plot of Fig. 6.8 shows a 2.5'' seeing limited guide image, respectively, with the 1.7'' diameter hole inside.

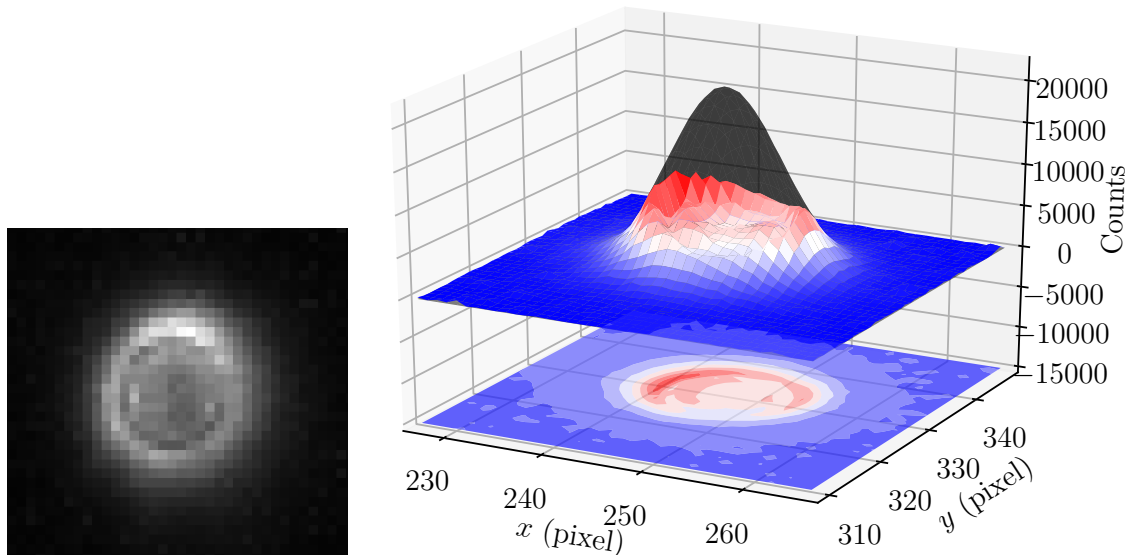


Figure 6.8: Fiber acquisition images showing a single 2.5'' seeing limited image directly from the guide camera (left) and a surface plot of 2.5'' seeing limited median filtered image for an entire 1200 s observation. The darkgray surface plot, is a fitted Gaussian profile to the seeing limited contour.

As f depends on temperature, pressure, humidity, etc. even for two consecutive nights the focus of the telescope may vary significantly, thus, before any observation an auto-focus algorithm finds the optimal focus using guide images (see Appendix A explanation of the algorithm). For now the auto-focus algorithm uses a default focus value to calculate the best focus. For consecutive observations this introduces overheads, as the default value might be far off compared to the value estimated in the previous observation. More important is the fact that the focus is only determined before an observation, hence, varying seeing during a run will introduce light loss, which in ultimately means lower performance. These subjects therefore may be considered in a future update.

The clear advantage of FIGU’s “mirror-slit”, is that we see exactly what happens at the fiber entrance, making it straight forward to determine e.g. coupling efficiency, seeing, atmospheric dispersion, and fiber transmission. In fact accounting for observational seeing, from the fiber-guide image of Fig. 6.8 (left) we can confirm from the light excess that the coupling efficiency is very close to optimal. Also, from a vast rendering of guide images grabbed at different altitude, it is clear that (1) atmospheric dispersion is a minor effect as long as $\phi_{\text{zenith}} > 30^\circ$, and (2) the guiding works very well, due to the very high motion state precision of SONG and the robust guide-algorithm determine the stellar COF.

Lastly, fiber attenuation, i.e. the transmission of light in, through, and out of the fiber, can also be estimated. Usually fiber attenuation is above 90%, where the loss in fiber optics happens mainly at the ends, with the connectors. Even spanning up to some dozens of meters, the transmission of the fiber itself is close to 100% stated by most companies. This is good news as we use fibers of 20 m in length. Fabricated by Shelyak the object fibers optics are of type “High-OH”, offering a very good performance for blue light and generally in the spectral range 3800-8000 Å. An approximate and intuitive way to calculate the fiber transmission and the combined efficiency of fiber transmission, guiding, and focus was done by median-combine all guide images during a complete observational run, as seen in the hot-cold surface plot of Fig. 6.8. The hot-cold guide-image projection below do actually show a asymmetric structure, which most likely are signs of atmospheric dispersion, as this specific target acquisition was started at (and decreased from) a altitude of 58% (which from Fig. 4.2 nicely agrees with a dispersion of around 0.5'').

Assuming a stable seeing during the observation and that the stellar profiles are Gaussian, computing the difference between the fitted 3D Gaussian (see darkgrey Gaussian surface profile in the same figure) and the actual image, the fiber transmission was calculated to be $\sim 70\%$ within 1.7'' aperture of the object-fiber and $\sim 55\%$ within 2.5'' observational runs of 1200 s. The former estimate actually highlight a significant throughput problem of BlueSONG. From my last visit to Tenerife in 2017, the object-fiber was seemingly found to be mounted incorrectly. However, from a recent SONG service visit by Mads Fredslund and Frank Grundahl, the object-fiber was both visually inspected by shining light through it but also connecting it to the SONG spectrograph; in both cases very a small throughput could be reported. This in fact suggest that the object-fiber is indeed damaged, and most likely needs replacement. Drawing a (cautious) conclusion from the measured throughput of 70%, replacing the object-fiber might result in a gain in effective exposure time of $\sim 30\%$.

6.3.2 CCD Detectors

So far no considerations of efficiency for the CCD detector and optics (focal-reducer, collimator, and objective) have been made. First let us consider the detectors used in the BlueSONG setup. Since the first astronomical Charged Coupled Device (CCD) sensors in

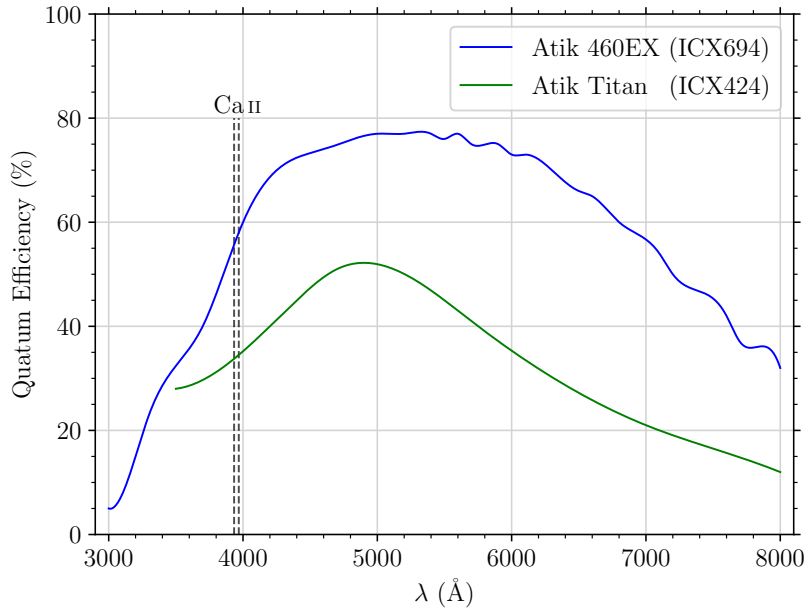


Figure 6.9: Quantum efficiency as function of wavelength for the acquisition camera Atik 460EX (—), and the guide camera Atik Titan (—). The Ca II lines are shown for reference. Notice these plots are the theoretical QE profiles provided by the manufacturers, and hence the real QE profiles may be significantly different from these.

1957 saw the light of day it quickly replaced photographic plates and other early solid-state imaging devices due to its ease of use and superior Quantum Efficiency (QE) (Lesser, 2015). The QE is an expression of how well incoming photons translates into electrons, hence, an ideal image sensor with QE = 100 % will count every single photon incident on the sensor.

As a first quality test, Fig. 6.9 shows the average QE for the Atik 469EX (—) and Aktik Titan (—) camera, respectively.⁴ With the Ca II lines as a reference one may first of all notice that the detector provide very satisfying QE over a broad wavelength range and, secondly, with a QE of about 55% around 4000 Å the Atik 460EX is very well suited as a science acquisition camera for this project. In fact the Sony ICX694 provides the highest QE near the Ca II among all the Sony sensors used by Atik. The Aktik Titan guide camera is likewise tailored for this projects as it covers a fair QE in the range 4500–6500 Å in correspondence to the peak emission of FGK type stars – e.g. recalling from Fig. 2.1 that a (early-type G dwarf) black body spectrum of $T_{\text{eff}} = 6000 \text{ K}$ peaks around 5000 Å.

Looking back on the atmospheric dispersion equation (4.5), Fig. 4.2 shows that the dispersion is largest for blue wavelengths at fixed airmass, which further complicates near-UV observations: if guiding on a particular wavelength of light, the object at other wavelengths will move out of the fiber, and observing at a high airmass this effect will naturally be amplified. As we are only interested in the spectral domain around 4000 Å a workaround could be to use a near-UV sensitive camera or using blue filter. However, this will be on the expense of less light to guide on. Following the discussion here, the QE of our guide camera peaks towards wavelengths of hotter solar-type stars, we may therefore conclude that, as long observations are made above an airmass of 2, the Atik Titan camera is a efficient guide camera for this project.

⁴Provided by <https://www.atik-cameras.com/>

6.3.3 Focal-reducer, Collimator, and Objective

As a next quality check, we need to consider light transmission of the remaining optical elements: focal reducer, collimator, and objective – with the two latter being included in the “package solution” bought from Shelyak. The simple and most important reason why this is needed, is due to the fact that most optical elements are far from optimized towards the near-UV/UV domain. The ThorLab lens-focal reducer⁵ mounted at the entrance of the FIGU, uses two so-called UV fused silica Plano-Convex spherical lenses which usually have a clear central aperture transmission of $\sim 85\%$ for optical light.

Next, light emitted from the object-fiber is collimated by a collimator doublet specifically made for eShel. Since the installation of eShel, a upgrade kit for the eShel collimator have been developed, which optical component is optimized to increase the range of spectral domain achievable, particular in the blue part of the spectrum.⁶ With the new doublet the Ca II H & K order (order $m = \#57$) can almost be reached with a standard objective focus, allowing to use the entire spectral range from 4000–7500 Å (or from #30 to #53) without any problems. Hence, this should strongly be considered since the application of heavy defocussing, as already mentioned for our pipeline, creates some serious problems. Unfortunately, no direct information on the performance of the two can be found anywhere on Shelyak’s website, and further correspondence is needed for clarification. However, with a standard focus of the objective lens, Shelyak do provide the measured spectral resolving power as function wavelength for the old (■) and new (◆) collimator as seen in Fig. 6.10. Hence, with the new lens the objective needs only a slightly adjustment to create a good focus in the Ca II H & K order. As the camera mount is fixed on eShel, another solution to bypass the heavy defocussing of the optical spectral domain, is by changing the so-called *shifting angle* γ , in order to move order #57 centrally onto the CCD detector. This will clearly effect the grating efficiency, but it might be worth doing because, first,

⁵<https://www.thorlabs.com/>

⁶<https://www.shelyak.com/improved-performance-of-the-eshel-spectroscopic/?lang=en>.

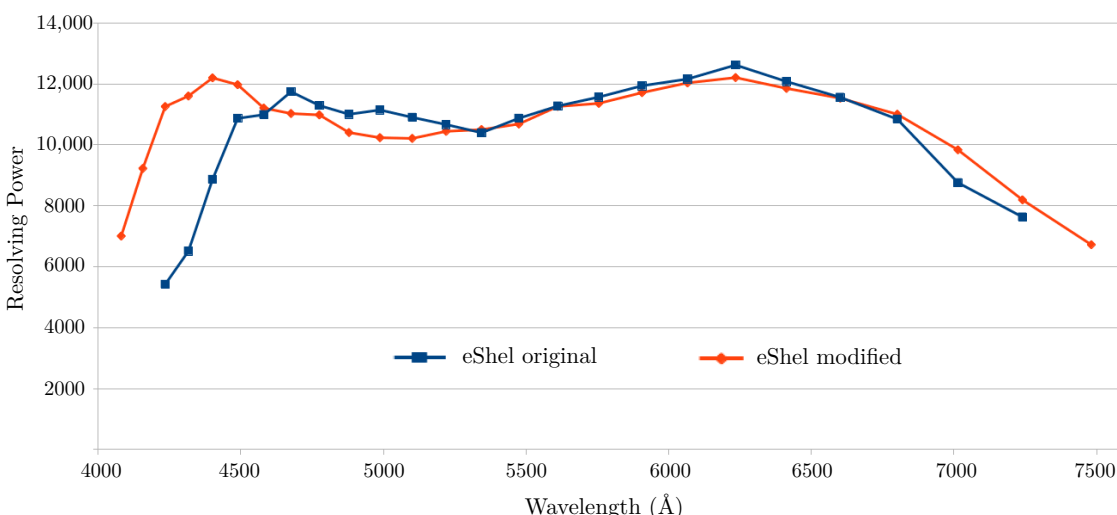


Figure 6.10: eShel resolving power as function of wavelength for a standard objective focus with the original (■) and modified (◆) version of eShel. The single update here is a change of collimator doublet, which for the new version allows a higher resolution in the deep blue, and therefore a higher efficiency. This figure is produced by Shelyak Instruments – only labels have been updated from French to English.

CCD detectors are usually more sensitive at their center. Secondly, the objective might only need a small adjustment to focus a larger fraction of the focal plane, and thus a better focus may be possible for order #57 and successive orders around it. This in turn will give rise to more well-defined spatial orders, and hence give better results both for the linear and optimal extraction procedure.

Already mentioned by Shelyak, another limiting element for exploiting the near-UV spectral domain is the usage of the $f/1.8$ 85 mm Canon EOS objective lens. This is a very popular DSLR lens used by many amateur photographers, however, several aspects about this lens makes it highly unfit for the wavelength domain at hand. First we might notice that this lens have 9 optical glass elements in 7 groups, and hence light thus needs to travel through ~ 5 cm of glass. Using the general optimistic rule-of-thumb in optics, which is for every 1 cm of glass light needs to travel through, an efficiency of 90% is expected, for our Canon lens this gives $0.9^5 \approx 0.6$, meaning 40% loss of light by this element alone. This might even be an upper limit, since there additionally will be reflection losses which, for a non UV-optimized lens like we use here, increases with decreasing wavelength.

6.3.4 Effective exposure time

From Chapter 4 it was seen how the S/N ratio estimated for an initial observation of θ Cyg, was used to set an approximate exposure time for our observations. With the now reduced spectra and estimated S/N ratios for each observation, we are able to make a more broad prediction of what S/N ratio as function of effective exposure time we should expect for the diverse apparent magnitudes in our stellar sample. To do this we used the calculated S/N ratios together with the following representation of the S/N ratio

$$S/N = C 10^{-mx/2.5} \quad (6.10)$$

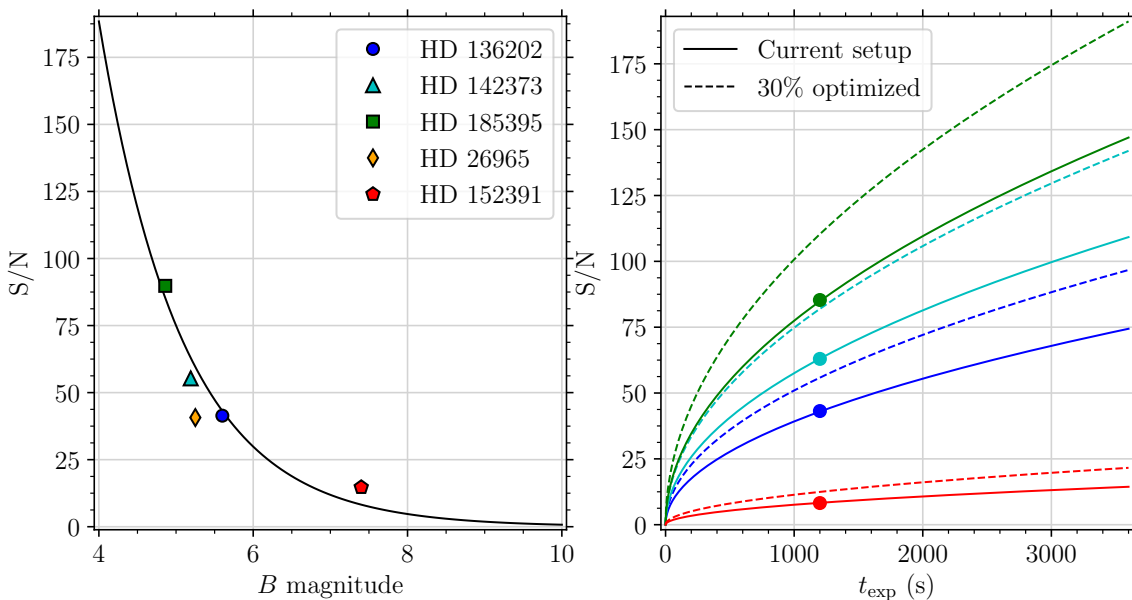


Figure 6.11: S/N ratio as a function of B magnitude (left) and effective exposure time (right). The left plot have been used to infer a S/N ratio (—), for which in the right plot have been used to estimate the effective exposure time, t_{exp} for our current setup (—), and possible future 30% optimized setup (---).

which in fact just is (4.2) with $S/N = F_2$ and $C = F_1$. We have in Fig. 6.11 (left) plotted our estimated S/N ratios against B magnitude for each target, and the data fit using (6.10). We see some clear fluctuations, however, this is expected since different spectral types are used (e.g. HD 26965 which is a K dwarf star). By evaluating each S/N ratio from the fit, next using the fact that $S/N \propto \sqrt{t}$ (Schroeder, 1999) and reinforcing the S/N ratios from this relation to match exactly the S/N ratios calculated from (6.10) at a exposure time of 1200 s, seen as the respective filled dots in the right-hand plot of Fig. 6.11. From each solid curve an effective exposure time for our current setup can be seen for different stellar magnitudes. By the discussion of this section, we have seen that a significantly fraction of light is lost in translation, hence, assuming a future update of BlueSONG can deliver a 30% higher efficiency, we recalculated the S/N ratio as a function of exposure time as the result is shown with dashed lines for the same four stars. We have seen in this project that an S/N ratio of around 40 is sufficiently for our targets to follow the flat and cyclic activity cycles. Seen from Fig. 6.11 this means if e.g. an exposure time of 1200 s is the maximum allowed, stars with a B magnitude higher than $B \sim 5.5$ are simply too faint to meet the requirements. Although it may be noticed that our stellar sample is heavily biased towards the brighter posterior of the HK stars. Thus being able to monitor dimmer stars, a S/N ratio around 70 or higher should probably be preferred.

6.3.5 Optimizing the calibrating

From the aspects we have rendered, it is already clear that much can be done to optimize the throughput of BlueSONG. In continuation this is likewise true for the calibration, specifically referring to the effective exposure time of 1200 s used for flats and ThAr images. Though alarmingly high, to test eShel these exposure times do not limit SONG's asteroseismic observations, neither our or SONG's observations, since calibration was done during daytime. However, having experienced that both the ThAr lamp, Tungsten, and LED lamps died, the exposure time needs to be lowered for any future operation. Besides the solution of ensuring a higher transmission for the object-fiber, Fig. 6.12 shows two guide images of how the object-fiber is illuminated by calibration light inside the FIGU. Left shows the original setup provided by Shelyak, and right shows the current setup,

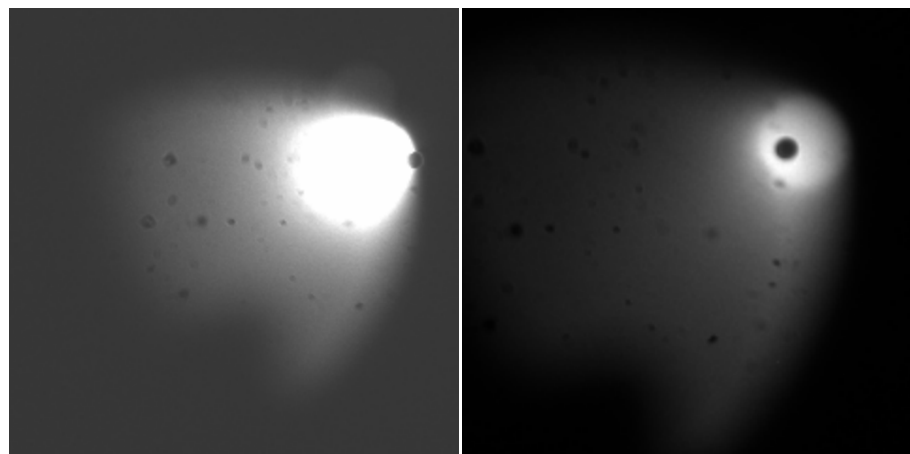
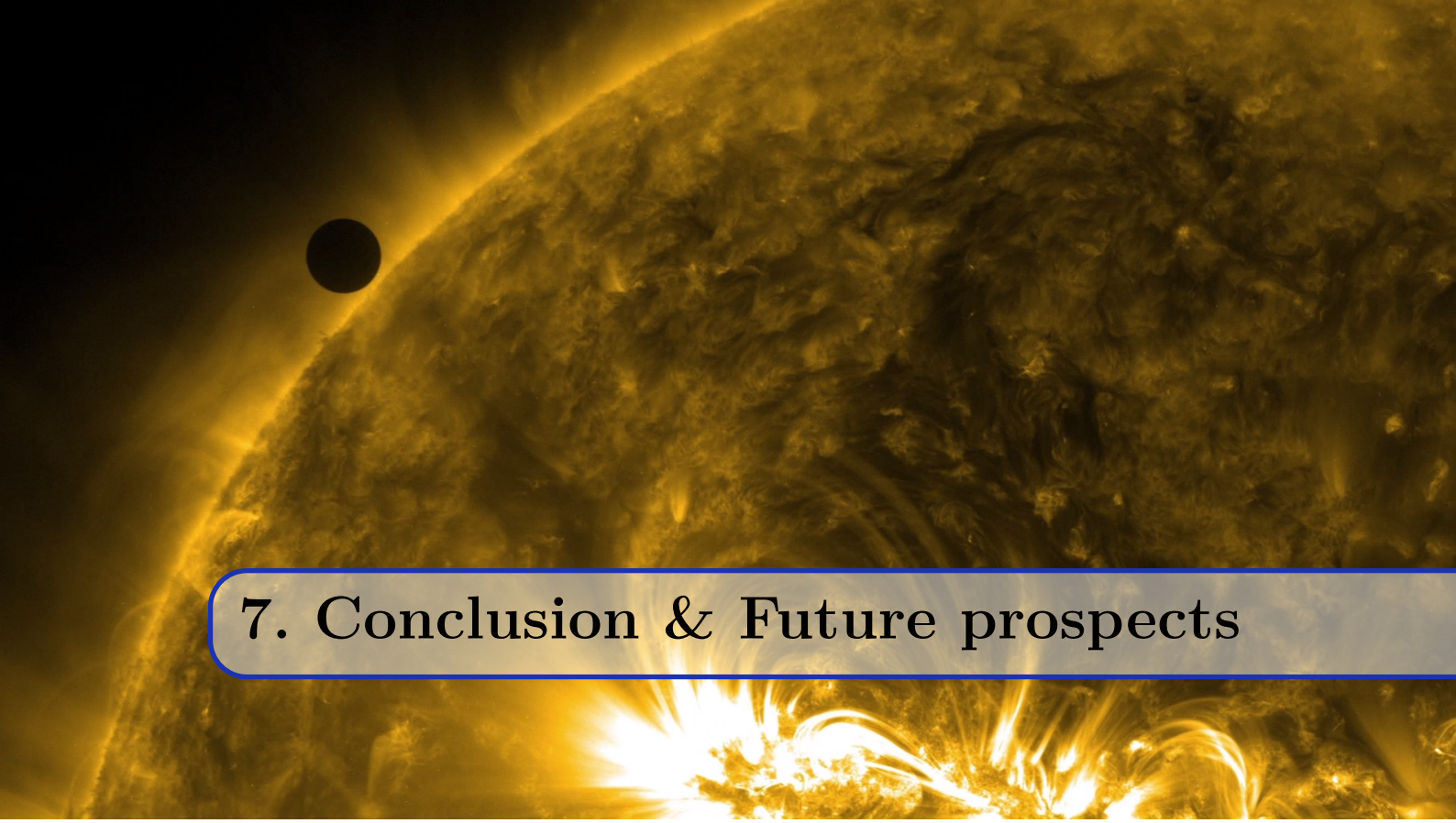


Figure 6.12: Two flats images taking with the guide camera showing the object fiber (or more precise the whole in the mirror) as a black dot and the reflected light from the flip-mirror. Left shows a guide image before adjusting to the COF, and right shows after the adjusting to the COF.

which was adjustment in September 2017 on a service visit to Tenerife. Lowering the effective exposure even more thus involves first identify and correct for the misalignment that introduce the “comet-like” light shape, for hereafter aligning/adjusting the fiber-tip of the object fiber to the COF of the flat (and ThAr) illumination. How these can be done in practice is described in Appendix B. Even with these adjustments it may be noted that the flat lamp may even be a limiting factor in itself due to the low temperature spectrum of 2800 K for the Tungsten lamp.



7. Conclusion & Future prospects

The “proof of concept” of this project have involved the commercial échelle spectrograph, *eShel*, mounted on the fully robotic Hertzsprung SONG telescope on Tenerife, to trace stellar magnetic activity in the Ca II H & K lines of solar-type stars. The fundamental idea behind *eShel* is first of all to estimate at the precision yield in near-UV for a commercial spectrograph and, secondly, what is the potential of using a commercial spectrograph for observing stellar cycles with SONG. Since receiving a sufficient emission excess in the near-UV is widely known to be challenging task, and even so for highly optimized and stable spectrographs, this project is to our knowledge the first of its kind.

Being the final outcome of thesis, testing the spectroscopic system was done comparing observations of solar-type stars obtained with *eShel* together with simultaneous observations made with the FIES spectrograph at the NOT, to that of the Mount Wilson survey. We can report a successful outcome of this project proving that *eShel* in fact can be used to trace stellar magnetic activity of solar-type stars, however, for now only efficiently on the brighter half of the HK Project’s stellar sample. Indeed a lot can be done to optimize the instrumentation, and therefore one may argue for simply building a new spectrograph that of-the-shelf can deliver the spectrophotometric quality needed to even go beyond the stellar magnitudes investigated in the thesis, and even that of the MWO observations. Ultimately, such a decision will depend on the combined efficiency of BlueSONG, which for now only can be gleaned from a list of erroneous items. The reason hereto is, that one would physically need the spectrograph for specific tests and, secondly, because it seems evident that observations have been done with a damaged object-fiber. Thus, it will be worthwhile trying to update these limiting instrumental parameters, to explore the full potential of *eShel*. To do this we propose the following updates and considerations

- **Determine exact attenuation of the fibers:** If the object-fiber is damaged it needs to be replaced.
- **Replace the objective:** (the Canon lens) with e.g. a simple ThorLab lens. Here it might be worth to look into near-UV optimized lenses.

- **Perhaps update to Shelyak's new collimator:** which by a standard focus-procedure reach down to order #53 without any problems.
- **Look into a new configuration:** where order #57 can be placed centrally on the CCD tip. This necessarily involves changing the spectroscopic parameters of the grating.
- **Optimize the the calibration procedure:** Its obvious that if the object-fiber is damaged or the throughput of eShel can be optimized, so will the data acquisition for the calibration. An optimization of the object-fiber illumination is likewise needed.
- **Ceil eSehl:** Since eShel (possibly like any other affordable spectrograph) is leaky, light from within the container (or outside during daytime) contaminate the spectrum, and introduce an additional light scattering. Thus, after all tests have been performed, we need to ceil the spectrograph with duck-tape.
- **Use optimal extraction:** A mentioned earlier the clear advantage of optimal extraction, compared to linear extraction, comes from its ability to optimize the spectrophotometric quality and its ability to reject comics. We may emphasize the need here, since levels of $S/N < 50$ are especially effected towards a much higher spectrophotometric precision. Also in general a clear goal would be to make Blues a fully automated pipeline integrated into a (hopefully near-future) fully automatic eShel-SONG spectroscopic system.
- If eShel after all of these updates stand the test, it might be worth investigating if SONG's ADC can be used with eShel.

With all these updates mentioned, a work plan have already been discussed and planned, which is outlined in Appendix B. Despite all the complications that have been experienced throughout this work, eShel has actually come to surprise us with its sufficient accuracy to demonstrate stellar cycles in other solar-type stars. Hence, although far from sufficient, eShel *is* a tool for observing stellar magnetic activity cycles. Hence, with the ultimate future prospect of successfully showing that an off-the-shelf spectrograph like eShel can be used to *efficiently* investigate stellar activity for solar-like stars, projects like this thesis might be key to monitor stellar cycles, and thus get a better understanding of the solar-stellar connection.

Bibliography

- Andersen, M. F., R. Handberg, E. Weiss, S. Frandsen, S. Simón-Díaz, F. Grundahl, and P. Pallé (2019). Conducting the song: The robotic nature and efficiency of a fully automated telescope. *Publications of the Astronomical Society of the Pacific* 131(998), 045003.
- Babcock, H. (1961). The topology of the sun's magnetic field and the 22-year cycle. *The Astrophysical Journal* 133, 572.
- Baliunas, S. á., R. Donahue, W. Soon, J. Horne, J. Frazer, L. Woodard-Eklund, M. Bradford, L. Rao, O. Wilson, Q. Zhang, et al. (1995). Chromospheric variations in main-sequence stars. *The Astrophysical Journal* 438, 269–287.
- Barden, S. C. (1988). *Fiber optics in astronomy*, Volume 3. Astronomical Society of the pacific.
- Barker, P. (1984). Ripple correction of high-dispersion iue spectra-blazing echelles. *The Astronomical Journal* 89, 899–903.
- Böhm-Vitense, E. (2007). Chromospheric activity in g and k main-sequence stars, and what it tells us about stellar dynamos. *The Astrophysical Journal* 657(1), 486.
- Borucki, W. J., D. G. Koch, N. Batalha, S. T. Bryson, J. Rowe, F. Fressin, G. Torres, D. A. Caldwell, J. Christensen-Dalsgaard, W. D. Cochran, et al. (2012). Kepler-22b: a 2.4 earth-radius planet in the habitable zone of a sun-like star. *The Astrophysical Journal* 745(2), 120.
- Bowers, C. and D. Lindler (2003). Stis echelle blaze shift correction. In *HST Calibration Workshop: Hubble after the Installation of the ACS and the NICMOS Cooling System*, pp. 127.
- Bradt, H. (2004). *Astronomy methods: A physical approach to astronomical observations*. Cambridge University Press.
- Chaplin, W., Y. Elsworth, G. Houdek, and R. New (2007). On prospects for sounding activity cycles of sun-like stars with acoustic modes. *Monthly Notices of the Royal Astronomical Society* 377(1), 17–29.
- Christensen-Dalsgaard, J. (2008). *Lecture notes on stellar structure and evolution*. Aarhus Universitet. Institute for Fysik og Astronomi.
- Clayton, M. (1996). Introduction to echelle spectroscopy. *Starlink Guide 9*.
- Cochard, F. (2018). *Successfully Starting in Astronomical Spectroscopy - A Practical Guide*, Volume 1. EDP Sciences.

- Duncan, D. K., A. H. Vaughan, O. C. Wilson, G. W. Preston, J. Frazer, H. Lanning, A. Misch, J. Mueller, D. Soyumer, L. Woodard, et al. (1991). Ca ii h and k measurements made at mount wilson observatory, 1966-1983. *The Astrophysical Journal Supplement Series* 76, 383–430.
- Eberhard, G. and K. Schwarzschild (1913). On the reversal of the calcium lines h and k in stellar spectra. *The Astrophysical Journal* 38.
- Eddy, J. A. (1976). The maunder minimum. *Science* 192(4245), 1189–1202.
- Egeland, R. (2018). sunstardb: A database for the study of stellar magnetism and the solar-stellar connection. *The Astrophysical Journal Supplement Series* 236(1), 19.
- Egeland, R., W. Soon, S. Baliunas, J. C. Hall, A. A. Pevtsov, and L. Bertello (2017). The mount wilson observatory s-index of the sun. *The Astrophysical Journal* 835(1), 25.
- Engel, M., S. Shahaf, and T. Mazeh (2017). The eshel spectrograph: A radial-velocity tool at the wise observatory. *Publications of the Astronomical Society of the Pacific* 129(976), 065002.
- Eversberg, T. (2016). Off-the-shelf echelle spectroscopy: Two devices on the test block. *Publications of the Astronomical Society of the Pacific* 128(969), 115001.
- Fabricius, J. (17th). De maculis in sole observatis. *Wittenbergae, MDCXI*.
- García, R. A., S. Mathur, D. Salabert, J. Ballot, C. Régulo, T. S. Metcalfe, and A. Baglin (2010). Corot reveals a magnetic activity cycle in a sun-like star. *Science* 329(5995), 1032–1032.
- Gray, D. F. (2005). *The observation and analysis of stellar photospheres*. Cambridge University Press.
- Hale, G. E. (1908). On the probable existence of a magnetic field in sun-spots. *The astrophysical journal* 28, 315.
- Hall, J. C. (2008). Stellar chromospheric activity. *Living Reviews in Solar Physics* 5(1), 2.
- Hall, J. C., G. Lockwood, and B. A. Skiff (2007). The activity and variability of the sun and sun-like stars. i. synoptic ca ii h and k observations. *The Astronomical Journal* 133(3), 862.
- Horne, K. (1986). An optimal extraction algorithm for ccd spectroscopy. *Publications of the Astronomical Society of the Pacific* 98(604), 609.
- Howell, S. B. (2006). *Handbook of CCD astronomy*, Volume 5. Cambridge University Press.
- Isaacson, H. and D. Fischer (2010). Chromospheric activity and jitter measurements for 2630 stars on the california planet search. *The Astrophysical Journal* 725(1), 875.
- Ivezić, Ž., A. J. Connolly, J. T. VanderPlas, and A. Gray (2014). *Statistics, Data Mining, and Machine Learning in Astronomy: A Practical Python Guide for the Analysis of Survey Data*. Princeton University Press.
- Karoff, C., T. Metcalfe, B. Montet, N. Jannsen, A. Santos, M. Nielsen, and W. Chaplin (2019). Sounding stellar cycles with kepler–iii. comparative analysis of chromospheric, photometric and asteroseismic variability. *Monthly Notices of the Royal Astronomical Society*.

- Karoff, C., T. S. Metcalfe, W. J. Chaplin, Y. Elsworth, H. Kjeldsen, T. Arentoft, and D. Buzasi (2009). Sounding stellar cycles with kepler–i. strategy for selecting targets. *Monthly Notices of the Royal Astronomical Society* 399(2), 914–923.
- Keil, S. and S. Worden (1984). Variations in the solar calcium k line 1976–1982. *The Astrophysical Journal* 276, 766–781.
- Kiefer, R., A. Schad, G. Davies, and M. Roth (2017). Stellar magnetic activity and variability of oscillation parameters: An investigation of 24 solar-like stars observed by kepler. *Astronomy & Astrophysics* 598, A77.
- Kippenhahn, R., A. Weigert, and A. Weiss (1990). *Stellar structure and evolution*, Volume 192. Springer.
- Koch, D. G., W. J. Borucki, G. Basri, N. M. Batalha, T. M. Brown, D. Caldwell, J. Christensen-Dalsgaard, W. D. Cochran, E. DeVore, E. W. Dunham, et al. (2010). Kepler mission design, realized photometric performance, and early science. *The Astrophysical Journal Letters* 713(2), L79.
- Lesser, M. (2015). A summary of charge-coupled devices for astronomy. *Publications of the Astronomical Society of the Pacific* 127(957), 1097.
- Lingam, M. and A. Loeb (2018). Physical constraints for the evolution of life on exoplanets. *arXiv preprint arXiv:1810.02007*.
- Lovis, C., X. Dumusque, N. Santos, F. Bouchy, M. Mayor, F. Pepe, D. Queloz, D. Ségransan, and S. Udry (2011). The harps search for southern extra-solar planets. xxxi. magnetic activity cycles in solar-type stars: statistics and impact on precise radial velocities. *arXiv preprint arXiv:1107.5325*.
- Metcalfe, T., W. Dziembowski, P. Judge, and M. Snow (2007). Asteroseismic signatures of stellar magnetic activity cycles. *Monthly Notices of the Royal Astronomical Society: Letters* 379(1), L16–L20.
- Metcalfe, T. S., P. Judge, S. Basu, T. Henry, D. Soderblom, M. Knoelker, and M. Rempel (2009). Activity cycles of southern asteroseismic targets. *arXiv preprint arXiv:0909.5464*.
- Palmer, C. A. and E. G. Loewen (2005). *Diffraction grating handbook*. Newport Corporation New York.
- Planck, M. (1914). The theory of heat radiation, translated by m. *Masius, P. Blackiston's Son & Co, Philadelphia, reprinted by Kessinger*.
- Roberts, W. O. (1945). A preliminary report on chromospheric spicules of extremely short lifetime. *The Astrophysical Journal* 101, 136.
- Saar, S. H. and A. Brandenburg (1999). Time evolution of the magnetic activity cycle period. ii. results for an expanded stellar sample. *The Astrophysical Journal* 524(1), 295.
- Schmitt, J., K.-P. Schröder, G. Rauw, A. Hempelmann, M. Mittag, J. González-Pérez, S. Czesla, U. Wolter, D. Jack, P. Eenens, et al. (2014). Tigre: A new robotic spectroscopy telescope at guanajuato, mexico. *Astronomische Nachrichten* 335(8), 787–796.
- Schroeder, D. J. (1999). *Astronomical optics*. Elsevier.

- Schwabe, H. (1844). Sonnenbeobachtungen im jahre 1843. von herrn hofrath schwabe in dessau. *Astronomische Nachrichten* 21, 233.
- Simon, T., T. R. Ayres, S. Redfield, and J. L. Linsky (2002). Limits on chromospheres and convection among the main-sequence a stars. *The Astrophysical Journal* 579(2), 800.
- Siverd, R. J., T. M. Brown, S. Barnes, M. K. Bowman, J. De Vera, S. Foale, D.-R. Harbeck, T. Henderson, J. Hygelund, A. Kirby, et al. (2018). Nres: the network of robotic echelle spectrographs. In *Ground-based and Airborne Instrumentation for Astronomy VII*, Volume 10702, pp. 107026C. International Society for Optics and Photonics.
- Škoda, P., B. Šurlan, and S. Tomić (2008). Investigation of residual blaze functions in slit-based echelle spectrograph. In *Ground-based and Airborne Instrumentation for Astronomy II*, Volume 7014, pp. 70145X. International Society for Optics and Photonics.
- Smart, W. M., W. Smart, and R. Green (1977). *Textbook on spherical astronomy*. Cambridge University Press.
- Telting, J., G. Avila, L. Buchhave, S. Frandsen, D. Gandolfi, B. Lindberg, H. Stempels, and S. Prins (2014). Fies: The high-resolution fiber-fed echelle spectrograph at the nordic optical telescope. *Astronomische Nachrichten* 335(1), 41–45.
- Thizy, O. and F. Cochard (2010). Spectrographs for small telescopes. *International Astronomical Union. Proceedings of the International Astronomical Union* 6(S272), 282.
- Varela, A., C. Muñz-Tuñón, A. de Gurtubai, and C. Saviron (2002). Site-testing results at the teide observatory. In *Astronomical Site Evaluation in the Visible and Radio Range*, Volume 266, pp. 454.
- Vaughan, A. H. and G. W. Preston (1980). A survey of chromospheric ca ii h and k emission in field stars of the solar neighborhood. *Publications of the Astronomical Society of the Pacific* 92(548), 385.
- Vaughan, A. H., G. W. Preston, and O. C. Wilson (1978). Flux measurements of ca ii and k emission. *Publications of the Astronomical Society of the Pacific* 90(535), 267.
- Vernazza, J. E., E. H. Avrett, and R. Loeser (1981). Structure of the solar chromosphere. iii-models of the euv brightness components of the quiet-sun. *The Astrophysical Journal Supplement Series* 45, 635–725.
- White, O. and W. Livingston (1981). Solar luminosity variation. iii-calcium k variation from solar minimum to maximum in cycle 21. *The Astrophysical Journal* 249, 798–816.
- Wilson, O. (1968). Flux measurements at the centers of stellar h-and k-lines. *The Astrophysical Journal* 153, 221.
- Wilson, O. (1978). Chromospheric variations in main-sequence stars. *The Astrophysical Journal* 226, 379–396.
- Wright, J. and J. Eastman (2014). Barycentric corrections at 1 cm s-1 for precise doppler velocities. *Publications of the Astronomical Society of the Pacific* 126(943), 838.
- Wynne, C. and S. Worswick (1986). Atmospheric dispersion correctors at the cassegrain focus. *Monthly Notices of the Royal Astronomical Society* 220(3), 657–670.

List of Figures

2.1	Illustration of the Sun's continuum.	6
2.2	Photographs of the solar photosphere, chromosphere, and spicules	8
2.3	Chromospheric toy-model of the Sun from Vernazza et al. (1981)	9
2.4	Illustration of energy transport zones for in main-sequence stars	11
3.1	Illustration of an a slit, fiber, and grism.	16
3.2	Schematic drawing of light diffracted by a prism and an échelle grating	17
3.3	Schematic drawing of an optimal spectroscopic system	19
3.4	Schematic drawing of BlueSONG	20
3.5	Setup of FIGU and eShel	21
3.6	Transparent view of the eShel spectrograph	23
4.1	Schematic view of the size of the stellar disk image at the focal plane	27
4.2	Atmospheric dispersion as a function zenith distance and airmass	28
4.3	Reduced calibration images	31
5.1	Schematic drawing of data reduction pipeline Blues.	34
5.2	Full échelle spectrum of the star HD 26965.	35
5.3	Functionality illustration of the subroutine <code>trace</code> .	36
5.4	Functionality illustration of the subroutine <code>make_inter_order_mask</code> .	37
5.5	Functionality illustration of the subroutine <code>background</code>	38
5.6	Functionality illustration of the subroutine <code>spectral_extraction</code> .	39
5.7	Functionality illustration of the utility <code>find_optimal_width</code> .	40
5.8	Functionality illustration of the subroutine <code>wavelength_calib</code>	41
5.9	Functionality illustration of the subroutine <code>find_blaze_function</code>	43
5.10	Annual drifts of the ThAr line positions on the CCD	46
6.1	Illustrative example for the calculation of the S index.	48
6.2	Illustration of different H and K bandpasses	49

6.3	Determination of the α coefficient	51
6.4	Illustration of the S index uncertainty estimation.	52
6.5	Final S index timeseries for the complete stellar sample	54
6.6	Functionality illustration of the subroutine <code>continuum_norm</code>	56
6.7	The background estimation and scattered light	57
6.8	Fiber acquisition images.	58
6.9	Quantum efficiency for the Atik cameras	60
6.10	eShel resolving power as function of wavelength	61
6.11	S/N ration as a function of B magnitude and effective exposure time	62
6.12	Guide images showing the object-fiber illumination	63

List of Tables

3.1 Specification of the Atik cameras	24
4.1 Stellar sample selected for observation	29
5.1 RV corrections of the stellar sample	45
6.1 Fractional uncertainties for the stellar sample	53